Distribution Agreement

In presenting this thesis or dissertation as a partial fulfillment of the requirements for an advanced degree from Emory University, I hereby grant to Emory University and its agents the non-exclusive license to archive, make accessible, and display my thesis or dissertation in whole or in part in all forms of media, now or hereafter known, including display on the world wide web. I understand that I may select some access restrictions as part of the online submission of this thesis or dissertation. I retain all ownership rights to the copyright of the thesis or dissertation. I also retain the right to use in future works (such as articles or books) all or part of this thesis or dissertation.

Signature:

_____	_____
Kevin P. Sullivan	Date

Oxidative Studies in Decontamination and Water Oxidation Catalysis

By

Kevin P. Sullivan
Doctor of Philosophy

Chemistry

_____
Craig L. Hill, Ph.D.
Advisor

_____
Vincent Conticello, Ph.D.
Committee Member

_____
Cora MacBeth, Ph.D.
Committee Member

Accepted:

_____
Lisa A. Tedesco, Ph.D.
Dean of the James T. Laney School of Graduate Studies

_____
Date

Oxidative Studies in Decontamination and Water Oxidation Catalysis

By

Kevin P. Sullivan
Bachelor of Arts. Macalester College, 2012

Advisor: Craig L. Hill, Ph.D.

An abstract of a dissertation submitted to the Faculty of the
James T. Laney School of Graduate Studies of Emory University
in partial fulfillment of the requirements for the degree of
Doctor of Philosophy
in Chemistry

2019

Abstract

Oxidative Studies in Decontamination and Water Oxidation Catalysis

By

Kevin P. Sullivan

Oxidation reactions are ubiquitous throughout our society. The development of oxidation catalysts has propelled the advancement of civilization and allowed for significant advancements in science and technology. However, the Earth is currently entering a period in which human activities are causing substantial damage both through chemical pollution and global warming resulting from production of greenhouse gasses. This work addresses issues related to both these concerns, by outlining efforts towards the development of oxidation catalysts in three systems relevant to mitigating the impacts of toxic or polluting chemicals. In the first, synthesis and characterization of a new class of organic/inorganic hybrid polymers composed of covalently-bound 1,3,5-benzenetricarboxamide linkers and anionic polyoxovanadate clusters with varying counter-cations is described. These materials form gels within seconds upon contact with polar aprotic organic liquids and catalyze the degradation of odorants and toxic molecules under mild conditions including aerobic oxidation of thiols, hydrogen peroxide-catalyzed oxidation of sulfides, and hydrolysis of organophosphate chemical warfare agent analogues. The second project describes efforts towards the development of rapid aerobic oxidation catalysts for sulfoxidation reactions. Systems involving tetrabutylammonium tribromide and tetrabutylammonium nitrate are studied and optimized for catalyzing the aerobic oxidation of the mustard gas analogue 2-chloroethyl ethyl sulfide. The addition of Cu(II) to this system results in significant rate enhancements, as well as provides a detection capability by changing color in the presence of sulfides, followed by recovery of the original color when the sulfoxidation is complete. Finally, the third project described in this work details stability studies conducted on the water oxidation catalyst $Na_{10}[Co_4(H_2O)_2(VW_9O_{34})_2] \cdot 26\ H_2O$. This polyoxometalate has been the subject of an ongoing debate regarding its stability under water oxidation catalysis conditions. Solution studies are examined clarifying the stability limitations in this system through ^{51}V NMR resonance experiments on the polyoxometalate. The study demonstrates that the observed catalytic activity cannot be explained simply by $Co(II)_{aq}$, but arises from multiple active water oxidation catalyst species in solution.

Oxidative Studies in Decontamination and Water Oxidation Catalysis

By

Kevin P. Sullivan
Bachelor of Arts. Macalester College, 2012

Advisor: Craig L. Hill, Ph.D.

A dissertation submitted to the Faculty of the
James T. Laney School of Graduate Studies of Emory University
in partial fulfillment of the requirements for the degree of
Doctor of Philosophy
in Chemistry

2019

Acknowledgments

I would first like to thank my advisor Dr. Craig Hill for teaching me how to be a careful and thorough scientist. I can't thank him enough for his constant support through my time here at Emory, for always being willing to listen and help, and for being a compassionate and generous mentor. I would also like to especially thank Dr. Yurii Geletii for his guidance and constant helpfulness. Dr. Geletii's passion for science is always an inspiration, and I will never forget his anecdotes which always manage to be both philosophical and hilarious. I would like to thank all current and former members of the Hill lab, who have been extraordinarily helpful and friendly: Dr. Weiwei Guo, Dr. Hongjin Lv, Dr. Chongchao Zhao, Dr. Sarah Lauinger, Dr. Guibo Zhu, Dr. Zhen Luo, Dr. Mooeung Kim, Jordan Sumliner, Dr. Jim Vickers, Yimu Hu, Meilin Tao, Dr. Elliot Glass, Phillip Zhu, Torie Snider, Xinlin Lu, Dr. Juan Cardenas, Dr. Yamin Li, Dr. Yingnan Chi, Dr. Iftikhar Ahmad, Dr. Masoumeh Chamack, and Natalie Uhlikova. I want to thank Daniel Collins-Wildman for our many adventures and stories gained through the years, Ben Yin for always being up for a lively debate at 4 am, and Marika Wieliczko for always going way out of her way to be helpful. Thank you to my undergraduate research assistants Rachel Slaugenhaupt, Paul Yang, Ben Natinsky, Rocky Li, and Jeffrey Li. I also want to acknowledge Dr. Charlie Modlin, Samantha Iamurri, Dr. Christian Wallen, Gregory Karahalis, Jack Trieu, and Dr. Skanda Vivek for being companions to me through the program.

I thank Dr. Cora MacBeth for always making time to talk about scientific and career goals and helping whenever possible. I would like to thank my former committee member Dr. Chris Scarborough and my current committee member Dr. Vince Conticello for providing guidance through my scientific progress at Emory. I want to acknowledge Dr. Bing Wang and Dr. Shaoxiong Wu for providing an enormous amount of help with many strange NMR experiments, and to Dr. Anil Mehta for helping me to interpret them. I want to particularly thank my undergraduate advisor Dr. Paul Fischer for providing my first experience of doing science and for teaching me the skills I needed to succeed in graduate school.

I feel honored by how lucky I am to have the family that I do. The constant support, love, and encouragement from my mother and father, Catherine and Dan Sullivan, has helped me through every step of the way. I hope to make them feel as proud to be my parents as I feel to be their son. I also want to thank my brother Patrick Sullivan for providing the much-needed laughs and cheer. I thank Nicole Powell for helping me through the thick of it and being practically perfect in every way. I would particularly like to thank my housemates for life Filomene Morrison and Melanie Pincus, who turned our house into a home that I will cherish in my memories for all my days, and Huxley Pincus for always lending a helping paw. I would like to thank Scott Hudson, Jay Schwartz, Dr. Kennedy McCollough, Mariam Asad, Dr. Katy Renfro, Brenna O'Neill, Casey Dallavalle, Jeff Schriber, Rebecca Kelly, John Kaufman, Adam Lipus, Anita Kambhampati, and many others for their friendship and support.

I also want to thank the Defense Threat Reduction Agency and the Army Research Office for providing me with funding to carry out my research.

Table of Contents

List of Figures

List of Abbreviations

A	absorbance
AChE	acetylcholinesterase
atm	standard atmosphere
ATR	attenuated total reflectance
bpy	2,2'-bipyridine
BTC	1,3,5-benzenetricarboxamide
BTU	British thermal units
CEES	2-chloroethyl ethyl sulfide
CEESO	2-chloroethyl ethyl sulfoxide
$CEESO_2$	2-chloroethyl ethyl sulfone
Co_9	$[Co_9(H_2O)_6(OH)_3(HPO_4)_2(PW_9O_{34})_3]^{16-}$
Co_4P_2	$Na_{10}Co_4(\alpha\text{-}PW_9O_{34})_2]$
Co_4V_2	$Na_{10}Co_4(\alpha\text{-}VW_9O_{34})_2]$
CoO_x	Cobalt oxide
CV	cyclic voltammetry
CWA	chemical warfare agent
CWC	Chemical Weapons Convention
DALY	disability-adjusted life year
DECP	diethyl cyanophosphonate
DFT	density functional theory
DLS	dynamic light scattering
DMA	*N*,*N*-dimethylacetamide

DMF	*N*,*N*-dimethylformamide
dmg	dimethylglyoxime
DMMP	dimethyl methyl phosphonate
DMNP	dimethyl *p*-nitrophenylphosphate
EA	elemental analysis
EtOH	ethanol
FT-IR	fourier transform infrared spectrsocopy
GA	tabun
GB	sarin
GC	gas chromatography
GD	soman
GOE	great oxygenation event
HD	*bis*(2-chloroethyl)sulfide
ICP-MS	inductively coupled plasma mass spectrometry
k_n	rate constant for reaction n
LMWOGs	low molecular weight organogelators
MAS	magic-angle spinning
MeCN	acetonitrile
MeOH	methanol
MOF	metal-organic framework
NaB	sodium borate buffer
NaP	sodium phosphate buffer
NEM	*N*-ethylmorpholine

NHE	normal hydrogen electrode
NH_2V_6	$[(n\text{-}C_4H_9)_4N]_2[(V_6O_{13})[((OCH_2)_3CNH_2]_2$
NO_x	nitrogen oxide
OEC	oxygen evolving complex
OP	organophosphate
POM	polyoxometalate
PrSH	propane thiol
PrSSPr	dipropyl disulfide
PSII	photosystem II
PTFE	polytetrafluoroethylene
p-TsOH	*p*-toluenesulfonic acid monohydrate
Q	index of swellability
Ru_4P_2	$[\{Ru_4O_4(\gamma\text{-}PW_{10}O_{36})_2]^{10-}$
SEM	scanning electron miscoscope
SLS	static light scattering
SS CP-MAS	solid-state cross-polarization magic angle spinning
TBA	tetrabutylammonium
TBA-polyV_6	$[(n\text{-}C_4H_9)_4N]_{2n}[(V_6O_{13})_n[((OCH_2)_3CNHCO)_3C_6H_3]_x$ $[((OCH_2)_3\text{-}CNHCO)_2((HOCH_2)_3CNHCO)C_6H_3]_y$ $[(OCH_2)_3CNHCO((HOCH_2)_3CNHCO)_2C_6H_3]_z]$
TBA-Co_4P_2	$TBA_6H_4[Co_4(H_2O)_2(PW_9O_{34})_2]$
TBA-Co_4V_2	$TBA_6H_4[Co_4(H_2O)_2(VW_9O_{34})_2]$
TEM	transmission electron microscope
THT	tetrahydropthiophene

THPA	Tetra-*n*-heptylammonium
TOF	turnover frequency
trisBTA	$C_6H_3(CONHC(CH_2OH)_3)_3$
UV-Vis	ultraviolet-visible spectrsocopy
VW_5	$[VW_5O_{19}]^{3-}$
V_2W_4	$[V_2W_4O_{19}]^{4-}$
V_6O_{19}	hexavanadate
VX	Ethyl ([2-[bis(propan-2-yl)amino]ethyl] sulfanyl)(methyl)phosphinate
WOC	water oxidation catalyst
WRC	water reduction catalyst
XPS	X-ray photoelectron spectroscopy
XRD	X-day diffraction
Å	angstrom (10^{-10} meters)
λ	wavelength

Chapter 1: Introduction

Overview of Oxidation Catalysis

1.1 Oxidation on Earth

In interplanetary space, solar wind (consisting of primarily hydrogen plasma) causes most of the universe to exist in a reducing atmosphere.[1-2] Until approximately 2.4 billion years ago, the earth existed in such an environment.[3] At this time, the reign of the reductive atmosphere was ended by a particularly resourceful phylum: the cyanobacteria. The triumph of these organisms in their oxidative assault on the Earth during the great oxygenation event (GOE) forever changed the planet (Figure 1.1). The source of their success was the ability to use photosynthesis to convert solar energy into fuel using their principal asset, the chloroplast.[4-5] Chloroplasts are organelles containing a series of enzymes involved in absorbing light and converting it into chemical energy. One of these enzymes, the oxygen evolving complex (OEC), contains a metal-oxo core which is responsible for the crucial conversion of H_2O to O_2 during photosynthesis and ultimately allows the organism to convert solar energy into carbohydrates .[6-7] This overall process is known as photosynthetic water oxidation.

Oxidation can be simply defined as a chemical reaction in which electrons are lost, resulting in an increase in the oxidation state of a substance. Oxygen can oxidize a variety of compounds spontaneously; a common example is the oxidation of Fe(II) to Fe(III) by oxygen to produce rust. During the GOE, the oxygen produced by cyanobacteria was rapidly consumed as the metal centers in terrestrial minerals were oxidized. This is marked on the geological record by the presence of banded iron formations; layers of iron oxides present in sedimentary rock.[8] After oxidation of these terrestrial minerals, oxygen rapidly accumulated in the atmosphere, oxidizing methane to carbon dioxide and water.[9] Global cooling from the conversion of the strong greenhouse gas methane to

the weaker greenhouse gas carbon dioxide allowed for the development of multicellular life and led to the enormous biodiversity of the following geological eras.[10]

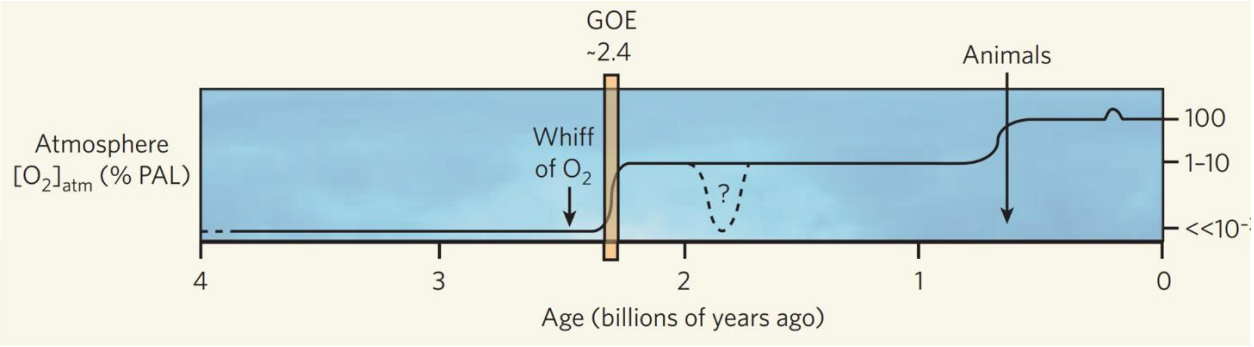

Figure 1.1. Concentration of O_2 in the atmosphere of Earth in % present atmospheric level (%PAL). Adapted with permission from Nature: *Nature*, Oxygen for Heavy-Metal Fans, Lyons, T.W., Reinhard, C.T., © 2009.[11]

The earth has changed substantially since the Precambrian era, but the legacy of the GOE remains. Our planet has retained its oxidative environment, with an atmosphere consisting of 21% oxygen. Like the revolutionary cyanobacteria long ago, a new organism has emerged that is rapidly and profoundly altering the environment of the Earth. Rather than producing oxygen, however, humans have employed it to create the outstanding marvels of modern civilization. Indeed, our species has developed substantially since we were first able to harness the energy released from the oxidation of hydrocarbons with oxygen through combustion. Controlling oxidation in this way has been one of the defining features of humanity, leading to the ability to cook food, the use of smelting to create revolutionary alloys such as bronze, the development of the internal combustion engine, and beyond. Though oxygen can oxidize a variety of compounds, the triplet ground state of O_2 is relatively unreactive. Over at least four billion years, biological systems evolved to circumvent issues of low reactivity using enzymes to catalyze reactions.[12] Such enzymes include oxidases, which use O_2 as the electron acceptor in a vast number of enzymatic reactions. The directed use of catalysts by humans to carry out specific functions, however, is a relatively recent occurrence. In

1794, the Scottish chemist Elizabeth Fulhame invented the concept of catalysis in a book detailing experiments on a variety of oxidation reactions.[13] Since that time, a vast quantity of oxidation catalysts have been developed and are used in a wide range of applications, including the degradation of toxic chemicals, functionalization of feedstock molecules, and extraction of energy from chemical bonds, among many others. Around 75% of industrially-produced chemicals are generated using catalysts, with many involving catalytic oxidation, as is the case in the production of nitric acid, sulfuric acid, ethylene oxide, acrylonitrile, terephthalic acid, and many more.[14-15] Because these chemicals are produced on such a large scale, even small differences in the process enormously influences the cost of the reaction, in both energetic and monetary terms. The bulk chemicals industry accounts for 30% of total industrial energy consumption, constituting roughly one-sixth of total energy consumption in the US in 2017.[16] Molecular oxygen has been considered as an ideal green oxidant owing to its abundance, low molecular weight, low cost, and because it typically generates water as a byproduct.[17] Of the industrial oxidation processes with a capacity of > 1000 tons per year, ~60% use O_2 as an oxidant.[17] Because of the large economic and energetic impacts, there is a constant need for ever more efficient and selective aerobic oxidation catalysts.

1.2 Chemistry and Global Stewardship

Our control of oxidation has allowed our society to flourish, but along with the extraordinary benefits have come severe consequences. Toxic compounds resulting from human actions have contaminated nearly every part of the globe from the upper atmosphere to the ocean floor. In North America during the year 2009 alone, 4.9 million metric tons of chemicals were released to the environment or disposed of, including 1.5 million metric tons of chemicals classified as persistent, bioaccumulative, and toxic, as well as 750,000 metric tons of carcinogenic compounds.[18-19] These

chemicals have significant impacts on both human and animal populations. The US Environmental Working Group has identified human exposure to a large number of toxic chemicals, showing that nearly all individuals tested were exposed to significant levels of polybrominated diphenyl ethers, bisphenol A, and perfluorooctanoic acid, among many others.[20] Though it can be difficult to attribute direct health outcomes of chronic low-level exposure to any one specific chemical, it is clear that overall exposures are a massive global health concern. The World Health Organization has estimated that 12.6 million people died in the year 2012 due to living in unhealthy environments and considers most of these deaths preventable.[21] These impacts are acutely felt by the world's most vulnerable populations, affecting people in low-and middle-income nations far more substantially, as can be measured in terms of disability-adjusted life years (DALYs), a metric indicating number of years lost due to ill health (Figure 1.2).

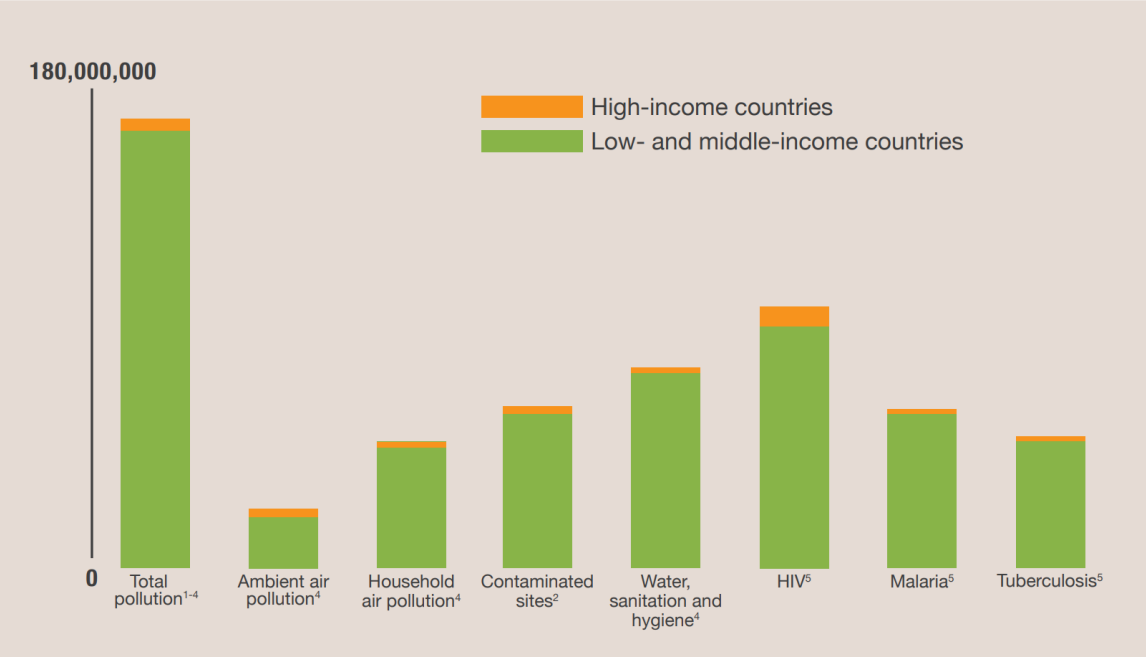

1: Disease and injury regional mortality estimates 2011. http://www.who.int/entity/healthinfo/global_burden_disease/estimates_regional/en/index.html
2. Contaminated sites data extrapolated from GAHP database.
3. Population for 2013 - high income. Available at: http://www.tradingeconomics.com/high-income/population-total-wb-data.html
4 DALYs and deaths attributable to selected environmental risk factors, by WHO Member State, 2004. http://www.who.int/quantifying_ehimpacts/national/countryprofile/intro/en/
5. Estimated DALYs by cause, WHO Member States, 2012 http://www.who.int/healthinfo/global_burden_disease/estimates/en/index2.html

Figure 1.2. Global pollution DALYs versus other major causes. Figure reproduced with permission from Pure Earth © 2015.[22]

In addition to the harm caused by chemical pollution, perhaps an even greater impact of human activity results from global warming resulting from greenhouse gas emissions. As large quantities of greenhouse gases (such as CO_2 or CH_4) emitted from combustion have accumulated, the temperature of the earth has risen substantially, with profound consequences to the ecosystem of the planet. The world used 575 quadrillion British thermal units (BTU) of energy in 2015, with a majority of this energy originating from fossil fuels.[16] As a result, the average temperature of the Earth has risen approximately 1°C ± 0.2°C above pre-industrial levels as of 2017 and is likely to continue to rise unless greenhouse emissions are substantially curtailed (Figure 1.3).[23] This has already had significant consequences for the environment of the Earth, causing increased incidences of temperature extremes, heavy precipitation events, wildfires, coastal flooding from rising sea levels, and ocean acidification, among many other problems.[24] The damage from climate change is predicted to increase, causing significant impacts to human and environmental health, as well as on the economy. In 2018, the Fourth National Climate Assessment estimates that the U.S. economy will shrink by as much as 10% by the end of the 21st century due to impacts from climate change.[24] The impacts of climate change will be felt globally, but they are expected to have a greater effect on areas that already have lower than average socioeconomic status, exacerbating famines, and increasing global income inequality. A variety of changes must be made in order to mitigate significant global temperature increases, but the most significant of these is to reduce the generation of greenhouse gas emissions from fossil fuels.

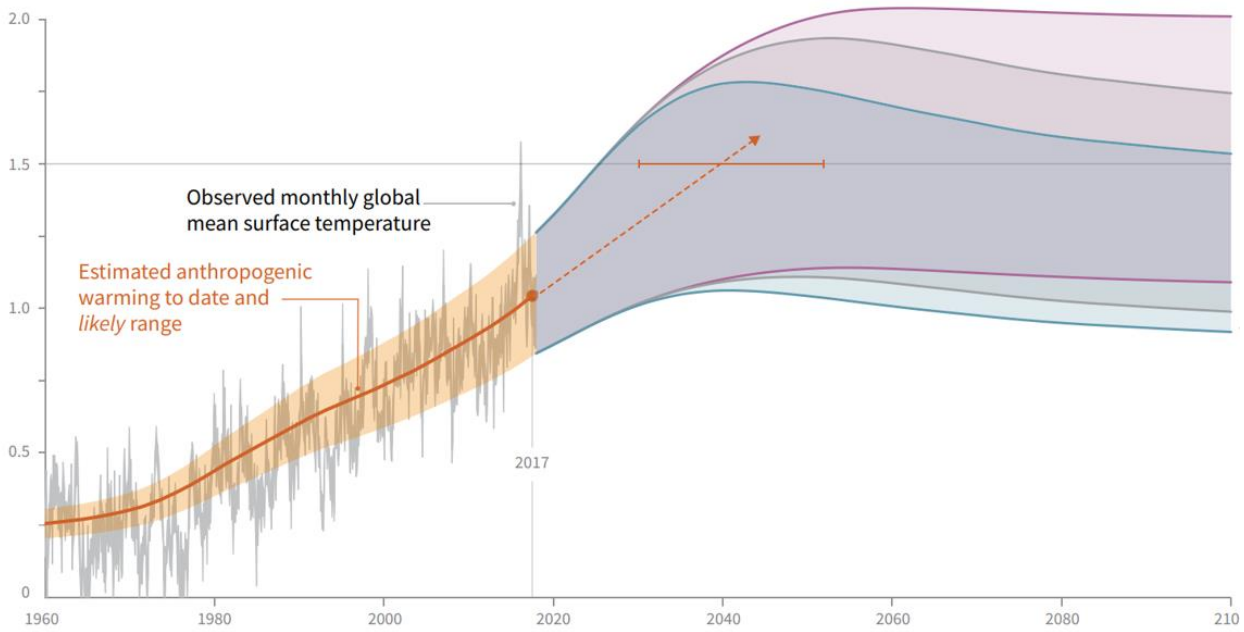

Figure 1.3. Global warming relative to 1850-1900. The three shaded areas represent different predictions based on differing global responses, with light purple representing no reduction of CO_2 emissions after 2030, dark purple representing CO_2 emissions reaching a net zero in 2055, and blue representing CO_2 emissions reaching a net zero in 2040 reproduced with permission from the Intergovernmental Panel on Climate Change © 2018.[23]

The impact that human activities have had on animal lives is similarly striking. As of 2014, 26% of described mammal species and 41% of described amphibian species are listed as "threatened."[25] Even more alarming is the 60% decline in total number of vertebrates between the period of 1970 to 2014.[26] This human-caused species loss is known as the Anthropocene extinction, and is estimated to already be occurring at rates 1000 times higher than previous mass extinction events, presaging profound negative impacts on global ecology and biodiversity on an unprecedented scale.[27]

It is clear that we need to be better stewards of our planet; unconscionable use of our chemical capabilities has led to unparalleled global devastation. However, chemistry also represents our most viable path to salvation. The recent conception of, and developments in, the field of green

chemistry have shown the exciting advances that can be made when resources and willpower are employed towards developing solutions to these issues. Looking to the future, there are several things that chemists must accomplish to alleviate our global impacts. Firstly, we must aim to reduce the global burden of toxic chemicals. This issue, being multifaceted, can be undertaken in a variety of ways. As examples, designing more efficient and selective reactions and catalysts helps to reduce the generation of waste side products, and developing novel decontamination methods aids in remediating contaminated environments. Secondly, renewable sources of energy must replace fossil fuels as the dominant energy source. This can be accomplished through developments in wind, solar, geothermal, and hydroelectric power technologies, in energy storage systems such as batteries, and in generation of fuels from renewable sources. As chemists, it is imperative that we remain aware of the profound impacts that our science has on the rest of the world. By increasing awareness of these issues and fostering innovation in sustainability-related disciplines, we can lead ourselves into a future that minimizes our ecological impacts, reverses damage done to the environment, and preserves our planet.

1.3 Examples of Important Oxidation Reactions

1.3.1 Decontamination of Toxic Compounds

One area in which the use of oxidation chemistry is widespread is in the oxidation of toxic compounds. Oxidative chemistry is particularity useful in wastewater decontamination at large scales, where chemical oxidants such as ozone, chlorine, or hypochlorite are used to mineralize chemical and biological contaminants.[28] When decontaminating toxic chemicals in the

environment, however, more mild oxidants are required, including photooxidation catalysts such as TiO_2, or oxidants such as CaO, or H_2O_2.[29-30]

In addition to decontamination of pollutants, oxidation can be employed to decontaminate chemicals of a more nefarious nature. Chemical warfare agents (CWAs) are chemicals that have been specifically formulated to kill or harm humans and are among the most toxic known substances. Because of this, efficient detoxification of CWAs has been a major global concern for decades.[31-33] Chemicals have been used by humans in warfare for millennia, with the earliest records of poison-tipped arrows appearing in the Indian epic "Ramayana" around 2000 BC.[34] However, chemical warfare in the modern era began during World War 1, with German forces deploying chlorine gas during the battle of Ypres. Following this, release by both sides of chlorine, phosgene, and sulfur mustard [*bis*(2-chloroethyl)sulfide; (HD)] gas resulted in the deaths of 1.3 million people, many of whom were civilians downwind of battlefields.[35] Sulfur mustard is a vesicant (blistering agent) and is both mutagenic and carcinogenic. The mechanism of toxicity is primarily through alkylation of DNA nucleotides, resulting in cellular apoptosis.[36] Because it has low water solubility and a relatively low vapor pressure, is can persist after release for extended time periods and can be rapidly absorbed through skin contact with contaminated surfaces.[37]

After the end of World War 1, research in insecticides by Germany resulted in the discovery of the first nerve agents: sarin (GB), tabun (GA), and soman (GD), known as the G-series nerve agents.[38] Later, Ethyl ([2-[bis(propan-2-yl)amino]ethyl]sulfanyl)(methyl)phosphinate (VX) and related agents were developed in England, showing even higher toxicity (Figure 1.4). These organophosphate (OP) nerve agents are extremely toxic due to their activity in inhibition of the

enzyme acetylcholinesterase (AChE).[39] AChE is involved in the breakdown of the neurotransmitter acetylcholine, which is involved in a large number of biological processes, but most notably in muscle contraction. Interaction of AChE with OP agents results in irreversible binding to the active site, permanently deactivating the enzyme.[38] The activity of AChE is exceedingly high, with each enzyme capable of removing 10^4 molecules of acetylcholine per second. Inhibition of AChE therefore results in a very rapid increase of acetylcholine in nerve synapses, causing uncontrolled muscle contraction and quickly leading to death from asphyxiation or other complications. [40]

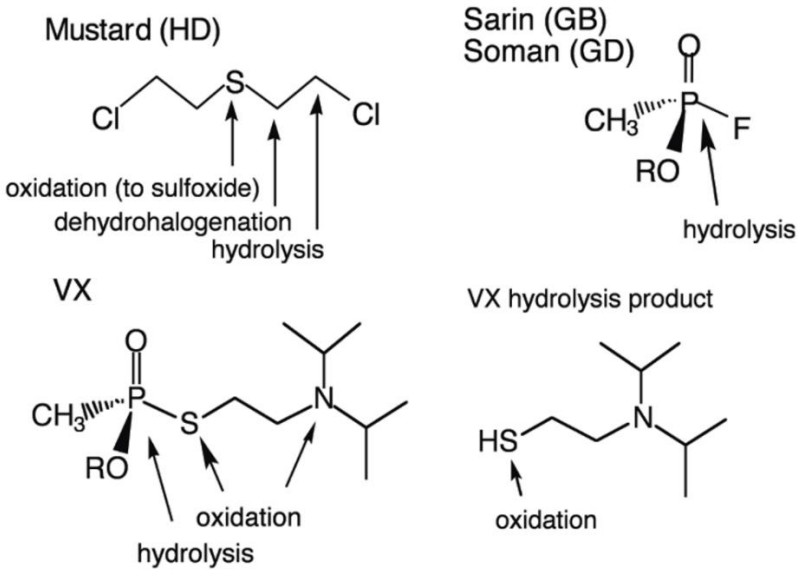

Figure 1.4. Common chemical warfare agents and potential routes of decontamination.

Despite seeing limited use in World War 2, CWAs were used in several more recent conflicts, such as the Iran-Iraq war, and the Syrian civil war.[41-42] These agents were stockpiled in huge quantities around the world until 1993 when the Chemical Weapons Convention (CWC) was ratified, outlawing the production, stockpiling, and use of CWAs. The CWC represents a historic achievement in global disarmament, leading to a 92% reduction in global chemical stockpiles as of 2017.[43] However, because of their relative ease of synthesis, high toxicity, and potential for

large-scale release, both HD and the OP CWAs continue to remain priority decontamination targets.[31, 38, 42, 44-45] Several CWAs can be decontaminated through oxidation, including HD and VX. Because of its hydrophobicity, decontamination of HD through oxidation of the sulfide is favored over hydrolysis and has been the topic of several recent studies.[38, 44, 46-50] Oxidation of sulfides can be readily achieved using strong oxidants. However, these methods cannot be used for situations in which HD has been released as strong oxidants are toxic or corrosive themselves. Additionally, these strong oxidants typically generate the sulfone product, which retains significant vesicant activity.[48] The challenge in designing effective systems for oxidation of HD to the nontoxic sulfoxide, therefore, is that the system needs to be both rapid, selective, and functional under mild conditions.

The OP CWAs are susceptible to decontamination by hydrolysis, which has been explored by several recent studies, most notably those involving the use of metal-organic frameworks (MOFs) and nanostructured metal oxides.[38, 41, 51-54] Current research in both hydrolysis and oxidation of CWAs has focused on developing practical materials for in-field use during CWA exposure. While liquid decontaminants such as bleach or hydrogen peroxide can successfully degrade many CWAs, their use in the field is often prohibitive due to transportation and storage difficulties.[31] An ideal decontamination agent is therefore a solid that can rapidly and effectively remove or neutralize chemical threats, be stable and active under environmental conditions, and be both inexpensive and synthetically facile to produce.[44] Some of the most promising materials towards these aims are "reactive sorbents," which combine the advantages of CWA sequestration and decontamination. Though there are several materials capable of decontaminating CWAs, most of them are stoichiometric, rapidly becoming deactivated as they degrade the agent. [38, 41] Ideal

decontamination methods would therefore be catalytic, allowing for a minimal amount of material to treat a large amount of the toxic agent. Development of effective catalysts with these attributes would therefore represent a significant advance in protection technologies.

1.3.2 Water Oxidation

Fossil fuels, such as coal, gasoline, or methane, are incredibly useful sources of power, and have greatly accelerated the advancement of human civilization. Fossil fuels are named after their origins from organic matter and were formed as a result of anaerobic decomposition when various plant, phytoplankton, and zooplankton species became buried under layers of sediment.[55] Because the metabolism of these organisms was driven by photosynthesis, sunlight is ultimately the origin of the energy found in fossil fuels. Fossil fuels are particularly beneficial due to their high energy densities, allowing a small amount of the substance to generate a large amount of energy. This is extracted through combustion of the fuel source to release CO_2, H_2O, and energy. The primary disadvantages, however, are the finite nature of fossil fuel resources as well as the harmful impacts of greenhouse gases emitted through combustion of these fuels. This high energy density is both what makes fossil fuels so useful and what poses the greatest challenge for replacing them with renewable energy sources. Current renewable methods of generating power (such as solar, wind, geothermal, nuclear, etc.) all result in the generation of electrical energy, which has a very low energy density relative to fossil fuels. For example, the specific energy (defined as the amount of energy per unit mass) of coal is 3235 W h/kg, whereas the specific energy of a lithium-ion battery is 385 W h/kg.[56] This difference poses several challenges, including grid instability due to peak energy consumption misaligning with peak energy production, as well as difficulties in supplying large energy demands, such as powering airplanes or shipping vessels.[57] Batteries can be used to

store some of the produced electrical energy as chemical energy, and developing more effective batteries is crucial in order for renewable energy to be able to replace fossil fuels.[58] However, currently, we only have the capacity to store ~1% of the energy consumed worldwide.[59] Though developing more effective batteries will bolster the capabilities of renewable energy, batteries are costly, often rely on utilizing large amounts of finite resources, and remain far less energy-dense than fossil fuels.[59] Therefore, access to chemical fuel from renewable sources without requiring the use of batteries would be a substantial step in reducing dependence on fossil fuels.

One fuel that been investigated extensively is H_2, as it possesses several advantages including higher energy density and the generation of H_2O as the only waste product of combustion. Because of this, H_2 represents a realistic target "green" fuel.[60] The technology for using H_2 as a fuel source is developing rapidly, but a primary issue is the large energetic cost to produce and purify H_2 through electrolysis, which often uses energy derived from fossil fuels. Recently, therefore, much effort has been spent to develop catalysts capable of facilitating the conversion of solar energy into chemical energy by splitting H_2O to generate H_2 and O_2, thereby creating a high-density fuel from a renewable energy source.

The thermodynamic potential of water splitting ($2H_2O \rightarrow H_2 + O_2$) is -1.23 V v. the normal hydrogen electrode (NHE) and requires large overpotentials. Catalysts are therefore needed to lower the energetic barrier for water splitting reactions.[61] The process of photosynthesis has been investigated as a template for the ability to produce H_2 from H_2O and sunlight. Photosynthesis involves an extremely complex series of reactions, enzymes, and biological molecules, a full understanding of which remains elusive. Sunlight is captured in Photosystem II (PSII) through

photoexcitation of chlorophyll dimer P680, generating the strongly reducing P680*, which begins the transfer of electrons through the electron transport chain.[62] This proceeds through the "z-scheme,' absorbing another photon in photosystem I, to result in the formation of ATP and NADPH, units of "energy currency" that cells use to produce glucose.[63] The resulting oxidized $P680^+$ is the strongest known biological oxidizing agent,[64] and is reduced back to P680 using electrons originating from water oxidation in the OEC.[7, 65] The OEC, introduced in section 1.1, is an inorganic cluster containing four manganese atoms, and is surrounded by PSII (Figure 1.5).[66-67] The process of water oxidation mediated by the OEC proceeds in a 4-electron, 4-proton, and 4-photon process known as the Kok cycle, generating oxygen, protons, and electrons (Figure 1.5).[68]

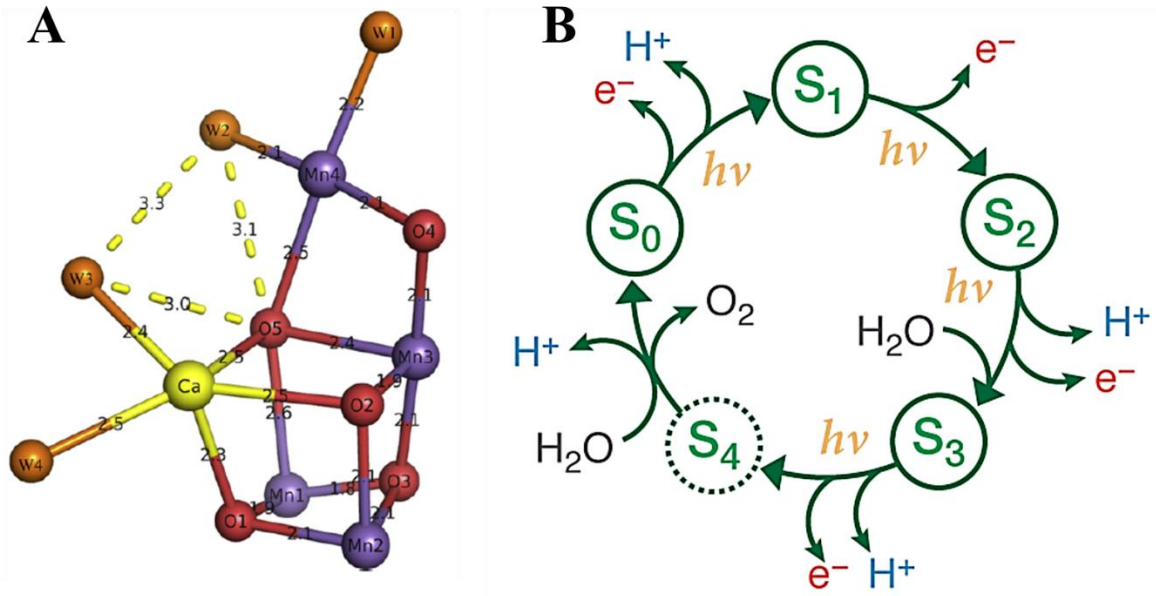

Figure 1.5. The oxygen-evolving complex in photosystem II and the Kok cycle. Crystal structure of the OEC in photosystem II at a resolution of 1.9 Å. Water molecules indicated by orange spheres, Mn atoms indicated by purple spheres, O atoms indicated by red spheres, and Ca atom indicated by yellow spheres. Figure reprinted with permission from Blakemore, J.D., Crabtree, R.H., and Brudvig, G.W. *Chemical Reviews* **2015** 115 (23), 12974. Copyright 2015 American Chemical Society.[69] (**B**) Depiction of the Kok cycle of the OEC. The cycle begins at the resting state, S_0, and terminates at S_4, with release of O_2 and generation of H^+. Figure reproduced with permission from V. Krewald, M. Retegan, N. Cox, J. Messinger, W. Lubitz, S. DeBeer, F. Neese and D. A. Pantazis, Chem. Sci., 2015, 6, 1676. Published by The Royal Society of Chemistry.[70]

Artificial photosynthesis differs fundamentally from natural photosynthesis in a variety of ways. For example, instead of charge separation occurring as a result of cascading bioenzymatic pathways, it is done through a semiconductor.[71] Biological systems are self-repairing by nature, but artificial systems must be stable in order to prevent the system from deactivating. The conversion of H_2O into O_2 and H_2 requires two half-reactions which are facilitated using both water oxidation catalysts (WOCs), responsible for oxidation of H_2O to O_2 and water reduction catalysts (WRCs) which catalyze the reduction of H^+ to H_2. In solar-powered water splitting reactions, the photoelectrochemical cell is composed of a photosensitizer, a WOC at the anode, and a WRC at the cathode (Figure 1.6).[69] Water reduction is significantly more facile as it is only a two-electron process with many types of electrodes (usually platinum-based) capable of operating at desired current densities with low overpotentials.[72] However, the other half-reaction involving water oxidation is one of the bottlenecks to implementation of solar water splitting technology.

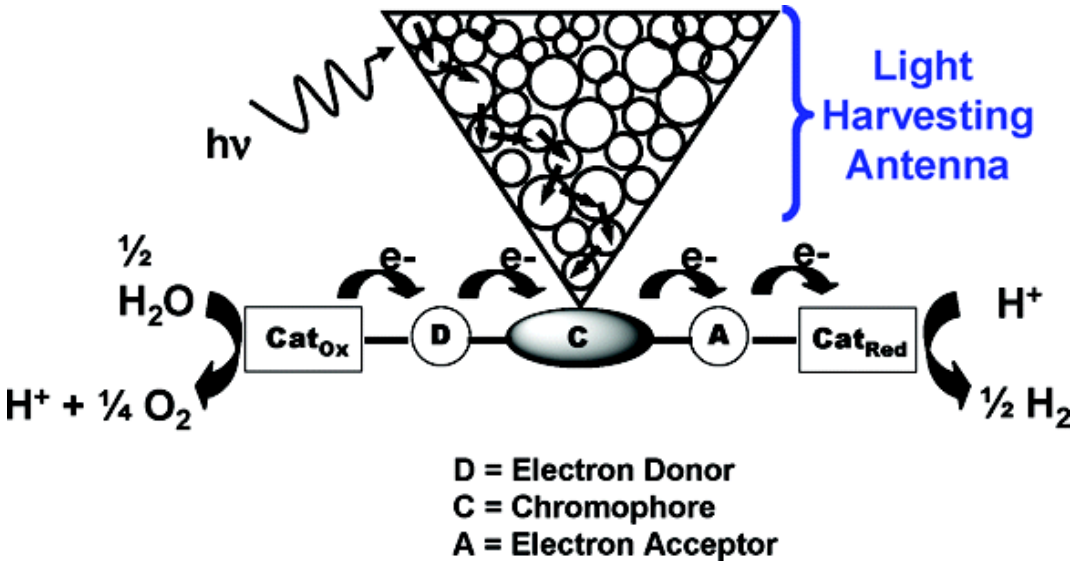

Figure 1.6. General scheme for artificial water splitting. Figure reprinted with permission from Alstrum-Acevedo, J. H. et. al. *Inorganic Chemistry* **2005** 44 (20), 6802. Copyright 2005 American Chemical Society.[71]

Water oxidation is a 4-electron process, making it significantly more challenging as the lack of redox potential leveling between these steps makes it difficult to achieve low overpotentials.[73-74] Additionally, oxidizing conditions are harsh and tend to decompose catalysts after few turnovers, especially if these catalysts contain organic groups. The stability of WOCs is therefore an issue of significant importance and explains why there are many efforts to develop inorganic catalysts containing no oxidizable organic groups.[75] Many of the most active and stable WOCs are Ru- or Ir-based, but the prohibitive costs of these elements precludes them from use in real-world situations. There is therefore great effort to develop WOCs that are stable and based on elements that are more abundant, such as Co, Ni, and Fe.[76] Many effective WOCs are heterogeneous, but such systems are very challenging to fully characterize.[61] Because of this, a variety of homogeneous systems have been developed which are substantially easier to modify, study, and characterize in order to gain a greater understanding of water oxidation mechanisms.[69] Though artificial photosynthesis has been an active area for some time with a large number of studies and

reviews dedicated to the effort, many challenges remain, maintaining this field as one of the most highly studied current areas in chemistry.

1.4 Polyoxometalates in Oxidation Catalysis

1.4.1 Overview of Polyoxometalates

Polyoxometalates (POMs) are oligomeric aggregates of metal cations bridged by oxide anions, and have received significant attention for their applications in many fields, including catalysis, energy conversion, memory storage, and medicine, among others.[77-78] POMs exhibit diverse chemical and structural properties, are generally oxidatively and hydrolytically stable, relatively inexpensive, and synthetically facile.[79-80] In addition, POMs are highly tunable, allowing for modifications to be made while retaining the integrity of the structure.

Some of the most common POMs structures are shown in Figure 1.7. Keggin POMs, with the general formula $XM_{12}O_{40}^{n-}$, (where M = Mo or W and X = a central tetrahedral heteroatom, commonly P, Si, or Al) have been used in many applications and have been extensively studied.[81] One reason for their usefulness is because they can easily be converted to the lacunary form in which one of the MO_4^{2-} units is removed, producing a relatively stable structure containing a defect site which can react with other transition metals to form new POMs with a wide variety of geometries and chemical properties, allowing them to be tailored to many specific applications.[78, 82]

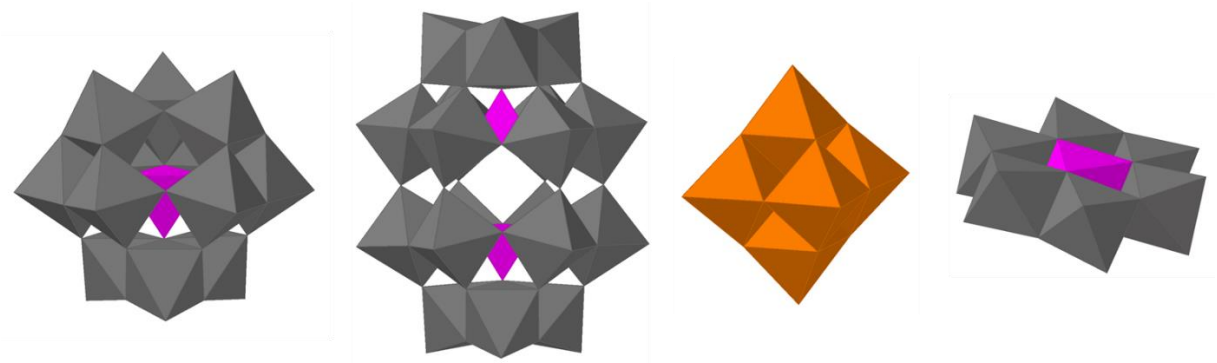

Figure 1.7. Common POM geometries. From left to right: Keggin, Wells-Dawson, Lindquist, and Anderson POMs. Grey octahedra represent W or Mo, orange octahedra represent V or Mo, purple octahedra or tetrahedra represent heteroatoms which are commonly P, Si, or Al.

This tunability extends beyond the realm of inorganic chemistry, as a variety of POMs have been developed which react with organic groups to form organic/inorganic hybrids. Combining POMs with organic components to create organic/inorganic hybrid molecules or polymers allows for rational design of multifunctional compounds with unique properties.[82-86] Inorganic/organic polymer materials are important in multiple disciplines as they allow for synergy between the physical properties of traditional polymers and the versatility in function of inorganic materials, and facilitate rational design of multifunctional compounds.[81-83, 87-93] Several strategies exist for the immobilization of POMs, including electrostatic attraction, solvophobic interactions, or covalent linkages, with the latter generally leading to the most stable products.[84, 94-95] Most commonly, covalent incorporation of POMs and other inorganic compounds into polymer matrices is achieved through side-chain functionalization either before or after the polymerization process.[85, 96-99] Few studies have described polymers containing POMs in the main backbone of the networks, which allow for unique POM-organic composite structures and functions to be achieved.[100-104] Polymers containing inorganic components in the main chain usually have quite low solubility, which is advantageous for their use in heterogeneous systems but makes molecular-level characterization challenging.[96]

1.4.2 Polyoxometalates in Decontamination

A variety of POMs have demonstrated usefulness in catalyzing decontamination reactions, including in wastewater decontamination, toxic gas sequestration, and radioactive waste processing, among others.[105-106] POMs are especially useful for these purposes due to their redox properties, which allow them to oxidize toxic compounds into nontoxic products. Additionally, their tunability allows for a range of multifunctional materials to be created. Multifunctional materials that both entrap and remove deleterious compounds are highly sought for protection and decontamination technologies. Gelation is one strategy used to immobilize compounds within a solid material. Stimuli-responsive gelator molecules that swell in the presence of solvents have gained increasing interest, as they allow for the creation of highly tunable stimuli-responsive materials.[107] Multifunctional POM-polymers will be further discussed in Chapter 2 of this work.

1.4.3 Polyoxometalates in Water Oxidation

POMs have attracted much attention in the field of water oxidation catalysis due to their oxidative stability and tunability, allowing them to serve as molecular models of heterogeneous WOCs.[75, 108] POMs are especially useful in this regard as they are capable of undergoing multiple electron transfers. One of the most well-studied POM WOCs is $[\{Ru_4O_4(\gamma\text{-}SiW_{10}O_{36})_2]^{10-}$ (**Ru_4Si_2**), which is highly active with turnover frequencies (TOFs) of ~1 mol O_2 s^{-1} at pH 7, and is stable over a wide pH range.[109] Another POM WOC that has been investigated extensively by our group is $[Na_{10}Co_4(\alpha\text{-}PW_9O_{34})_2]$ (**Co_4P_2**), which is notable not only because it uses the more earth-abundant Co, but also because of its TOF for the water oxidation reaction is ~6 s^{-1}.[110] Recently, the POM $[Na_{10}Co_4(\alpha\text{-}VW_9O_{34})_2]$ (**Co_4V_2**) has been investigated by our group, which showed a TOF of up to ~1000 s^{-1} (Figure 1.8). However, the speciation of **Co_4V_2** is quite complex at elevated pH, leading

to significant challenges when assessing its activity and stability under these conditions. This issue is further discussed in chapter 4 of this work.

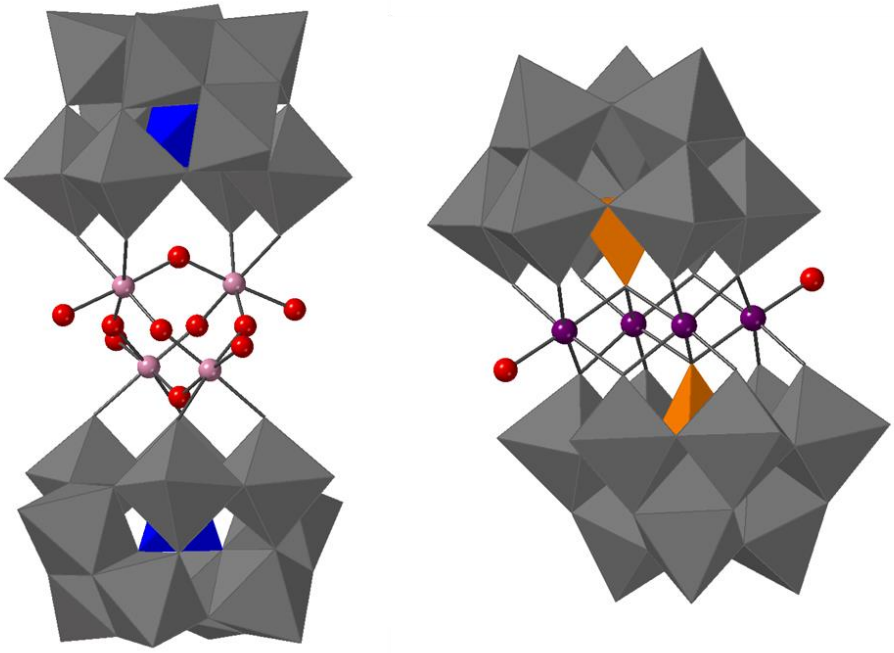

Figure 1.8. **Ru_4Si_2** and **Co_4V_2** POMs. Grey octahedra represent W, tetrahedra represent Si (blue) and V (orange). Spheres represent O (red), Co (purple), and Ru (pink).

Though the field of POM WOCs is maturing, there are a variety of challenges that remain. As examples, recent efforts have investigated the immobilization of POMs onto surfaces to create heterogeneous catalysts with well-defined structures,[111] as well as POMs that are stable in very acidic conditions as very few earth-abundant WOCs are currently capable of operating at low pH.[112]

1.5 Scope of Current Work

The current work investigates three systems that have been developed for catalytic oxidation reactions. The first chapter describes an organic/inorganic polymer containing POMs in the main chain which is capable of catalytically oxidizing the odorant propane thiol into the corresponding

non-odorous disulfide. Oxidation of the substrate causes the polymer to change color from red to green, providing a built-in colorimetric capability. The network is also capable of catalyzing the oxidation of the HD analogue 2-chloroethyl ethyl sulfide (CEES) by hydrogen peroxide to selectively form the decontaminated sulfoxide product. Perhaps most interestingly, however, the polymer swells and forms gels when exposed to polar aprotic organic liquids, allowing the network to entrap a large amount of liquid. Notably, this occurs in dimethyl methyl phosphonate (DMMP), a simulant of OP CWAs, suggesting that this material may be useful for the entrapment of chemical warfare agents. In addition, the POM units within the polymer are doubly anionic, and the tetrabutylammonium (TBA) counter cations can be readily exchanged for a wide variety of other cations, which both changes the physical properties of the material and can add function. For example, the cations can be exchanged for tetrazirconate clusters, allowing the resulting materials to be active catalysts for the hydrolysis of OP agent analogues. This family of highly tunable materials can therefore potentially be used for both entrapment and decontamination of CWAs. Details regarding the synthesis, characterization, and catalytic activity will be discussed in detail.

In the following chapter, oxidative decontamination of CWAs will continue to be discussed. Specifically, it will detail investigations into a complex reaction system using bromine and nitrogen oxide species that rapidly and selectively oxidize sulfides to sulfoxides. This catalytic system had been investigated previously by our group, in which TBA bromide, TBA nitrate and the sulfide, CEES, were mixed in an acidic acetonitrile solution. Though this reaction goes to completion and selectively generates the sulfoxide product, it proceeds slowly and requires heat. Chapter three will discuss improvements of this system, beginning with the substitution of TBA bromide with TBA tribromide. This substitution allows the reaction to proceed to completion much

more rapidly and eliminates the need for heat. Several key reaction parameters are explored and optimized, such as the complex dependences of the reaction rate on the concentration of water, H^+, and catalytic components. Furthermore, the reaction rate can be substantially increased by the addition of copper to the system. Lastly, a catalytic system is explored in which a solid formulation incorporating the optimized reaction components are used to catalyze the oxidation of neat liquid CEES.

In the final chapter, the stability and speciation of POM WOCs will be explored. The Hill group has previously reported that the **Co_4V_2** POM is an active water oxidation catalyst.[113] However, two recent reports have been published questioning the stability of this catalyst in the basic buffered solutions that are used for the catalytic experiments, and point out the misassignment of the **Co_4V_2** ^{51}V NMR peak.[114-115] The authors of these critique papers also suggest that 100% of the observed catalytic water oxidation activity is attributed to cobalt oxides The work outlined in this chapter investigates the stability of **Co_4V_2** under different conditions by identifying and examining the correct ^{51}V NMR signal. These studies reveal that **Co_4V_2** is rapidly converted into other compounds as the pH is increased, but after this initial equilibration, the remaining amount of **Co_4V_2** remains relatively stable over a 1h timescale. This effect is pronounced at increased buffer concentration as well as decreased POM concentration. The experiments suggest that polyvanadates are formed during the decomposition of **Co_4V_2**, which rapidly complex with Co to form cobalt vanadates. Stopped-flow kinetic studies reveal that the observed water oxidation activity cannot be explained solely by the activity of $Co(II)_{aq}$, but the complexity of the system prevents a full mechanistic comprehension as well as an understanding of the relative activities of the various active catalysts in this system.

1.6 References

1. Zahnle, K.; Schaefer, L.; Fegley, B., *Cold Spring Harbor perspectives in biology* **2010,** 2 (10), a004895-a004895.

2. Tian, F.; Toon, O. B.; Pavlov, A. A.; De Sterck, H., *Science* **2005,** 308 (5724), 1014-1017.

3. Ohmoto, H.; Watanabe, Y.; Ikemi, H.; Poulson, S. R.; Taylor, B. E., *Nature* **2006,** 442, 908.

4. Schirrmeister, B. E.; Gugger, M.; Donoghue, P. C. J., *Palaeontology* **2015,** 58 (5), 769-785.

5. Lyons, T. W.; Reinhard, C. T.; Planavsky, N. J., *Nature* **2014,** 506, 307.

6. Halliwell, B., *Progress in Biophysics and Molecular Biology* **1979,** 33, 1-54.

7. Yachandra, V. K.; Sauer, K.; Klein, M. P., *Chemical Reviews* **1996,** 96 (7), 2927-2950.

8. Brocks, J. J.; Logan, G. A.; Buick, R.; Summons, R. E., *Science* **1999,** 285 (5430), 1033-1036.

9. Kopp, R. E.; Kirschvink, J. L.; Hilburn, I. A.; Nash, C. Z., *Proceedings of the National Academy of Sciences of the United States of America* **2005,** 102 (32), 11131-11136.

10. Schirrmeister, B. E.; de Vos, J. M.; Antonelli, A.; Bagheri, H. C., *Proceedings of the National Academy of Sciences* **2013,** 110 (5), 1791-1796.

11. Lyons, T. W.; Reinhard, C. T., *Nature* **2009,** 461, 179.

12. Newton, M. S.; Arcus, V. L.; Gerth, M. L.; Patrick, W. M., *Current Opinion in Structural Biology* **2018,** 48, 110-116.

13. Laidler, K. J., *Archive for History of Exact Sciences* **1986,** 35 (4), 345-374.

14. Hagen, J., *Industrial catalysis: a practical approach*. John Wiley & Sons: 2015.

15. Klugherz, P. D.; Harriott, P., *AIChE Journal* **1971,** 17 (4), 856-866.

16. ANNUAL ENERGY OUTLOOK 2018 with projections to 2050. Energy, U. S. D. o., Ed. U.S. Energy Information Administration: 2018.

17. Gavriilidis, A.; Constantinou, A.; Hellgardt, K.; Hii, K. K.; Hutchings, G. J.; Brett, G. L.; Kuhn, S.; Marsden, S. P., *Reaction Chemistry & Engineering* **2016,** 1 (6), 595-612.

18. *Global Chemicals Outlook - Towards Sound Management of Chemicals*; United Nations Environment Programme: 2013.

19. Cribb, J., *Surviving the 21st Century: Humanity's Ten Great Challenges and How We Can Overcome Them*. Springer, Cham: Canberra, Australia, 2017.

20. *Fourth National Report on Human Exposure to Environmental Chemicals*; March 2018, 2018.

21. A Prüss-Ustün, J. W., C Corvalán, R Bos, M Neira *Preventing Disease Through Healthy Environments: a global assessment of the burden of disease from environmental risks*; World Health Organization: 2016.

22. *2015 World's Worst Pollution Problems*; Green Cross Switzerland: 2015.

23. *Summary for Policymakers in IPCC, 2018: Global Warming of 1.5°C. An IPCC Special Report on the impacts of global warming of 1.5°C above pre-industrial levels and related global greenhouse emission pathways, in the context of strengthening the global response to the threat of climate change, sustainable development, and efforts to eradicate poverty*; Intergovernmental Panel on Climate Change: 2018.

24. Jay, A., D.R. Reidmiller, C.W. Avery, D. Barrie, B.J. DeAngelo, A. Dave, M. Dzaugis, M. Kolian, K.L.M. Lewis, K. Reeves, and D. Winner, *2018: Overview. In Impacts, Risks, and Adaptation in the United States: Fourth National Climate Assessment*; U.S. Global Change Research Program: Washington, DC, USA, 2018.

25. Monastersky, R., *Nature* **2014,** (516), 158–161.

26. WWF, Living Planet Report - 2018: Aiming Higher. . Grooten, M. a. A., R.E.A., Ed. WWF: Gland, Switzerland, 2018.

27. Pimm, S. L.; Jenkins, C. N.; Abell, R.; Brooks, T. M.; Gittleman, J. L.; Joppa, L. N.; Raven, P. H.; Roberts, C. M.; Sexton, J. O., *Science* **2014,** 344 (6187).

28. Oller, I.; Malato, S.; Sánchez-Pérez, J. A., *Science of The Total Environment* **2011,** 409 (20), 4141-4166.

29. Muñoz, I.; Rieradevall, J.; Torrades, F.; Peral, J.; Domènech, X., *Chemosphere* **2006,** 62 (1), 9-16.

30. Georgi, A.; Kopinke, F.-D., *Applied Catalysis B: Environmental* **2005,** 58 (1), 9-18.

31. Yang, Y. C.; Baker, J. A.; Ward, J. R., *Chem Rev* **1992,** 92 (8), 1729-1743.

32. Talmage, S. S.; Watson, A. P.; Hauschild, V.; Munro, N. B.; King, J., *Current Organic Chemistry* **2007,** 11 (3), 285-298.

33. Kim, K.; Tsay, O. G.; Atwood, D. A.; Churchill, D. G., *Chem Rev* **2011,** 111 (9), 5345-5403.

34. Kokatnur, V. R., *Journal of Chemical Education* **1948,** 25 (5), 268.

35. Fitzgerald, G. J., *American journal of public health* **2008,** 98 (4), 611-625.

36. Elmore, D. T.; Gulland, J. M.; Jordan, D. O.; Taylor, H. F., *The Biochemical journal* **1948,** 42 (2), 308-316.

37. Dacre, J. C.; Goldman, M., *Pharmacological Reviews* **1996,** 48 (2), 289-326.

38. Jang, Y. J.; Kim, K.; Tsay, O. G.; Atwood, D. A.; Churchill, D. G., *Chemical Reviews* **2015,** 115 (24), PR1-PR76.

39. Shih, T.-M.; Kan, R. K.; McDonough, J. H., *Chemico-Biological Interactions* **2005,** 157-158, 293-303.

40. Quinn, D. M., *Chemical Reviews* **1987,** 87 (5), 955-979.

41. Mondloch, J. E.; Katz, M. J.; Isley Iii, W. C.; Ghosh, P.; Liao, P.; Bury, W.; Wagner, G. W.; Hall, M. G.; DeCoste, J. B.; Peterson, G. W.; Snurr, R. Q.; Cramer, C. J.; Hupp, J. T.; Farha, O. K., *Nat Mater* **2015,** 14 (5), 512-516.

42. Munro, N. B.; Talmage, S. S.; Griffin, G. D.; Waters, L. C.; Watson, A. P.; King, J. F.; Hauschild, V., *Environmental health perspectives* **1999,** 107 (12), 933-74.

43. Walker, P. F. In *A Century of Chemical Warfare: Building a World Free of Chemical Weapons*, One Hundred Years of Chemical Warfare: Research, Deployment, Consequences, Cham, 2017//; Friedrich, B., Hoffmann, D., Renn, J., Schmaltz, F., Wolf, M., Eds. Springer International Publishing: Cham, 2017; pp 379-400.

44. Smith, B. M., *Chem Soc Rev* **2008,** 37 (3), 470-478.

45. Raushel, F. M., *Nature* **2011,** 469 (7330), 310-311.

46. Hiscock, J. R.; Bustone, G. P.; Clark, E. R., *ChemistryOpen* **2017,** 6 (4), 497-500.

47. Liu, Y.; Buru, C. T.; Howarth, A. J.; Mahle, J. J.; Buchanan, J. H.; DeCoste, J. B.; Hupp, J. T.; Farha, O. K., *Journal of Materials Chemistry A* **2016,** 4 (36), 13809-13813.

48. Wagner, G. W.; Yang, Y.-C., *Industrial & Engineering Chemistry Research* **2002,** 41 (8), 1925-1928.

49. Kumar, J. P.; P.V.R.K, R.; G.K, P.; Singh, B., *Applied Clay Science* **2015,** 116-117, 263-272.

50. Sullivan, K. P.; Neiwert, W. A.; Zeng, H.; Mehta, A. K.; Yin, Q.; Hillesheim, D. A.; Vivek, S.; Yin, P.; Collins-Wildman, D. L.; Weeks, E. R.; Liu, T.; Hill, C. L., *Chemical Communications* **2017,** 53 (83), 11480-11483.

51. Barea, E.; Montoro, C.; Navarro, J. A. R., *Chemical Society Reviews* **2014,** 43 (16), 5419-5430.

52. DeCoste, J. B.; Peterson, G. W., *Chemical Reviews* **2014,** 114 (11), 5695-5727.

53. Wagner, G. W.; Chen, Q.; Wu, Y., *J Phys Chem C* **2008,** 112 (31), 11901-11906.

54. Bandosz, T. J.; Laskoski, M.; Mahle, J.; Mogilevsky, G.; Peterson, G. W.; Rossin, J. A.; Wagner, G. W., *The Journal of Physical Chemistry C* **2012,** 116 (21), 11606-11614.

55. Sato, M., *Spec Publ-Geochemical Soc* **1990,** 2, 271-283.

56. Balsara, N. P.; Newman, J., *Journal of Chemical Education* **2013,** 90 (4), 446-452.

57. Evans, A.; Strezov, V.; Evans, T. J., *Renewable and Sustainable Energy Reviews* **2012,** 16 (6), 4141-4147.

58. Alotto, P.; Guarnieri, M.; Moro, F., *Renewable and Sustainable Energy Reviews* **2014,** 29, 325-335.

59. Larcher, D.; Tarascon, J. M., *Nature Chemistry* **2014,** 7, 19.

60. Mazloomi, K.; Gomes, C., *Renewable and Sustainable Energy Reviews* **2012,** 16 (5), 3024-3033.

61. Hunter, B. M.; Gray, H. B.; Muller, A. M., *Chemical reviews* **2016,** 116 (22), 14120-14136.

62. Jee, G.; Kambara, T.; Coleman, W., *Photochemistry and Photobiology* **1985,** 42 (2), 187-210.

63. Eberhard, S.; Finazzi, G.; Wollman, F.-A., *Annual Review of Genetics* **2008,** 42 (1), 463-515.

64. Kato, M.; Zhang, J. Z.; Paul, N.; Reisner, E., *Chemical Society Reviews* **2014,** 43 (18), 6485-6497.

65. Rappaport, F.; Guergova-Kuras, M.; Nixon, P. J.; Diner, B. A.; Lavergne, J., *Biochemistry* **2002,** 41 (26), 8518-8527.

66. Suga, M.; Akita, F.; Hirata, K.; Ueno, G.; Murakami, H.; Nakajima, Y.; Shimizu, T.; Yamashita, K.; Yamamoto, M.; Ago, H.; Shen, J.-R., *Nature* **2014,** 517, 99.

67. Umena, Y.; Kawakami, K.; Shen, J.-R.; Kamiya, N., *Nature* **2011,** 473, 55.

68. Yano, J.; Yachandra, V., *Chemical Reviews* **2014,** 114 (8), 4175-4205.

69. Blakemore, J. D.; Crabtree, R. H.; Brudvig, G. W., *Chemical Reviews* **2015,** 115 (23), 12974-13005.

70. Krewald, V.; Retegan, M.; Cox, N.; Messinger, J.; Lubitz, W.; DeBeer, S.; Neese, F.; Pantazis, D. A., *Chemical Science* **2015,** 6 (3), 1676-1695.

71. Alstrum-Acevedo, J. H.; Brennaman, M. K.; Meyer, T. J., *Inorganic Chemistry* **2005,** 44 (20), 6802-6827.

72. Sarkar, S.; Peter, S. C., *Inorganic Chemistry Frontiers* **2018,** 5 (9), 2060-2080.

73. Gagliardi, C. J.; Vannucci, A. K.; Concepcion, J. J.; Chen, Z.; Meyer, T. J., *Energy & Environmental Science* **2012,** 5 (7), 7704-7717.

74. Man, I. C.; Su, H.-Y.; Calle-Vallejo, F.; Hansen, H. A.; Martínez, J. I.; Inoglu, N. G.; Kitchin, J.; Jaramillo, T. F.; Nørskov, J. K.; Rossmeisl, J., *ChemCatChem* **2011,** 3 (7), 1159-1165.

75. Lv, H.; Geletii, Y. V.; Zhao, C.; Vickers, J. W.; Zhu, G.; Luo, Z.; Song, J.; Lian, T.; Musaev, D. G.; Hill, C. L., *Chemical Society Reviews* **2012,** 41 (22), 7572-7589.

76. Roger, I.; Shipman, M. A.; Symes, M. D., *Nature Reviews Chemistry* **2017,** 1, 0003.

77. Miras, H. N.; Yan, J.; Long, D.-L.; Cronin, L., *Chemical Society Reviews* **2012,** 41 (22), 7403-7430.

78. Wang, S.-S.; Yang, G.-Y., *Chemical Reviews* **2015,** 115 (11), 4893-4962.

79. Hill, C. L., *Chemical Reviews* **1998,** 98 (1), 1-2.

80. Pope, M. T.; Müller, A., *Angewandte Chemie International Edition in English* **1991,** 30 (1), 34-48.

81. Long, D.-L.; Tsunashima, R.; Cronin, L., *Angewandte Chemie International Edition* **2010,** 49 (10), 1736-1758.

82. Song, Y.-F.; Tsunashima, R., *Chemical Society Reviews* **2012,** 41 (22), 7384-7402.

83. Zhang, B.; Yin, P.; Haso, F.; Hu, L.; Liu, T., *Journal of Cluster Science* **2014,** 25 (3), 695-710.

84. Proust, A.; Matt, B.; Villanneau, R.; Guillemot, G.; Gouzerh, P.; Izzet, G., *Chemical Society Reviews* **2012,** 41 (22), 7605-7622.

85. Miao, W.-K.; Yan, Y.-K.; Wang, X.-L.; Xiao, Y.; Ren, L.-J.; Zheng, P.; Wang, C.-H.; Ren, L.-X.; Wang, W., *ACS Macro Letters* **2014,** 3 (2), 211-215.

86. Dolbecq, A.; Dumas, E.; Mayer, C. R.; Mialane, P., *Chemical Reviews* **2010,** 110 (10), 6009-6048.

87. Nicole, L.; Laberty-Robert, C.; Rozes, L.; Sanchez, C., *Nanoscale* **2014,** 6 (12), 6267-6292.

88. Diaz, U.; Brunel, D.; Corma, A., *Chemical Society Reviews* **2013,** 42 (9), 4083-4097.

89. Jung, J. H.; Lee, J. H.; Silverman, J. R.; John, G., *Chemical Society Reviews* **2013,** 42 (3), 924-936.

90. Zhang, K. Y.; Liu, S.; Zhao, Q.; Huang, W., *Coordination Chemistry Reviews* **2016,** 319, 180-195.

91. Zhu, Q.-L.; Xu, Q., *Chemical Society Reviews* **2014,** 43 (16), 5468-5512.

92. He, W.-W.; Li, S.-L.; Zang, H.-Y.; Yang, G.-S.; Zhang, S.-R.; Su, Z.-M.; Lan, Y.-Q., *Coordination Chemistry Reviews* **2014,** 279, 141-160.

93. Du, D.-Y.; Qin, J.-S.; Li, S.-L.; Su, Z.-M.; Lan, Y.-Q., *Chemical Society Reviews* **2014,** 43 (13), 4615-4632.

94. Clerici, M. G.; Kholdeeva, O. A.; Hill, C. L., *Liquid Phase Oxidation via Heterogeneous Catalysis*. John Wiley & Sons, Inc.: 2013.

95. Xiao, Z.; Chen, K.; Wu, B.; Li, W.; Wu, P.; Wei, Y., *European Journal of Inorganic Chemistry* **2016,** 2016 (6), 808-811.

96. Wu, H.; Yang, H.-K.; Wang, W., *New Journal of Chemistry* **2016,** 40 (2), 886-897.

97. Hu, M.-B.; Xia, N.; Yu, W.; Ma, C.; Tang, J.; Hou, Z.-Y.; Zheng, P.; Wang, W., *Polymer Chemistry* **2012,** 3 (3), 617-620.

98. Rieger, J.; Antoun, T.; Lee, S.-H.; Chenal, M.; Pembouong, G.; Lesage de la Haye, J.; Azcarate, I.; Hasenknopf, B.; Lacôte, E., *Chemistry – A European Journal* **2012,** 18 (11), 3355-3361.

99. Macdonell, A.; Johnson, N. A. B.; Surman, A. J.; Cronin, L., *Journal of the American Chemical Society* **2015,** 137 (17), 5662-5665.

100. Xu, L.; Lu, M.; Xu, B.; Wei, Y.; Peng, Z.; Powell, D. R., *Angewandte Chemie International Edition* **2002,** 41 (21), 4129-4132.

101. Wang, R.; Li, Y.; Shetye, K.; Dutta, T.; Jin, L.; Li, S.; Peng, Z., *European Journal of Inorganic Chemistry* **2015,** 2015 (4), 656-663.

102. Haso, F.; Wang, R.; He, J.; Luo, J.; Eghtesadi, S. A.; Peng, Z.; Liu, T., *New Journal of Chemistry* **2016,** 40 (2), 910-913.

103. Kang, J.; Xu, B.; Peng, Z.; Zhu, X.; Wei, Y.; Powell, D. R., *Angewandte Chemie International Edition* **2005,** 44 (42), 6902-6905.

104. Tong, U.; Chen, W.; Ritchie, C.; Wang, X.; Song, Y.-F., *Chemistry – A European Journal* **2014,** 20 (6), 1500-1504.

105. Omwoma, S.; Gore, C. T.; Ji, Y.; Hu, C.; Song, Y.-F., *Coordination Chemistry Reviews* **2015,** 286, 17-29.

106. Hiskia, A.; Troupis, A.; Antonaraki, S.; Gkika, E.; Papaconstantinou, P. K. E., *International Journal of Environmental Analytical Chemistry* **2006,** 86 (3-4), 233-242.

107. Doring, A.; Birnbaum, W.; Kuckling, D., *Chemical Society Reviews* **2013,** 42 (17), 7391-7420.

108. Sumliner, J. M.; Lv, H.; Fielden, J.; Geletii, Y. V.; Hill, C. L., *European Journal of Inorganic Chemistry* **2014,** 2014 (4), 635-644.

109. Geletii, Y. V.; Botar, B.; Kögerler, P.; Hillesheim, D. A.; Musaev, D. G.; Hill, C. L., *Angewandte Chemie International Edition* **2008,** 47 (21), 3896-3899.

110. Yin, Q.; Tan, J. M.; Besson, C.; Geletii, Y. V.; Musaev, D. G.; Kuznetsov, A. E.; Luo, Z.; Hardcastle, K. I.; Hill, C. L., *Science* **2010,** 328 (5976), 342-345.

111. Lauinger, S. M.; Sumliner, J. M.; Yin, Q.; Xu, Z.; Liang, G.; Glass, E. N.; Lian, T.; Hill, C. L., *Chemistry of Materials* **2015,** 27 (17), 5886-5891.

112. Blasco-Ahicart, M.; Soriano-López, J.; Carbó, J. J.; Poblet, J. M.; Galan-Mascaros, J. R., *Nature Chemistry* **2017,** 10, 24.

113. Lv, H.; Song, J.; Geletii, Y. V.; Vickers, J. W.; Sumliner, J. M.; Musaev, D. G.; Kögerler, P.; Zhuk, P. F.; Bacsa, J.; Zhu, G.; Hill, C. L., *Journal of the American Chemical Society* **2014,** 136 (26), 9268-9271.

114. Folkman, S. J.; Finke, R. G., *ACS Catalysis* **2017,** 7 (1), 7-16.

115. Folkman, S. J.; Kirner, J. T.; Finke, R. G., *Inorganic Chemistry* **2016,** 55 (11), 5343-5355.

Chapter 2: Polyoxometalate-Based Gelating Networks for Entrapment and Catalytic Decontamination

2.1 Introduction: Multifunctional Catalytic Polymers

2.1.1 Discovery of Hexavanadate-Based Polymers

This work describes the synthesis and characterization of a family of POM-based multifunctional polymers. The initial polymer, which will be abbreviated as **TBA-polyV$_6$**, is composed of hexavanadate (V_6O_{19}) clusters bridged by 1,3,5-benzenetricarbonyl linker molecules, and was first synthesized by Huadong Zeng during his work in the Hill lab. Dr. Zeng provided a great deal of characterization of related hexavanadate-based POM organic/inorganic hybrids.[1] This polymer was particularly notable for its ability to form gels upon contact with polar aprotic organic liquids, though a thorough characterization of this effect and of the material remained elusive. The polymer was subsequently investigated by Wade Neiwert and Daniel Hillesheim, who performed studies of thiol oxidation catalyzed by the hexavanadate units within the material.[2-3] However, despite promising initial results, these investigations were not able to provide a complete picture of the system due to the significant challenge of characterizing this material, which is insoluble in all solvents tested. The research outlined in this section, therefore, describes efforts to obtain a more complete understanding of the polymer structure and further examine its catalytic activity. Through these investigations, several new and highly interesting properties of the material were revealed, and additional derivatives were made in order to enhance the various physical or catalytic properties of the material. The collective effort culminated in the first publication related to this new class of polymers.[4] These studies are addressed in this chapter.

The polymer discussed in this section is synthesized through reaction of $C_6H_3(CONHC(CH_2OH)_3)_3$ (**trisBTA**) and $(TBA)_3[H_3V_{10}O_{28}]$ in *N*,*N*-dimethylacetamide (DMA),

affording a gel material that is isolated as a red insoluble powder with the formula [(*n*-$C_4H_9)_4N]_{2n}[(V_6O_{13})_n[((OCH_2)_3CNHCO)_3C_6H_3]_x[((OCH_2)_3$-$CNHCO)_2((HOCH_2)_3CNHCO)C_6H_3]_y[(OCH_2)_3CNHCO((HOCH_2)_3CNHCO)_2C_6H_3]_z]$ (**TBA-polyV$_6$,** x = triply bound **trisBTA**, y = doubly-bound **trisBTA**, z = singly-bound **trisBTA**) (Figure 2.1). The material forms gels upon simple addition of a liquid, including the CWA analogue DMMP. This polymer and its derivatives are additionally capable of catalyzing both hydrolysis of nerve agent simulants and aerobic oxidation reactions under mild conditions. The physical and chemical properties of the polymer can be readily altered through exchange of the POM counter cations, allowing for the creation of a wide variety of new responsive and reactive materials.

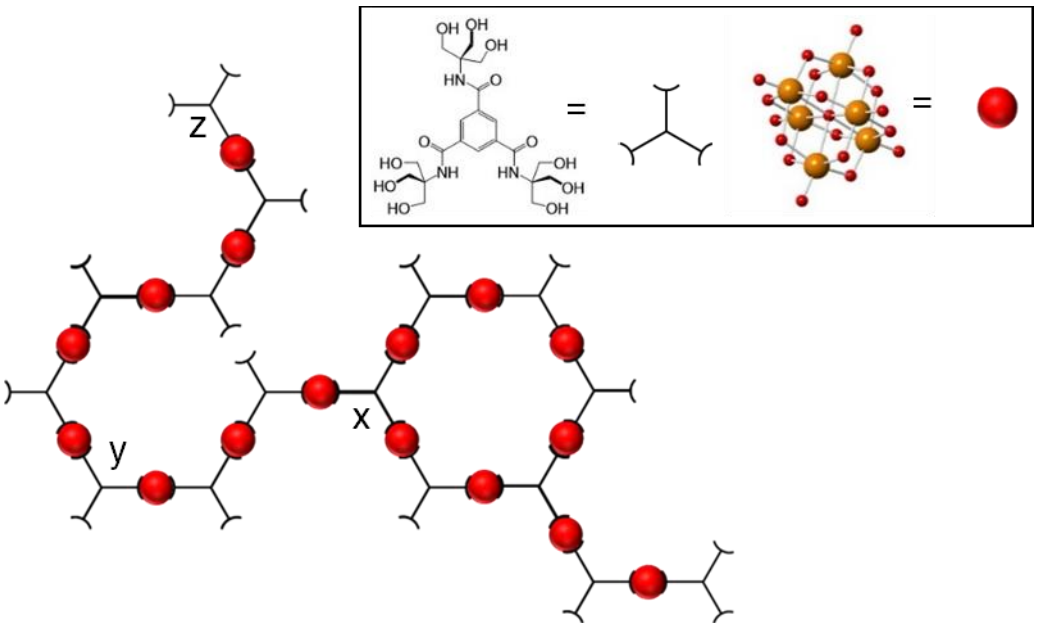

Figure 2.1. Representation of **TBA-polyV$_6$**, indicating triply-bound (x) doubly-bound (y) and singly-bound (z) linkers. Inset: representations of trisBTA and V_6O_{19}. Orange and red spheres represent V(V) and O^{2-}, respectively.

2.1.2 Hybrid Organic/Inorganic POMs

The field of organic/inorganic POMs has rapidly expanded in recent years, allowing for the development of compounds that exhibit advantages of both POMs and their organic groups.[5] In catalysis, the study of these hybrids has allowed for a greater understanding of the interactions of surface oxides with organic molecules, leading to the development of more efficient multifunctional catalysts.[6] In general, there are two primary classes of hybrid POMs; systems in which the POM is bound covalently, and those in which the POM is bound by noncovalent interactions including hydrogen bonding, van der Waals interactions, or electrostatic interactions.[7] A vast array of these hybrids have been synthesized and studied, with several reviews dedicated to describing them.[5-6, 8-12] However, few studies have investigated polymers containing POMs in the main backbone of the networks, which allows for unique polymer structures and functions to be achieved.[13-17] Two POM classes, however, have been explored for their ability to be incorporated covalently into hybrid structures: the Anderson and Lindquist POMs (Figure 1.7), as these POMs are capable of reacting with tris-alkoxide groups to form stable products.[12] Studies on the Anderson POM hybrids in particular have led to the discovery of several unique compounds, including targeted anti-tumor compounds,[18] POM-based artificial peptides,[19] single-molecule magnets,[20] and many more.[12, 21] However, the Anderson POM hybrids have not found many applications in catalysis, as the Mo atoms on the outer ring of the structure that are exposed to the solvent are typically not reactive enough to catalyze reactions of interest. This is not the case, however, with the vanadium-based Lindquist hybrid POMs, which are composed of six identical vanadium atoms esterified by two tris-triols, as shown in Figure 2.2.

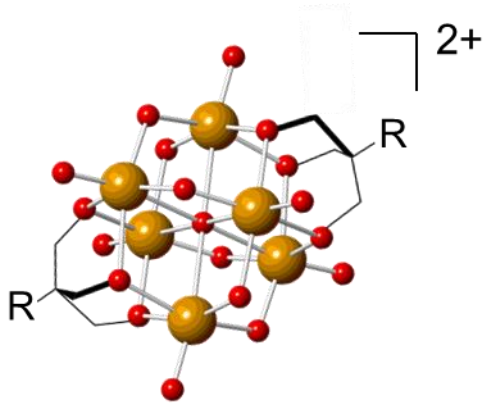

Figure 2.2. Representative structure of hybrid organic/inorganic Lindquist hexavanadate structure. Orange and red spheres represent V(V) and O^{2-}, respectively.

Though they have been less extensively explored than the Anderson POM hybrids, hexavanadates have been incorporated into a variety of systems, such as surfactants with catalytic desulfurization capabilities,[22] or POM-based coordination networks that catalyze aerobic oxidations,[23] among others.[24-26] The modular nature of these hexavanadate-Anderson hybrids allows for the directed design of molecules of interest, including the work described here in which polymers are constructed by linking together hexavanadate POMs in extended frameworks. This versatility in design and functionality allows for exciting new developments to be possible in the field of organic/inorganic hybrid materials.

2.1.3 Overview of Gels

Inorganic/organic polymers are important in multiple disciplines as they allow for synergy between the physical properties of traditional polymers and versatility in function of inorganic compounds.[27-29] As noted above, of the most intriguing aspects of the hexavanadate-based polymeric material under study is its ability to form gels upon contact with polar aprotic organic liquids. Gels are defined as substantially dilute cross-linked systems that exhibit no flow in the

steady-state.[30] They occur when polymer strands are entangled in a three-dimensional network, trapping solvents within the material.[31] Gels exhibit solid-like rheology and do not flow despite being predominately liquid in composition.[32] Supramolecular gels are formed when discrete molecular units self-assemble into nano-or micro-scale structures through noncovalent interactions (such as hydrogen bonding, π-π interactions, van der Waals forces, solvophobic effects, *etc*.), forming 3D networks consisting of cross-linked or entangled fibers.[33] They have been described as a result of "crystallization gone awry,"[32] as they depend on a complex balance between gelator aggregating forces and solubilizing solvent-aggregate interactions.[34] A subset of these are known as low molecular weight organogelators (LMWOGs), small molecules which assemble into gelating polymers.[35] LMWOGs are quite attractive in the design of new soft materials, but often require an external stimulus such as a temperature or pH change to initiate gelation. Only a small number of polymers with a permanent backbone demonstrate gelation behavior, and their gelation abilities are generally lower than LMWOGs. It is extremely challenging to predict *ab initio* which molecules or polymers will be effective gelators, making the discovery of new classes of gelators primarily a serendipitous event.[36] However once a certain class of compounds has been found to exhibit gelation behavior, these compounds can be used to design new gelators. In this way, polymers with enhanced gelation behavior have been designed by incorporating known LMWOGs into polymer backbones, including in C_3-symmetric 1,3,5-benzenetricarboxamide (BTC) derivatives.[31, 37-38] In BTC-based gelator systems, gelation primarily occurs through hydrogen-bonding and π-stacking interactions between amide N-H and carbonyl moieties on adjacent molecules, as shown in Figure 2.3.[37, 39-40]

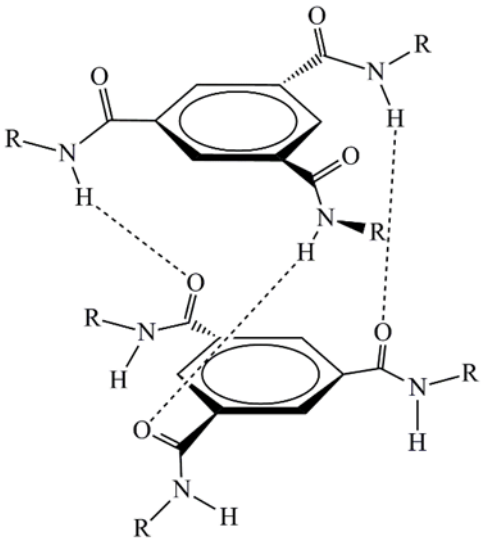

Figure 2.3. General motif of hydrogen bonding through interactions between adjacent amide moieties in 1,3,5-benzentricarboxamides.

There have been several reports of gels based on functionalized POMs in hybrid organic/inorganic systems.[41-43] However, most of these reported gelators are LMWOGs, and thus are not ideal for applications involving the entrapment and decontamination of toxic compounds. Materials that respond to external stimuli play an increasing role in a diverse range of applications, including protection against chemical or biological threats.[44-46] Polymer gelators can adsorb a large number of solvent molecules within their networks, making them attractive for use as protective materials.[44, 47-48] Development of materials for the sequestration and decontamination of CWAs, including OP nerve agents such as Sarin and VX, and blister agents such as HD, has been a priority for decades due to their high toxicity, as discussed in section 1.3.1.[49] Entrapment of CWAs by gelation has been reported in a few cases, including in several crosslinked polymer systems and LMWOG systems, where interactions between the gelators and the CWAs result in gel formation. [50-53] However, currently no materials have been developed that are able to simultaneously form gels in and decontaminate CWAs. Such a capability would represent a significant advance in the field of protective materials.

2.2 Experimental

2.2.1 General Methods

All starting materials were used as received unless otherwise specified.

Elemental analyses were performed by Galbraith Laboratories, Inc. (C, H, N) and Atlantic Microlab Inc. (V, Li, Zr).

Infrared (FT-IR) spectra were recorded using a Nicolet TM 6700 FTIR spectrometer Smart Orbit Diamond ATR accessory.

Diffuse reflectance UV/Vis studies were performed using a PerkinElmer Lambda 1050 with 150mm integrating sphere. Spectra were obtained by immobilizing powdered samples on a film and hanging it using a center mount clamp coated in Spectralon® at 0˚.

Uv/Vis measurements. All UV-Vis spectra were acquired using Agilent 8453 spectrophotometer equipped with a diode-array detector.

Z-contrast STEM images were obtained on Hitachi HD2000 scanning transmission electron microscope with 20kV accelerating voltage. TEM images were obtained a Hitachi HD2000 scanning transmission electron microscope at an accelerating voltage of 30kV. Samples were prepared by dispersing **TBA-polyV$_6$** in wet DMF and dropping on Electron Microscopy Sciences

CF200-Cu grids, followed by air drying at 40 °C for two days. Contrasts were enhanced for the entire images using Microsoft Word software.

BET isotherms were obtained using a Quantachrome NOVA2000 with N_2 as the adsorption gas.

GC data were obtained using a Hewlett Packard HP 6890 GC system equipped with a HP-5 5% phenyl methyl siloxane column.

Static Light Scattering: The solid hybrid sample was fully dissolved after the solution was put in 70 °C oven overnight. The solution was then filtered and used as stock solution. Solutions with concentrations from 0.01 mg/mL to 0.09 mg/mL in the mixed solvent were prepared. The dn/dc for the hybrid in the mixed solvent was determined to be -0.112 mL/g within the above concentration range. SLS experiments were performed at scattering angles (θ) between 30 and 100°, at 2° intervals. Solutions with concentrations of 0.90, 0.68, and 0.45 mg/mL were used. Derived from Rayleigh-Gans-Debye equation [54], a Zimm plot was used to analyze the SLS data to obtain the molecular weight of the hybrid. The average molecular weight was determined to be $(1.586\pm0.033)*10^6$ g/mol. Data were obtained using a commercial Brookhaven Instrument LLS spectrometer equipped with a solid-state laser operating at 532 nm.

XPS measurements were performed using a Thermo K-Alpha XPS. A monochromated aluminum Kα source (1486.6 eV) was used for excitation of photoelectrons. The base pressure of the analysis chamber was 10^{-7} Pa during collection. Survey scan spectra were measured over a pass energy of 200 eV at 1eV energy steps. High resolution scans were performed over a pass energy of 50 eV at

0.1 eV energy steps. Analysis of all spectra were done using CasaXPS software (version 2.3.14). A mixture of Gaussian and Lorentzian functions (GL(X%))were used to fit the high resolution peaks of V, N, and Zr. A reasonable fit was achieved using symmetric lineshapes for V(IV)2p, V(V)2p, N1s, and Br3d. Different GL parameters were used for different elements, but the same parameters were maintained across all measurements. Best fit was achieved using GL(90) for vanadium, GL(56) for nitrogen, GL(30) for oxygen, and GL(80) for bromine. Fitting constraints were applied in such a manner as to be chemically sensible. Doublet peaks for bromide were fit using a separation of 1.05 eV and a ratio of 3:2 between the 3d5/2 and the 3d3/2 peaks; doublet peaks for V(IV) and V(V) were fit using a separation of 7.33 eV and a ratio of 2:1 between the 2p3/2 and the 2p1/2 peaks; doublet peaks for Br were fit using a separation of 1.05 eV and a ratio of 3:2 between the 3d5/2 and the 3d3/2 peaks. V2p was recorded along with O1s, follow up analysis were also performed with a single Shirley baseline across the entire region. O1s peaks were fitted with the assumption that an insignificant amount of adventitious carbon is present on the powdered samples. The stoichiometry of the oxygen species in the linker are preserved in the fit. All measurements were done on dried powders of V_6O_{13} polymers. Samples were standardized against V_2O_5 and TBA(PF_6) powder. All samples were vacuum dried via Schlenk line at 60 °C before introduction into the XPS chamber. The Thermo K-Alpha flood gun was used for charge neutralization during all experiments. Standard deviations of peak fitting parameters were obtained from an analysis of the error matrix generated using a Monte Carlo simulation on the relevant data sets.

Solution ^{31}P NMR spectroscopic measurements were made on a Varian INOVA 600 MHz spectrometer and resonance signals were referenced to 85% H_3PO_4 in H_2O. T_1 = 3.1s, d1 = 15, and

no ^{1}H decoupling was used. Solution ^{1}H spectroscopic measurements were made on a Varian INOVA 600 MHz spectrometer.

Solid-state cross-polarization magic angle spinning (CP-MAS) ^{13}C spectra were collected on a BRUKER Avance 600 with ^{13}C frequency of 150.918 MHz and an HCN biosolids probe and MAS speed of 10kHz with 500μs of ^{1}H-^{13}C cross-polarization followed by a Hahn-echo π-pulse of 4μs with 125kHz SPINAL64 ^{1}H (600.13 MHz) decoupling.[55] Dipolar dephasing spectra collected in the absence of ^{1}H decoupling with 50 μs of ^{1}H-^{13}C cross-polarization.

CP-MAS and Hahn-echo ^{13}C (75.48 MHz) spectra were collected on a BRUKER Avance III 300 with an HCN biosolids probe and MAS speed of 13.5 kHz. CP-MAS spectra were collected with 250μs of ^{1}H -^{13}C cross-polarization followed by a Hahn-echo π-pulse of 6μs. Hahn-echo ^{13}C spectra were collected with excitation of all ^{13}C resonances with a 3 μs π/2-pulse followed by a Hahn-echo π-pulse of 6 μs. The relaxation delay for the ^{13}C Hahn-echo spectra was determined by measuring the ^{13}C T_1 with the Torcha method via CP-MAS.[56] All spectra were collected with 100kHz SPINAL64 ^{1}H (300.13 MHz) decoupling. ^{13}C chemical shifts are referenced externally to TMS using adamantane as a secondary reference.[57]

^{51}V NMR: Solution (157.65MHz) ^{51}V NMR spectrum of **TBA-polyV$_6$**. Spectra were collected on a Varian INOVA 600. 20,000 scans were collected on **TBA-polyV$_6$** gel in DMF for the solution spectrum with a single broad (~15 ppm fwhm) peak at -499ppm. Spectra were processed with 2000 Hz exponential line broadening that matched the signal decay in the FID. Peaks were referenced to $VOCl_3$. The broad peak in the solution spectrum is consistent with reduced motion expected for

a gel. Solid-state ^{51}V (78.90 MHz) NMR spectra of **TBA-polyV$_6$** were collected at room temperature with a Bruker 4mm HX magic-angle spinning (MAS) probe and a Bruker Avance III 300 spectrometer. Spectra were measured using a rotor synchronized solid-echo with ^{51}V pulse widths of 1.4μs at multiple MAS speeds (6, 8 and 10 kHz) to identify the center band. Spectra with and without ^{1}H decoupling were identical. Chemical shift is referenced externally to $VOCl_3$ using V_2O_5 as a secondary reference at -609 ppm.[58]

Image analysis for swelling rate was obtained using a Leica DM4500B bright-field microscope equipped with a COHU solid state CCD camera. A 10X objective lens was used. For the analysis of swelling rate for Figure 2c, a sample of powdered **TBA-polyV$_6$** was placed on a glass slide followed by addition of dimethylformamide and particle area was tracked over time. In each case, particle size analysis was conducted using IDL routine methods developed by J. Crocker and D. Grier,[59] and images were processed using ImageJ software.

2.2.2 Synthesis of Hexavanadate Materials

Tetrabutylammonium decavanadate ($[(n\text{-}C_4H_9)_4N]_3[H_3V_{10}O_{28}]$) was synthesized according to reported literature procedures.[60] Synthesis of $[(n\text{-}C_4H_9)_4N]_2[(V_6O_{13})[((OCH_2)_3CNH_2]_2$ **(NH_2V_6)** was also carried out according to reported literature procedures.[61]

Synthesis of $C_6H_3(CONHC(CH_2OH)_3)_3$ (trisBTA). Tris(hydroxymethyl)aminomethane (4.54 g, 37.5 mmol) was dissolved in dry DMA under argon with mild heating. The solution was cooled to 0 ºC, followed by the addition of triethylamine (38 mmol). Trimesic acid trichloride (3.32 g, 12.5 mmol) dissolved in dry DMA was transferred dropwise under argon to the solution. The resulting

clear, yellow solution was heated to room temperature and was stirred under argon overnight. A yellow/white precipitate was isolated via filtration, concentrated *in vacuo*, redissolved in warm water and stored at 10 ºC overnight. The resulting white precipitate (1.34 g, 21% yield) was collected via vacuum filtration. Formation of the product was confirmed by comparisons with literature reports.[62] ^{1}H NMR in DMSO-d_6, ppm (assignment in italics, multiplicity, intensity): 8.25 (C_6H_3, s, 3H); 7.55 (CONHC, s, 3H); 4.74 (CH_2OH, t, 9H); 3.71 (CH_2OH, s, 18H). ^{13}C NMR in DMSO-d_6, ppm (assignment in italics): 166 (NH*C*); 135, 129 (C_6H_3); 63 ($HOCH_2C$); 60 ($HOCH_2$).

Synthesis of TBA-polyV$_6$. The **trisBTA** linker ($C_6H_3(CONHC(CH_2OH)_3)_3$, 1.00 g, 1.9 mmol) was dissolved in dry DMA under argon with mild heating. Tetrabutylammonium decavanadate ($[(n\text{-}C_4H_9)_4N]_3[H_3V_{10}O_{28}]$, 3.25 g,1.9 mmol) dissolved in dry DMA was transferred to the **trisBTA** solution under argon via cannula. The resulting clear, orange solution was stirred at 80 °C in the dark for one week, resulting in a green gel. The reaction mixture was cooled to room temperature and Et_2O was added, resulting in brown particles in a dark green solution. The solid was purified by repeated swelling in DMF, centrifugation and removal of the green supernatant, followed by contraction in Et_2O and removal of the supernatant. This process was repeated until the decanted liquid was colorless, affording a red solid powder (2.37 g). This was ground into a fine powder using a Wig-L-Bug® instrument, followed by additional swelling and contraction steps until the supernatant was colorless. $[(n\text{-}C_4H_9)_4N]_{2n}[(V_6O_{13})_n[((OCH_2)_3CNHCO)_3C_6H_3]_x[((OCH_2)_3CNHCO)_2((HOCH_2)_3CNHCO)C_6H_3]_y[(OCH_2)_3CNHCO((HOCH_2)_3CNHCO)_2C_6H_3]_z]$ (**TBA-poly$_6$**, x = triply bound linkers, y = doubly-bound linkers, z = singly-bound linkers). Solution ^{51}V NMR (ppm): -501. Solid-state CP-MAS ^{51}V NMR (ppm): -506. Solid-state CP-MAS ^{13}C NMR, ppm (assignment in italics): 166 (NH*C*);

136, 130 (C_6H_3); 84 ($VOCH_2$); 63 ($HOCH_2C$); 58 ($HOCH_2$); 54, 25, 20, 14 ((n-$C_4H_9)_4N$). EA (wt% found): C (38.15), H (6.255), N (4.095), V (20.29).

Cation exchange to form Li-polyV$_6$ and Zr-polyV$_6$. A sample of **TBA-polyV$_6$** in a Pasteur pipette containing glass wool at its base was washed with CH_3CN. A solution of 0.1 M $LiBF_4$ in CH_3CN was eluted through the column, replacing the TBA^+ cations with Li^+. To ensure that the exchange was complete, the eluent was collected, evaporated to dryness by rotary evaporation, and dried *in vacuo*, followed by extraction of the $TBABF_4$ with 1,4-dioxane. This solution was filtered, the solvent was removed by rotary evaporation and the resulting solid was dried *in vacuo*. The presence of TBA^+ was confirmed by observing the C-H stretching bands via FT-IR. Elution with the $LiBF_4$ solution was repeated until no C-H stretching bands in the eluent were observed using this method. The resulting product (**Li-polyV$_6$**) in the column was washed with several volumes of CH_3CN to remove excess $LiBF_4$. The same process was repeated using a 0.1 M solution of zirconyl chloride in CH_3CN/H_2O to obtain **Zr-polyV$_6$**.

Li-polyV$_6$, EA (wt%): C (18.71), H (3.575), N (3.17), Li (1.09), V (25.4). **Zr-polyV$_6$**, EA (wt% found): C (11.91), H (1.89), N (3.56), V (16.2), Zr (17.8).

2.2.3 Conditions for Catalytic Reactions

Oxidation of propane thiol (PrSH) catalyzed by TBA-polyV$_6$. A sample of **TBA-polyV$_6$** (7.6 mg; 5.4 µmol based on V_6 units) was added to 3.0 mL of 95% DMF / 5% H_2O. The solution was purged with O_2 for 15 minutes, and 1,3-dichlorobenzene internal standard (40 µL, 120 mM) and 1-propanethiol (60 µL, 220mM) were added. The molar ratio was 130 PrSH per V_6 unit. Reactions

were monitored by GC analysis of PrSH and PrSSPr. A control reaction was run under the same conditions but without **TBA-polyV$_6$**.

Oxidation of CEES catalyzed by TBA-polyV$_6$. A sample of **TBA-polyV$_6$** (3.3 μmol based on V_6 units) was added to 1.5 mL of MeOH and was stirred for 1 hour to disperse particles. The 1,3-dichlorobenzene internal standard was added (20 μL), followed CEES (48 μL, 411 μmol). The zero time point was taken immediately after addition of CEES to the reaction mixture, followed by addition of a solution of 30% w/w H_2O_2 (48 μL, 411 μmol) to initiate the reaction. Conversion to product was monitored by GC analysis of the CEES peak. A control reaction was run under the same conditions but without **TBA-polyV$_6$**. Each reaction was run in triplicate to obtain standard deviations.

The selectivity for 2-chloroethyl ethyl sulfoxide (CEESO) over 2-chloroethyl ethyl sulfone ($CEESO_2$) was determined using ^{1}H NMR of the reaction mixture before and after the reaction. Conditions: 3.3 μmol **TBA-polyV$_6$** (based on V_6 units) was added to a 1.5 mL deuterated methanol and stirred for 1 hour. The 1,3-dichlorobenzene internal standard was added (20 μL), followed CEES (48 μL, 411 μmol). The first NMR aliquot was taken and the ^{1}H spectrum was obtained. After this, a solution of 30% w/w H_2O_2 was added to initiate the reaction. After 40 minutes, the second NMR aliquot was taken and its ^{1}H spectrum was obtained.

Oxidation of CEES catalyzed by TBA-polyV$_6$, Li-polyV$_6$, and Zr-polyV$_6$. A sample of **TBA-polyV$_6$, Li-polyV$_6$, and Zr-polyV$_6$** (3.3 μmol based on V_6 units) was added to 1.5 mL of MeOH and was stirred for 1 hour to disperse particles. The 1,3-dichlorobenzene internal standard was

added (20 µL), followed 15 µL 30% aqueous H_2O_2 solution (30% aqueous solution, 140 µmol H_2O_2). Lastly, 16 µL CEES (137 µmol) was added initiate the reaction, and the zero time point was taken immediately after addition of CEES to the reaction mixture. Conversion to product was monitored by GC analysis of the CEES peak. A control reaction was run under the same conditions but without **TBA-polyV$_6$**. Each reaction was run in triplicate to obtain standard deviations.

Hydrolysis of DECP catalyzed by TBA-polyV$_6$. **TBA-polyV$_6$** (3.3 µmol based on V_6 units) was dispersed in 3.0 mL DMF by stirring overnight, then 600 µL of this dispersion was put into a high-pressure NMR tube, followed by addition of 10 µL of diethyl cyanophosphonate (66 µmol) and 50 µL of water (900 µmol) to initiate the reaction. Reaction progress was monitored by ^{31}P NMR. The control reaction was run using the same method but without **TBA-polyV$_6$**.

Hydrolysis of DMNP catalyzed by Zr-polyV$_6$. A sample of **Zr-BTAV$_6$** (5 mg, 2.45 µmol based on Zr_4 clusters) was added to a vial containing 1.0 mL aqueous *N*-ethylmorpholine buffer at pH = 10.00 and stirred for 1 hour to disperse the powder. To initiate the reaction, dimethyl *p*-nitrophenylphosphate (DMNP) was added (4 µL, 25 µmol), and reaction progress was monitored by UV/Vis of the *p*-nitrophenolate anion product at 407 nm. Control reactions were run under identical conditions but without the catalyst. Reactions were run in triplicate to obtain standard deviations. Filtration control to test for heterogeneity of the system was done using similar conditions, except all reagents other than DMNP were added to the reaction mixture and were stirred for 2 hours before filtration using 0.2 µm syringe filters. The supernatant was collected and 4 µL (25 µmol) DMNP were added to initiate the reaction.

2.2.4 Gelation Studies

The swelling behavior of **TBA-polyV$_6$** and **Li-polyV$_6$** in various solvents was measured by adding 5 mL of liquid to the solid polymer (~25 mg) and allowing it to gel for 24 hours. Glass wool was inserted into a glass Pasteur pipet to create a filter, and this pipet was weighed. The gel was placed in the pipet and the excess solvent filtered through while the gel was retained on the glass wool barrier. The pipet containing the gel was then weighed to determine the amount of liquid immobilized by the solid gel material. Each experiment was repeated in triplicate to determine the standard deviation.

2.3 Results and Discussion

2.3.1 Characterization

Due to the insoluble nature of **TBA-polyV$_6$**, characterization of the material presented a significant challenge as solution-based techniques for analysis could not be used. However, a variety of solid-state NMR techniques were performed which provided a great deal of insight into the composition of the polymer. Firstly, solid-state ^{51}V NMR confirmed the presence of V_6O_{19} clusters within the solid material by revealing a peak centered at -506 ppm with associated spinning sidebands (Figure 2.4).

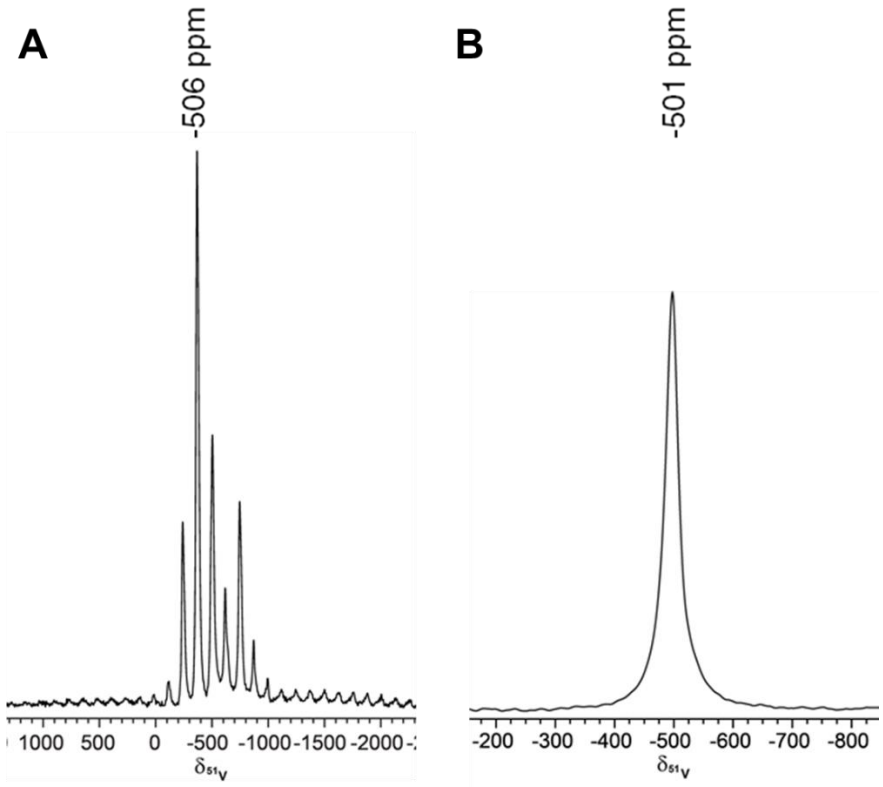

Figure 2.4. ^{51}V NMR characterization of **TBA-polyV$_6$**. (**A**) Solid-state magic-angle spinning ^{51}V NMR spectrum of **TBA-polyV$_6$** powder. The center band was located by spinning at multiple magic-angle spinning speeds, indicating the presence of one peak in the spectrum with its associated spinning sidebands. (**B**) Solution ^{51}V NMR spectrum of **TBA-polyV$_6$** in the gel phase when dispersed in *N*,*N*-dimethylformamide.

A single peak in the solution ^{51}V NMR of the polymer swollen in dimethylformamide (DMF) appears at -500 ppm and is consistent with the presence of intact hexavanadate units containing symmetrical triester groups of the resulting **TBA-polyV$_6$**.[26] Unlike many other hexametalates, the hexavanadate anion is not stable in the absence of bis-triester units, so a single peak in this spectrum is consistent with the presence of discrete hexavanadate clusters.[63]

Infrared spectroscopy determined the V-O stretching frequencies to be consistent with the known monomeric analogue $[(n\text{-}C_4H_9)_4N]_2[(V_6O_{13})[((OCH_2)_3CNH_2]_2$ **(NH_2V_6)** (Figure 2.5).[64]

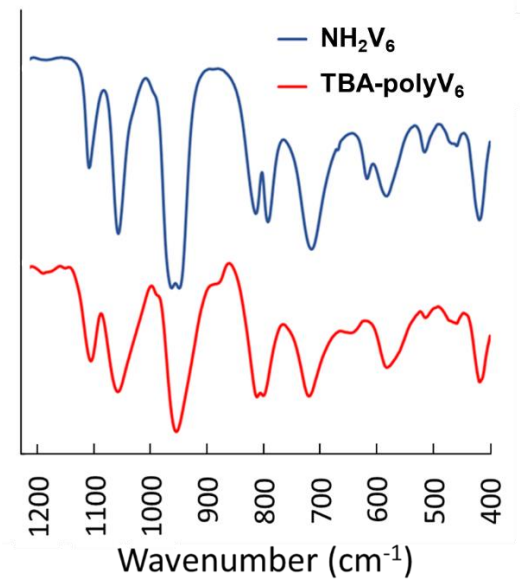

Figure 2.5. ATR FT-IR spectra of **TBA-polyV$_6$**. **TBA-polyV$_6$** (●) and the known monomeric species **NH$_2$V$_6$** (●). Peaks at 950, 810, 790, 715 are attributed to V-O vibrations.[65] The peaks in the V-O stretching frequency region agree well with reported literature values and with the known monomer **NH$_2$V$_6$**, revealing that the hexavanadate core is intact in **TBA-polyV$_6$**.

Together, these studies confirm that the **TBA-polyV$_6$** material contains intact V_6O_{19} units. In order to verify the presence of **trisBTA** linkers in the polymer, solid-state cross-polarization magic angle spinning (SS CP-MAS) ^{13}C NMR was performed on **TBA-polyV$_6$**. In a cross-polarization experiment, the NMR signal intensity will depend on the transfer of magnetization from proton to carbon nuclei. A rapid increase in signal is observed for carbon nuclei directly attached to a proton, whereas a slow increase in signal is observed for non-protonated carbon nuclei. This signal will then decay based on the environment of the carbon nucleus.[66] In order to obtain quantitative peak areas from the spectrum, a calibration experiment correlating contact time (the time during which magnetization is transferred from ^1H to ^{13}C) to peak height is required. This experiment suggests that a 500 ms delay must be used when detecting the signal for adequate buildup of the nonprotonated carbon peaks (Figure 2.6). Additionally, measurement of the magnetization decay was required to account for the increased decay rate of nuclei near the POM, as proximity to the

vanadium nuclei increases the rate of magnetization decay via quadrupolar coupling. These calibration experiments allowed us to obtain an accurate integration of the signals.

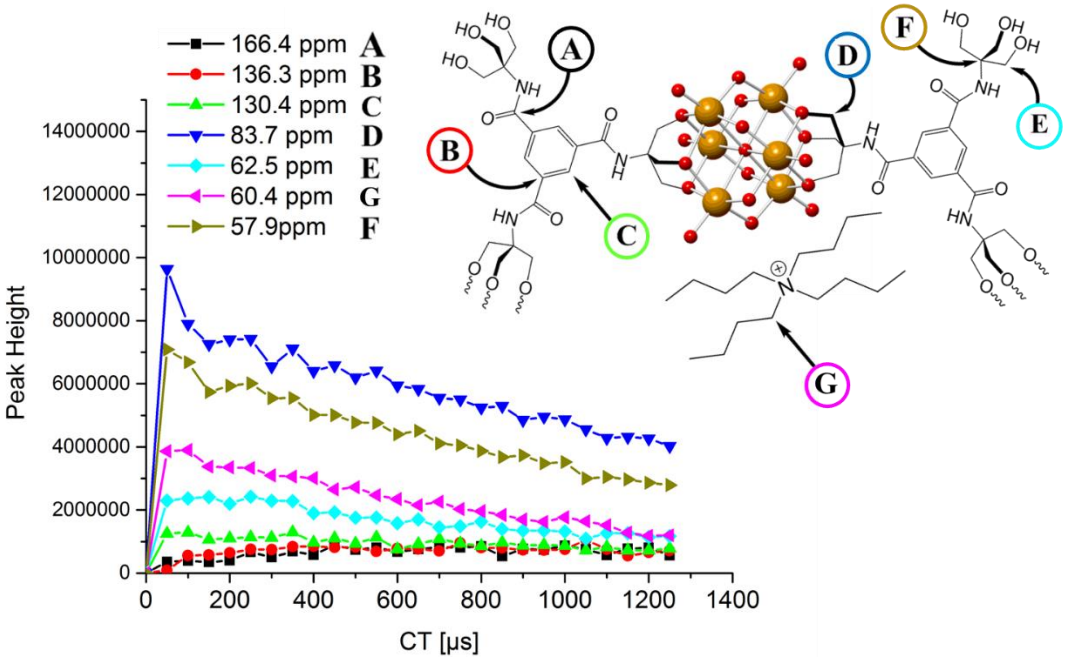

Figure 2.6. ^{13}C SSCP-MAS NMR calibration correlating peak height and contact time (CT). Peak assignments are shown on a representative **TBA-polyV$_6$** unit. Orange and red spheres represent V(V) and O^{2-}, respectively. Peaks that rise in intensity quickly are representative of carbon nuclei near proton nuclei.

Using the optimized contact time parameters, a ^{13}C SS CP-MAS NMR spectrum of **TBA-polyV$_6$** was obtained and is shown in Figure 2.7.

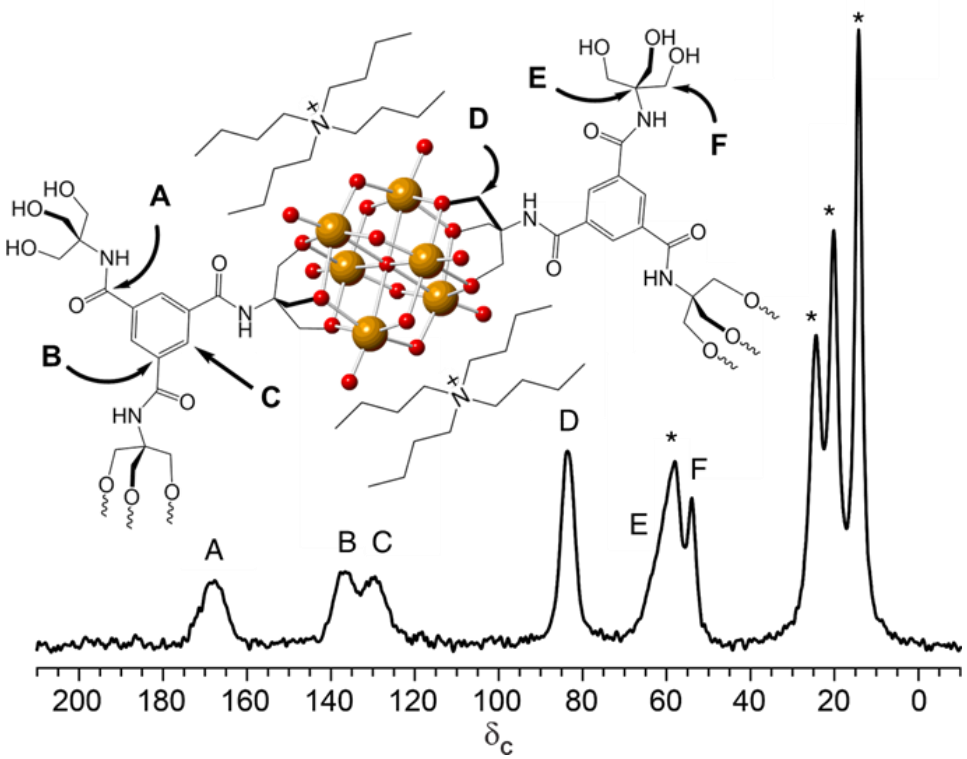

Figure 2.7. Solid-state magic-angle spinning ^{13}C NMR of **TBA-polyV$_6$**. TBA^+ (*) peaks are indicated. Orange and red spheres represent V(V) and O^{2-}, respectively.

After obtaining the spectrum, it was necessary to assign the peaks. Comparisons were made to the solution ^{13}C NMR spectrum of the **trisBTA** linker, shown in Figure 2.8. The slight deviations in chemical shift values between the solution and solid-state spectra can be attributed to the effect of solvent molecules on the solution spectra.

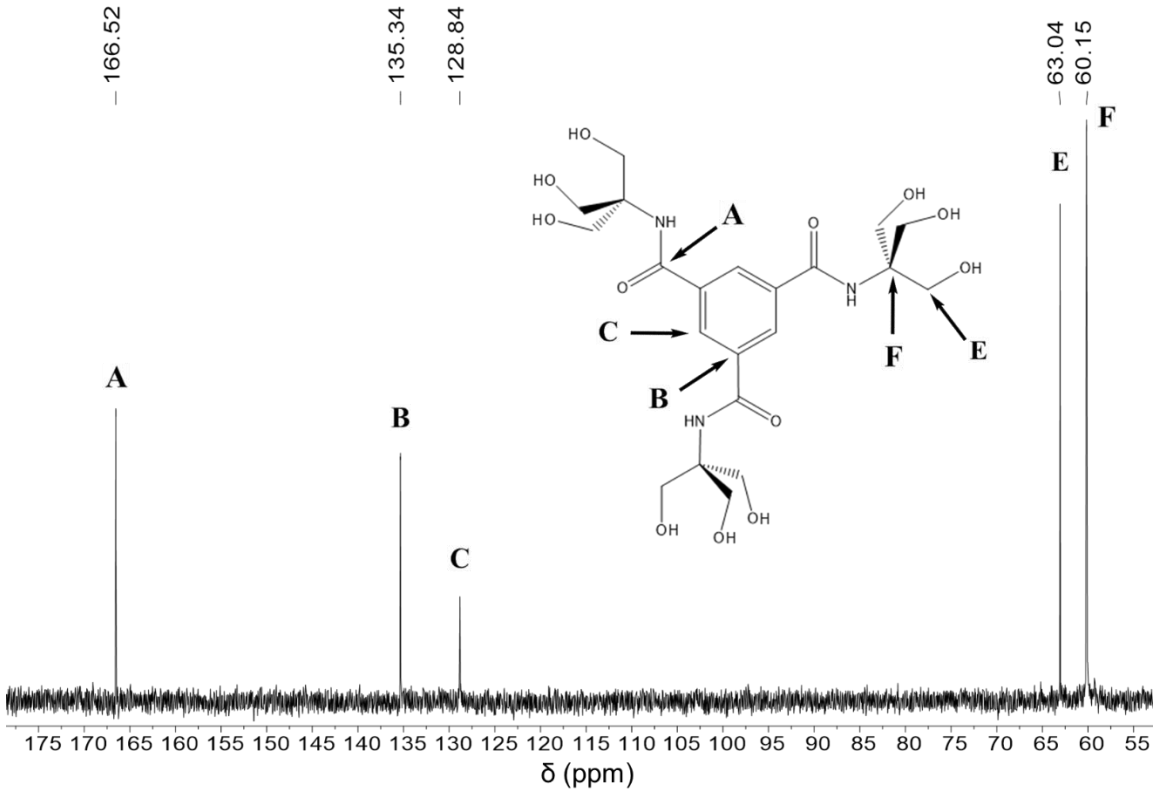

Figure 2.8. Solution ^{13}C NMR of **trisBTA** in dimethyl sulfoxide-d_6.

Comparison with the **trisBTA** spectrum, in combination with the information revealing the peaks located near protons from the contact time experiments in Figure 2.6, suggests the peak assignments shown in Table 2-1.

Table 2-1. Chemical shifts and assignments for **TBA-polyV$_6$** and **trisBTA**.

Chemical Shift **TBA-polyV$_6$** (ppm)	Chemical Shift **trisBTA** (ppm)	Assignment
166.4	166.5	benzamide (A)
136.3	135.3	benzamide (B)
130.4	128.8	benzamide (C)
83.7	N/A	V-bound tris(triol) (D)
62.5	63.0	tris(triol) methylene (E)
57.9	60.2	tris(triol) quaternary (F)

To further confirm the identity of the peaks (particularly because E, F, and one of the TBA^+ peaks are quite close in chemical shift and require peak deconvolution to separate) a dipolar dephasing CP-MAS ^{13}C NMR experiment was performed, which eliminates any signals from carbon nuclei that exhibit strong dipolar coupling with proton nuclei (Figure 2.9). In this experiment, a delay is added before the acquisition of the NMR signal after the contact time has ended. The signals for carbon nuclei with strong coupling to proton nuclei will relax more quickly, resulting in their signal being lost in the resulting spectrum. This analysis definitively identified the peak at 62.5 ppm as the triol quaternary carbon and the peak at 57.9 ppm as the free triol methylene carbon.

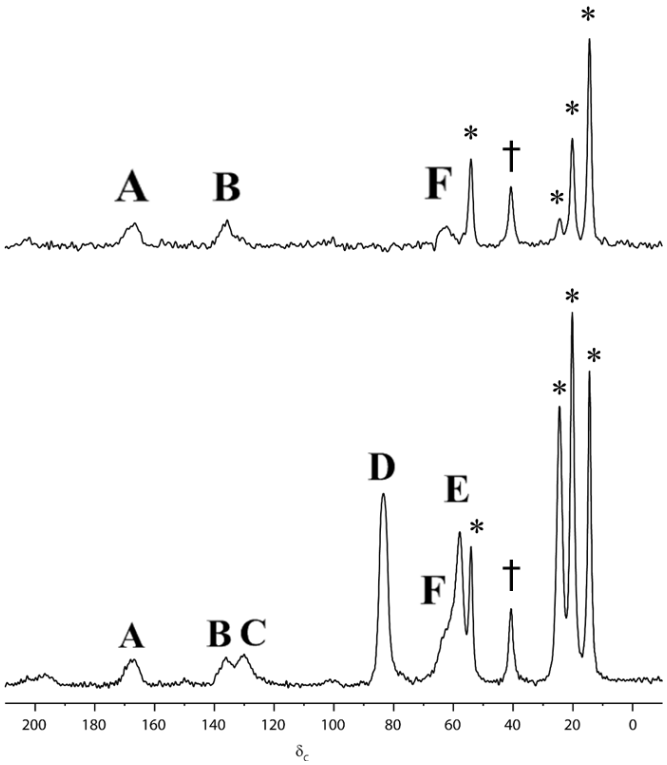

Figure 2.9. Dipolar dephasing ^{13}C CP-MAS solid-state NMR experiment on **TBA-polyV$_6$**. Spectra are shown without (bottom) and with (top) 40μs dipolar dephasing. TBA^+ peaks (*) and residual DMSO peak (†) are present in the dipolar dephased spectrum, consistent with their increased mobility resulting in motion-averaging of the ^{13}C-^{1}H dipolar coupling.

One notable result is the observance of a peak in the spectrum of **TBA-polyV$_6$** which is not present in the spectrum of the **trisBTA** linker: the peak at 83.7 ppm. This signal is attributed to the POM-bound methylene carbon, which undergoes a significant chemical shift due to its proximity to the quadrupolar vanadium nuclei. Analyzing the ratio of POM-bound to free triol groups allows for greater insight into the composition of the polymer. To do this, quantitative ^{13}C solid-state NMR was conducted without cross-polarization to determine the relative peak areas, as direct excitation of the ^{13}C resonances with a Hahn-echo ensures that the spectral intensities are directly related to relative ^{13}C concentration. (Figure 2.10).

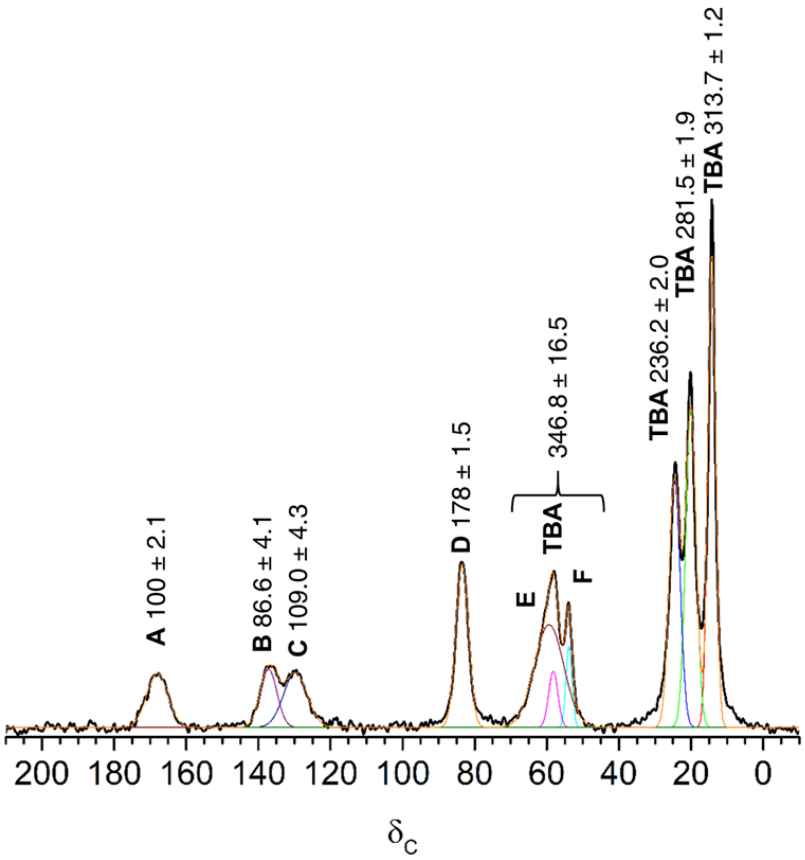

Figure 2.10. Peak deconvolution of the ^{13}C Hahn-echo natural abundance solid-state spectrum of **TBA-polyV$_6$**. Due to overlap of the peaks in the 50-70 ppm range, alternate methods were used to estimate the ratios of the peaks in this region. The ratios of peaks A (amide carbon), B, C (aromatic carbons), and E (quaternary carbon) should be identical based on the molecular structure. We therefore took the average of A, B, and C, and assumed E to be equal to that value (98.53). Additionally, the sum of D (vanadium-bound methylene carbon) and F (unbound methylene carbon) should be equal to three times E. We can therefore solve for the value of F (117.6).

Deconvolution of these peaks estimates a ratio of 3 hexavanadate-bound to 2 unbound methylene carbons. Additionally, deconvolution of the carbon and nitrogen peaks obtained from XPS data determined a ratio of 1.1 V_6 units per **trisBTA** linker (Figure 2.11).

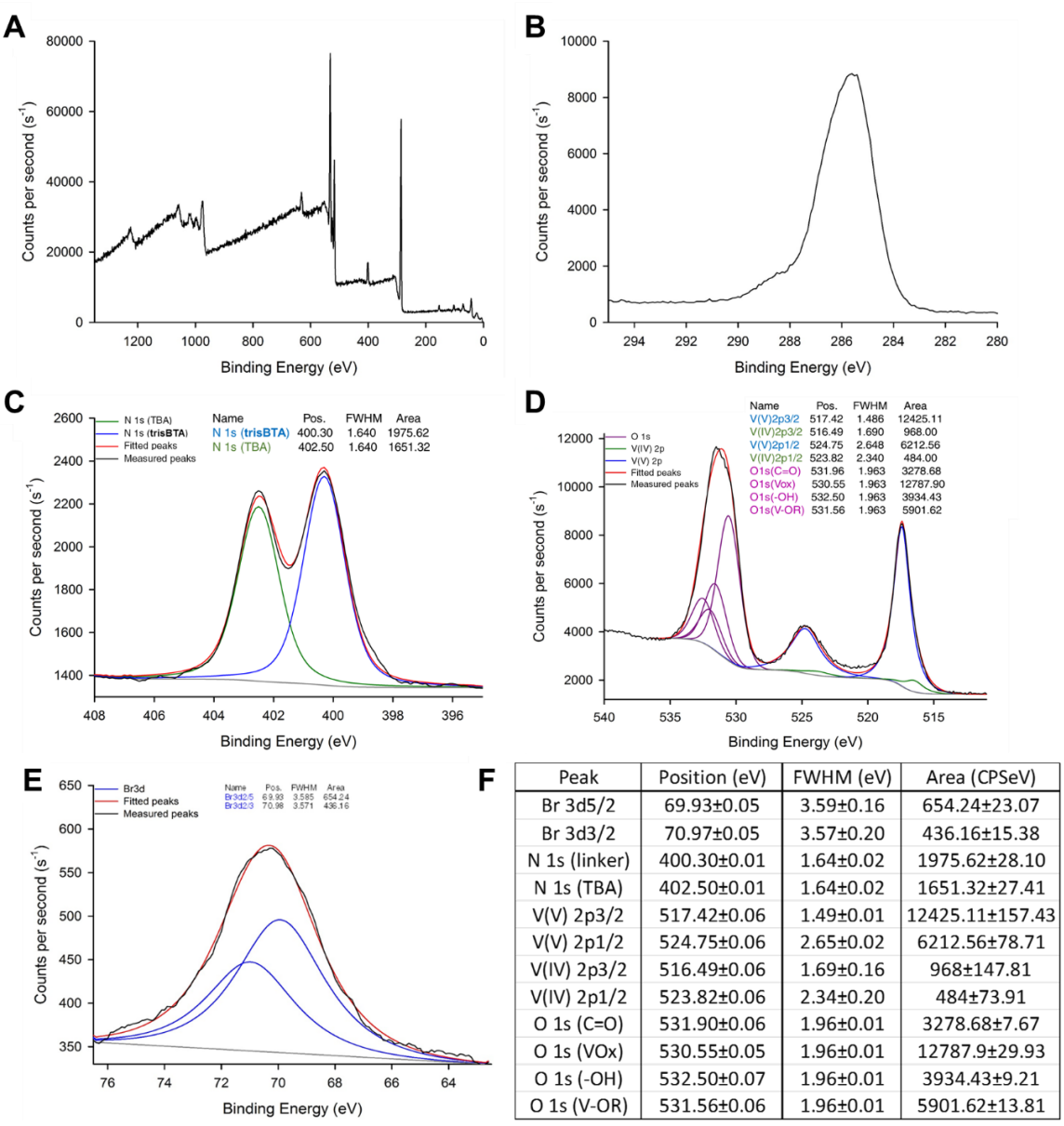

Peak	Position (eV)	FWHM (eV)	Area (CPSeV)
Br 3d5/2	69.93±0.05	3.59±0.16	654.24±23.07
Br 3d3/2	70.97±0.05	3.57±0.20	436.16±15.38
N 1s (linker)	400.30±0.01	1.64±0.02	1975.62±28.10
N 1s (TBA)	402.50±0.01	1.64±0.02	1651.32±27.41
V(V) 2p3/2	517.42±0.06	1.49±0.01	12425.11±157.43
V(V) 2p1/2	524.75±0.06	2.65±0.02	6212.56±78.71
V(IV) 2p3/2	516.49±0.06	1.69±0.16	968±147.81
V(IV) 2p1/2	523.82±0.06	2.34±0.20	484±73.91
O 1s (C=O)	531.90±0.06	1.96±0.01	3278.68±7.67
O 1s (VOx)	530.55±0.05	1.96±0.01	12787.9±29.93
O 1s (-OH)	532.50±0.07	1.96±0.01	3934.43±9.21
O 1s (V-OR)	531.56±0.06	1.96±0.01	5901.62±13.81

Figure 2.11. XPS spectra of **TBA-polyV$_6$**. (**A**) Survey scan, (**B**) high resolution scan of the C1s region, (**C**) high resolution scan of the N1s region with fitted peak deconvolution (**D**) high resolution scan of the V2p and O1s regions with fitted peak deconvolution (**E**) high resolution scan of the Br3d region with fitted peak deconvolution. (**F**) compilation of data from **A**-**E**.

Singly-capped V_6 units are unstable, meaning that each POM is found in its doubly-capped form in which each vanadium nucleus is identical, confirmed by the presence of a single ^{51}V NMR peak. The theoretical limit assuming only monomers of the form linker-POM-linker are present is 1 bound methylene: 2 unbound methylene, whereas a linear polymer with alternating POM and **trisBTA** units reaches a theoretical ratio of 2 bound methylene: 1 unbound methylene. The polymer can therefore not simply be composed of linear strands and must adopt a complex structure. Theoretically, an infinite 2-dimensional polymer of POM units and linker molecules reaches an upper limit of 1.5 POM: 1 **trisBTA**, a monomer would have a ratio of 0.5 POM: 1 **trisBTA**, and an infinitely long linear polymer would achieve a ratio of 1 POM: 1 **trisBTA**. A POM: **trisBTA** ratio higher than 1:1 confirms that there are points where a triply-bound linker is creating a closed loop in the polymer and indicates the presence of roughly 9% closed-loop points in the network. Each closed loop requires two triply-bound linkers, so 18% represents a minimum estimate of the number of triply-bound linkers in the material, (examples of singly-doubly- and triply-bound linkers are shown in Figure 2.1).

Static light scattering measurements on a sample of **TBA-polyV$_6$** dispersed in wet DMF determined the average molecular weight of the material to be 1600 kDa (Figure 2.12), indicating the average polymer is comprised of roughly 1,000 monomer units. However, due to low solubility, this molecular weight determination can only be a rough approximation of the average molecular weight and represents a low estimate.

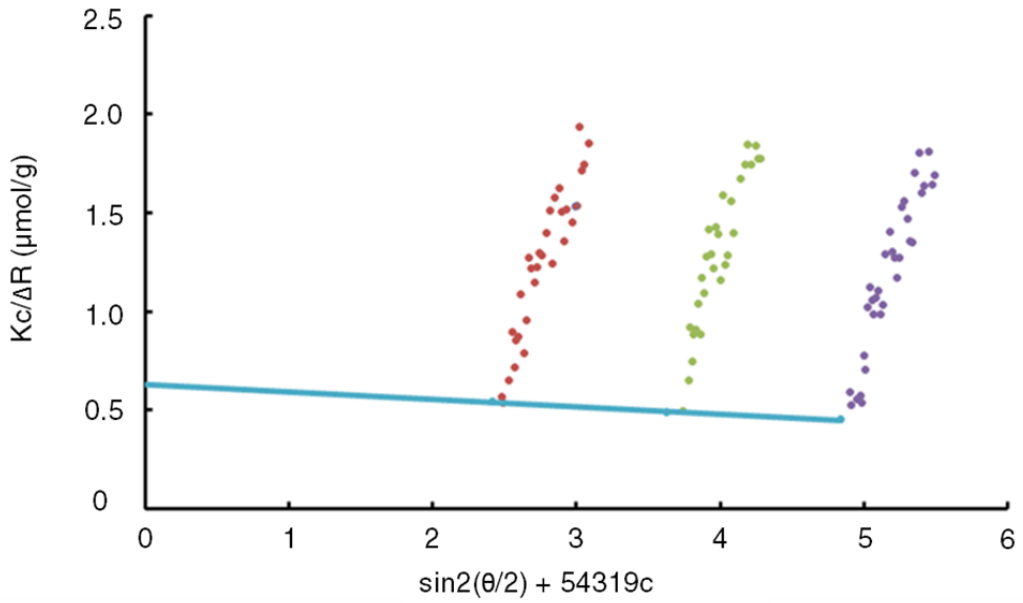

Figure 2.12. Static light scattering of **TBA-polyV$_6$**. Zimm plot of the static light scattering measurements of the solutions of **TBA-polyV$_6$** in DMF/water mixed solvent (85% DMF/15% H_2O). SLS experiments were performed at scattering angles (θ) between 30 and 100°, at 2° intervals. Solutions with concentrations of 0.90, 0.68, and 0.45 mg/mL were used.

By compiling the molecular weight estimate from SLS, the ratio of bound linkers to unbound linkers from solid-state ^{13}C NMR, and elemental ratios obtained by both NMR and XPS we can infer that **TBA-polyV$_6$** is a cross-linked polymer with a complex non-linear structure. These cross-linked fiber structures can be seen in electron microscopy images of the material (Figure 2.13). The extensively cross-linked nature of the polymer results in the material possessing a relatively high BET surface area of 430 m^2/g.

A

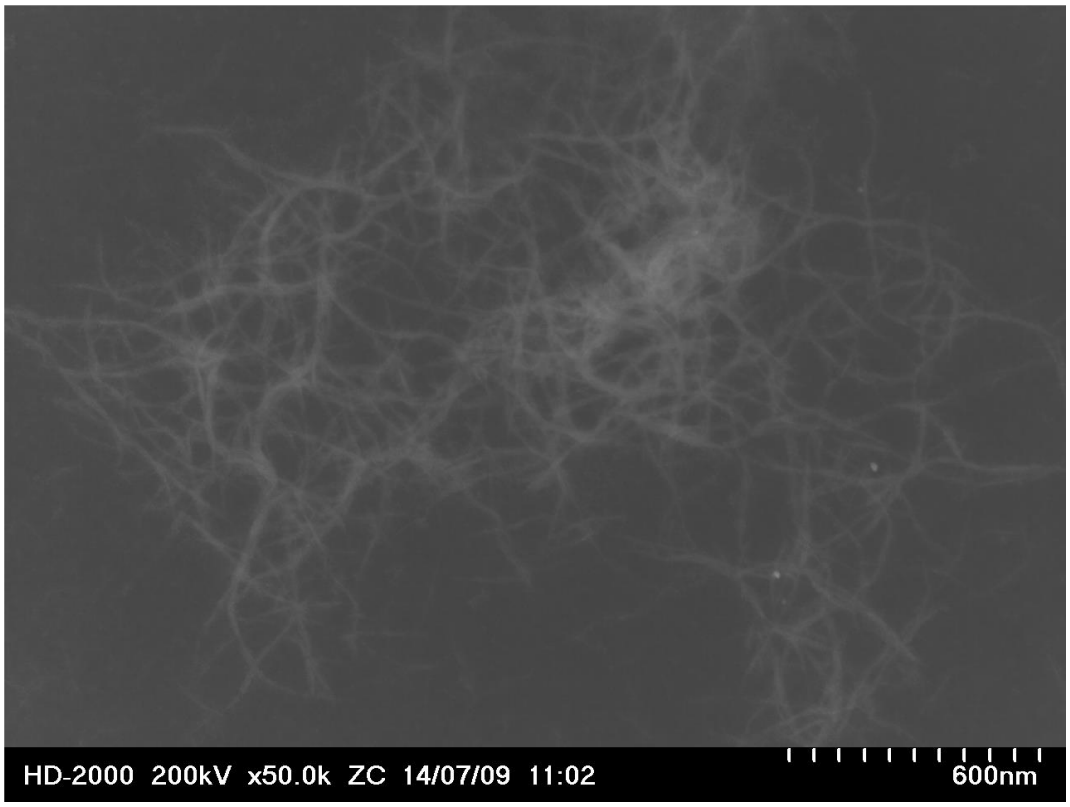
HD-2000 200kV x50.0k ZC 14/07/09 11:02
600nm

B

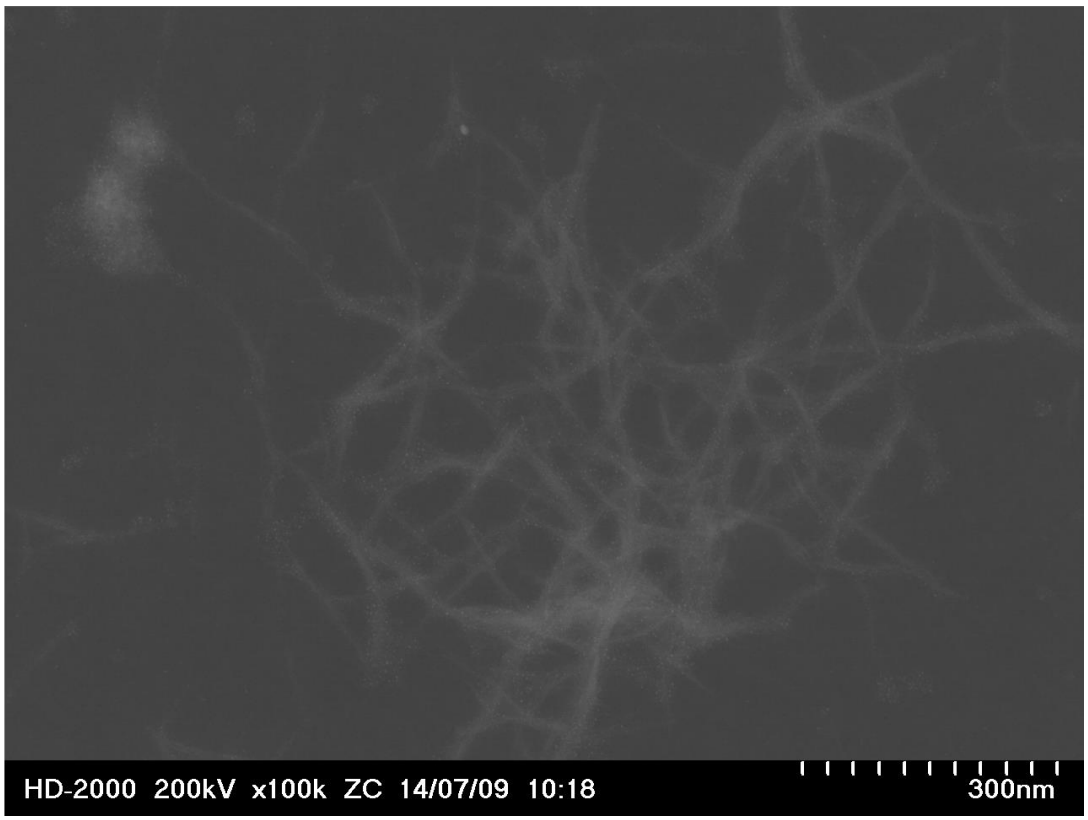
HD-2000 200kV x100k ZC 14/07/09 10:18
300nm

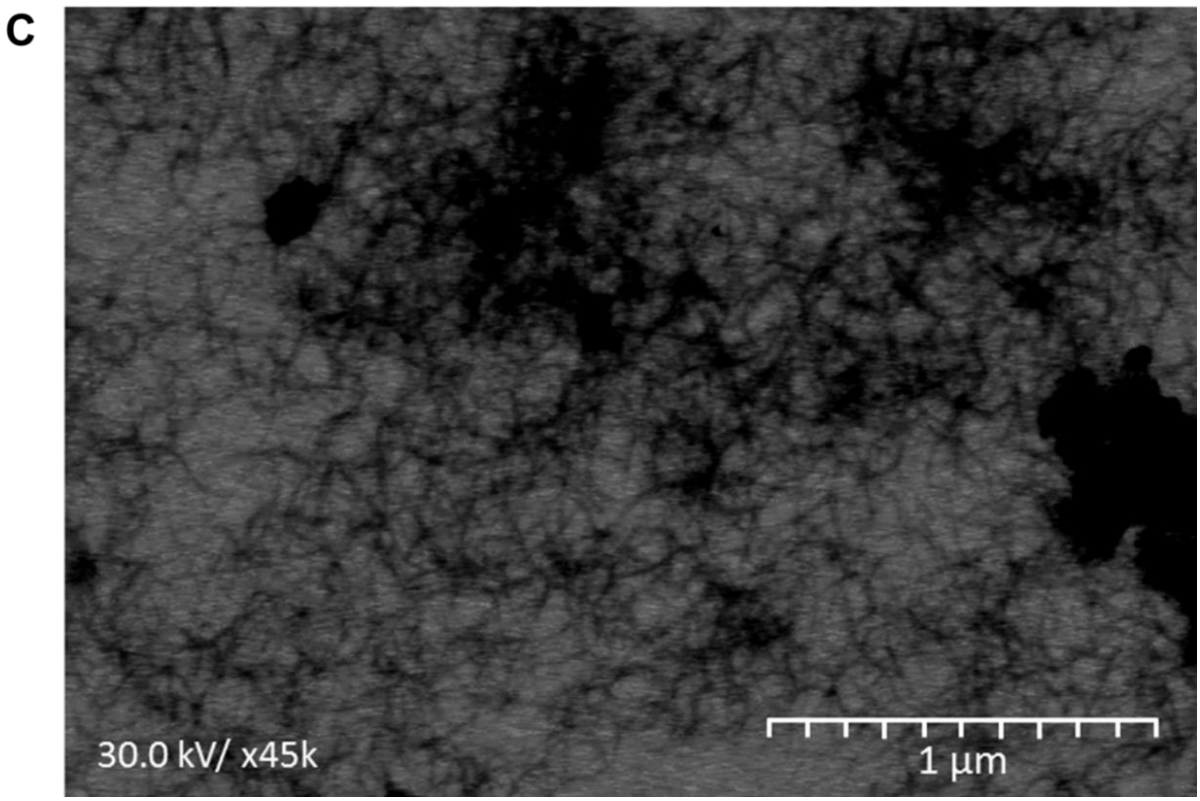

Figure 2.13. Electron microscopy of **TBA-polyV$_6$.** Images taken after swelling in DMSO and drying under vacuum. Contrast enhanced using Microsoft Word software. (**a, b**) STEM images in Z-contrast mode of **TBA-polyV$_6$**. (**c**) TEM image of **TBA-polyV$_6$**.

2.3.2 Gelation Capability

TBA-polyV$_6$ exhibits remarkable physical properties in the presence of polar aprotic liquids, entrapping them upon contact and forming gels within seconds (Figure 2.14).

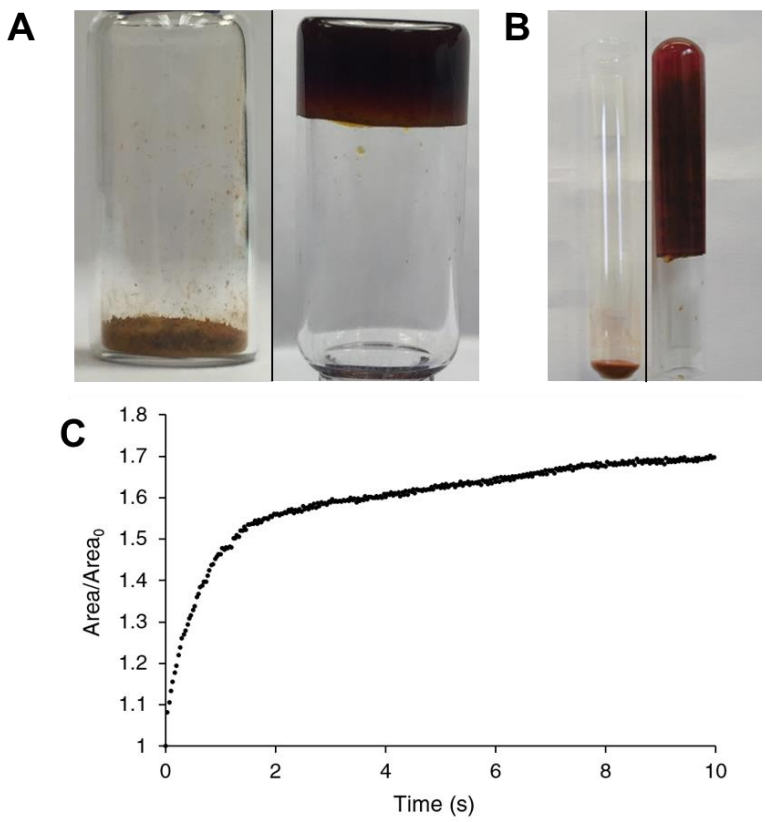

Figure 2.14. Swelling behavior of **TBA-polyV$_6$**. (**A**) Swelling of **TBA-polyV$_6$** (left) in the presence of dimethyl methyl phosphonate (DMMP) (right). (**B**) Swelling of **TBA-polyV$_6$** (left) in the presence of DMF (right). (**C**) Analysis of swelling rate using particle tracking after exposure to DMF.

The primary gelation mechanism in 1,3,5-benzenetricarboxamide-based gels is the formation of hydrogen-bonding networks.[53, 67] ATR FT-IR studies of **TBA-polyV$_6$** reveal a red shift in the amide 1 band of DMF (which primarily consists of the amide C=O stretch) from 1661 cm^{-1} to 1652 cm^{-1} upon addition of **TBA-polyV$_6$**, indicative of hydrogen bonding interactions between the gelator and the carbonyl oxygen of DMF (Figure 2.15). The occurrence of gelation in polar aprotic solvents and contraction in protic solvents suggests that when external hydrogen bond donors are present (such as with H_2O), the hydrogen bonding networks between **TBA-polyV$_6$** and DMF are disrupted and result in contraction of the gel. These gels remain stable to inversion indefinitely after swelling and can be returned to the contracted solid form though addition of a nonpolar

solvent such as toluene or diethyl ether, demonstrating both rapid and reversible organogel-forming activity. The material also retains its gelation capability even after multiple swelling/contraction cycles.

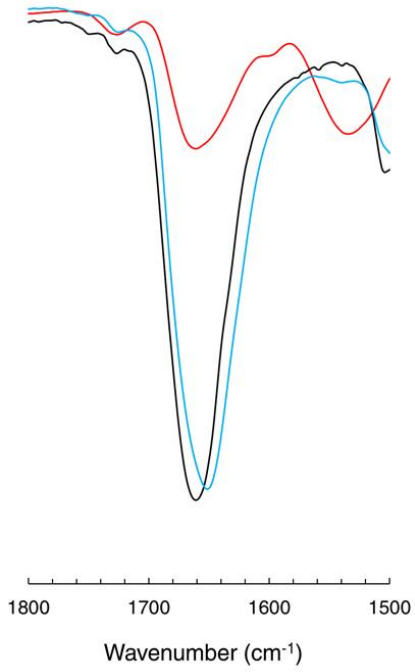

Figure 2.15. **Hydrogen-bond-induced carbonyl peak shifts**. ATR FT-IR spectra of DMF with varying amounts of **TBA-polyV$_6$** added. The amide 1 band, consisting of the amide C=O stretch, is shown. The peak is observed for pure DMF at 1661 cm^{-1} (●). When 8 wt% gelator is added, a red-shifted amide peak is observed to 1652 cm^{-1} (●). The spectrum of **TBA-polyV$_6$** (●) alone (no solvent) is shown to demonstrate that an increase in the amount of gelator alone is not the cause of the observed red shift in the DMF amide peak.

Several reports suggest that OP agents can interact with hydrogen-bond donors through the phosphoryl oxygen.[53, 68-69] Interaction with the multiply-hydrogen-bonding trisBTA units, as well as pore-filling by the solvent in the cross-linked polymer are likely to contribute to the gel formation behavior of **TBA-polyV$_6$**. Significantly, **TBA-polyV$_6$** is capable of forming gels when exposed to OP agent analogues. Addition of the G-series nerve agent analogue DMMP results in a substantial index of swellability (Q) value of 10 mL g^{-1} (Figure 2.14 and Table 2-2). Indeed,

studies using highly-crosslinked polymers have demonstrated correlations between swelling capability in polar organic liquids such as DMF and CWAs such as HD and OPs.[50]

Table 2-2. Swelling parameters for **TBA-polyV$_6$** and **Li-polyV$_6$**.

	Swellability Q (mL g^{-1})		
	DMSO	DMF	DMMP
TBA-polyV$_6$	15.6 ± 0.7	13.0 ± 1.0	9.6 ± 1.7
Li-polyV$_6$	19.0 ± 0.1	15.0 ± 1.1	8.8 ± 0.5

It is notable that this gelation behavior occurs rapidly and spontaneously, as this allows for the material to entrap OP agents directly upon contact. This rapid gelation behavior was visualized under a microscope, and image analysis was used to obtain a qualitative measure of the swelling kinetics (Figure 2.14). Comparing the swelling capability of **TBA-polyV$_6$** to other absorbent materials reveals its high capacity for organic liquid entrapment (Figure 2.16).

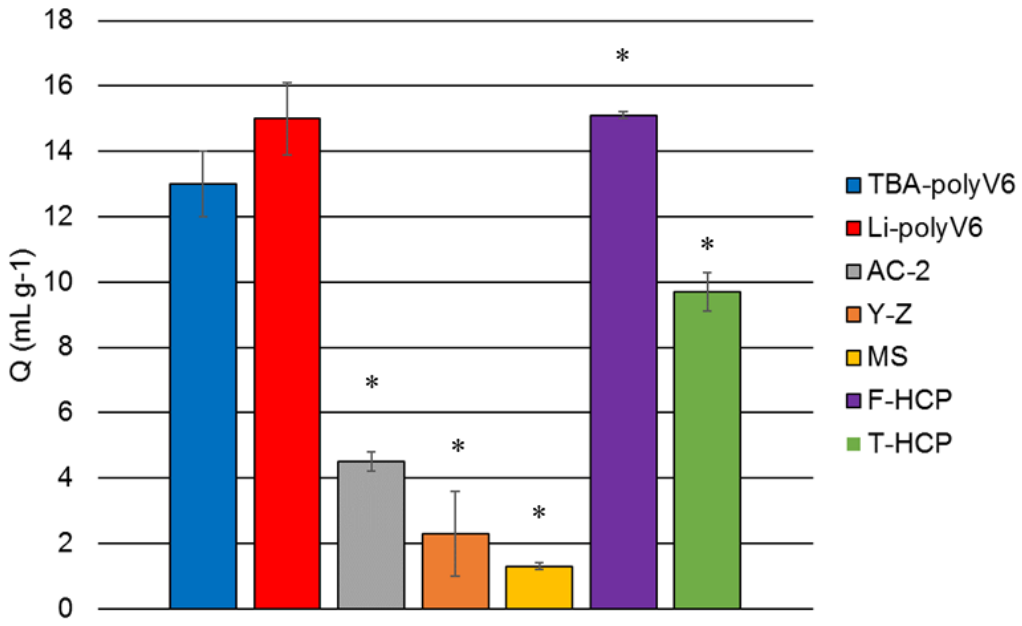

Figure 2.16. Comparison of index of swellability (Q) between **TBA-polyV$_6$**, **Li-polyV$_6$** and other adorbents. Index of swellability for activated charcoal 100-4000 mesh (AC-2), molecular sieves 3Å (MS), y-zeolite (Y-Z), fluorobenzene-derived highly crosslinked polymer (F-HCP), and toluene-derived highly crosslinked polymer (T-HCP). In each case, the gel was swollen for 24 hours prior to analysis. Data indicated with [*] is from Wilson *et. al*. using similair procedures to determine Q.[50]

A key design of **TBA-polyV$_6$** as a smart multifunctional material is its potential to be readily tuned for desired applications. It is straightforward to exchange the TBA^+ counter cations for a variety of alternate counter cations, such as Li^+. The exchange of TBA^+ for Li^+ was accomplished by simple elution of a solution containing $LiBF_4$ through a column containing **TBA-polyV$_6$**. Both FT-IR and CP-MAS ^{13}C NMR display the complete absence of TBA^+ peaks in the resulting material, **Li-polyV$_6$**, and demonstrate that the polymer remains intact after the exchange (Figures 2.17 and 2.18).

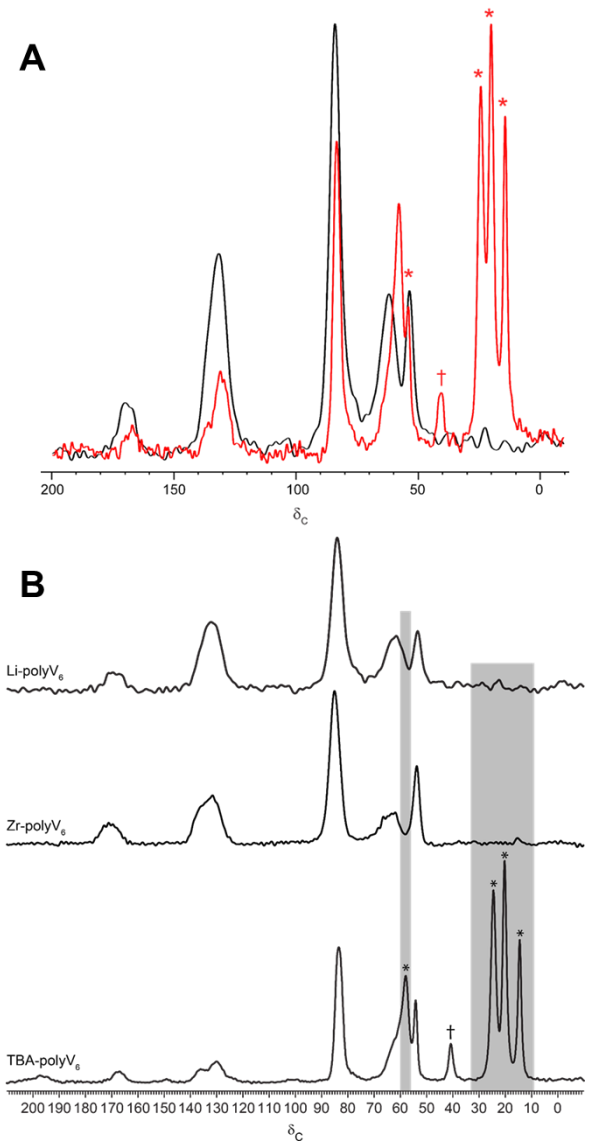

Figure 2.17. ^{13}C (75.5 MHz) CP-MAS spectra of **TBA-, Li-, and Zr-polyV$_6$**. (**A**) **TBA- (●) and Li- (●) polyV$_6$** spectra are shown. TBA$^+$ cation (*), and DMSO (†) peaks are indicated. The increased resolution between the triol carbons at 54 and 62 ppm is consistent with distinct H-bonding environments in the **TBA-** and **Li-polyV$_6$** samples. TBA$^+$ counter cations are not observed in **Li-polyV$_6$**. (**b**) ^{13}C (75.5 MHz) CP-MAS spectra of **TBA-**, **Li-**, and **Zr-polyV$_6$**. TBA$^+$ cation (*), and DMSO (†) peaks are indicated.

FT-IR and ^{51}V NMR of isolated **Li-polyV$_6$** confirm that the hexavanadate core is also intact after the exchange. Significantly, **Li-polyV$_6$** is a hydrophilic version of **TBA-polyV$_6$**, exhibiting dramatically different physical characteristics such as hydrogelation capability (Table 2-2). Employing the same method allowed for the synthesis of a large number of derivatives with

varying counter cations, including tetrahexylammonium, tetrapropylammonium, ammonium, potassium, cerium, copper, europium, lanthanum, silver, and zirconium. Of these, the zirconium-exchanged polymer **Zr-polyV$_6$** has been used for further investigations and is discussed below.

.

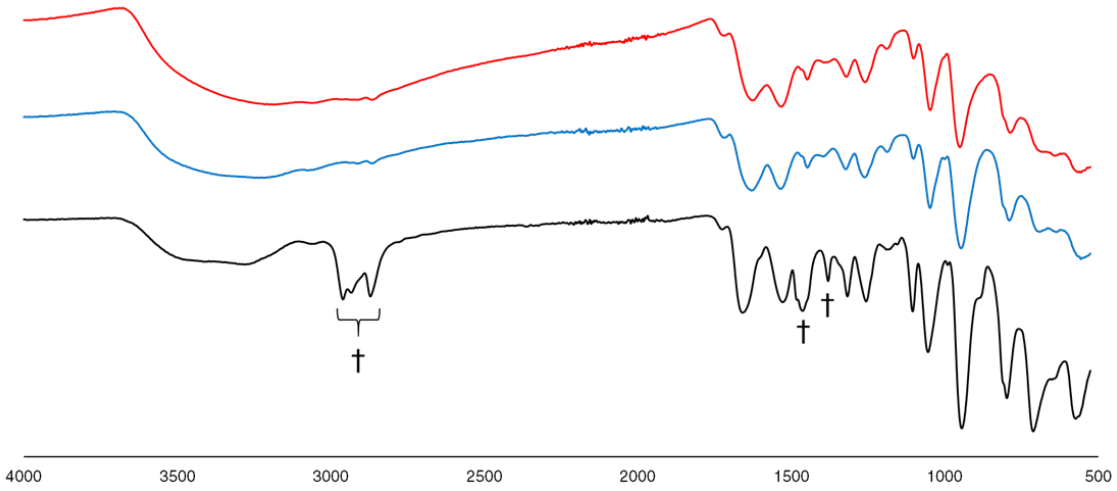

Figure 2.18. ATR-FTIR spectra of **Li-polyV$_6$** and **Zr-polyV$_6$** polymers. **TBA-polyV$_6$** (●), **Zr-polyV$_6$** (●) and **Li-polyV$_6$** (●). Tetrabutylammonium peaks (†) are present in the **TBA-polyV$_6$** sample at 2930 cm^{-1}, 2950 cm^{-1}, 2870 cm^{-1}, 1490 cm^{-1} and 1390 cm^{-1} but are not present in the cation-exchanged polymers.

The ability to ability to tailor this new class of materials to obtain favorable physical properties and exhibit desired swelling based on judicious counter cation choice demonstrates the utility of this new class of polymers.

2.3.3 Catalytic Activity

As mentioned previously, hexavanadate POMs are known to be active towards the oxidation of sulfides. [22-23] To demonstrate the applicability of **TBA-polyV$_6$** for air-based oxidative removal reactions under mild conditions, we conducted studies on the catalytic oxidation of propane thiol (PrSH) to dipropyl disulfide (PrSSPr). This representative odorant is fully oxidized to the non-

odorous disulfide, using only oxygen to reoxidize the reduced POM units (130 turnovers in ~6 days) (Figure 2.19).

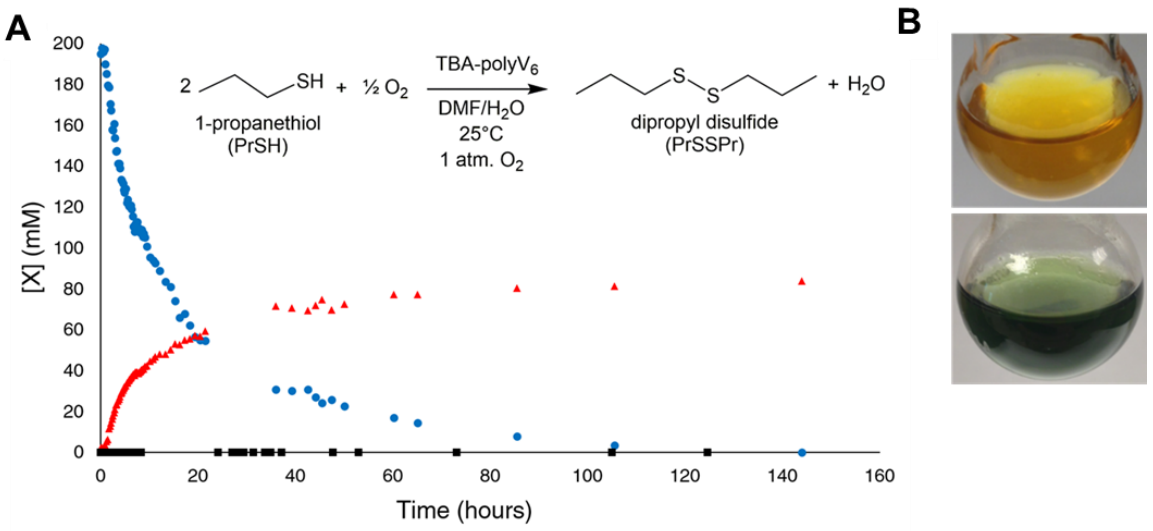

Figure 2.19. Aerobic oxidation of propane thiol. (**A**) Oxidation of propane thiol (●) to dipropyl disulfide (▲) The mole ratio is 127 PrSH per V_6. A control (■) was run with the omission of **TBA-polyV$_6$**. (**B**) **TBA-polyV$_6$** in DMF before (above) and after (below) addition of PrSH. Reactions monitored by gas chromatography.

TBA-polyV$_6$ is red in its powder state and reddish-orange when dispersed in solvent (λ_{max} = 388 nm), indicative of a fully oxidized $[V^{V}_{6}O_{13}(OR)_6)]^{2-}$ core (R = **tris(TRIS)** linkers). Upon reduction of the POM, the material becomes dark green as the peak at 388 nm decreases and a broad peak between 600 and 900 nm increases, providing a colorimetric detection capability (Figure 2.19 and Figure 2.20).

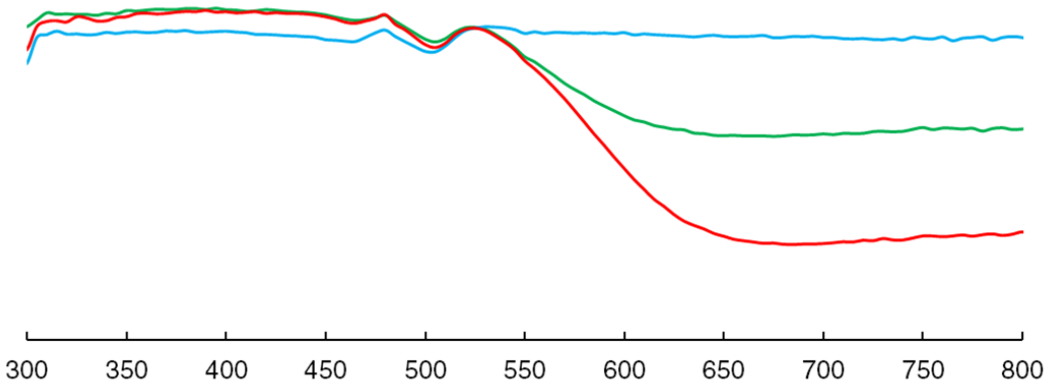

Figure 2.20. Diffuse reflectance UV/Vis spectra of **TBA-polyV$_6$**. Sample of **TBA-polyV$_6$** before (●) and after (●) reduction by excess ascorbic acid, resulting in a very broad peak arising from IVCT bands in the region from 600-1000 nm. Upon addition of PrSH (●), reduction of the V_6 center results in a green color, consistent with reduction of V_6 sites within the material.

The persistent observation of a green reduced hexavanadate species suggests that reoxidation of **TBA-polyV$_6$** by O_2 is rate-limiting under these conditions. Titration UV/vis studies indicate that the green color is associated with a two-electron reduced hexavanadate, whereas the four-electron reduced cluster is blue in color (Figure 2.21), in accordance with previous reports.[64] This dramatic and responsive color change detection capability is another attribute of these polymers that is advantageous for protection and decontamination technologies.

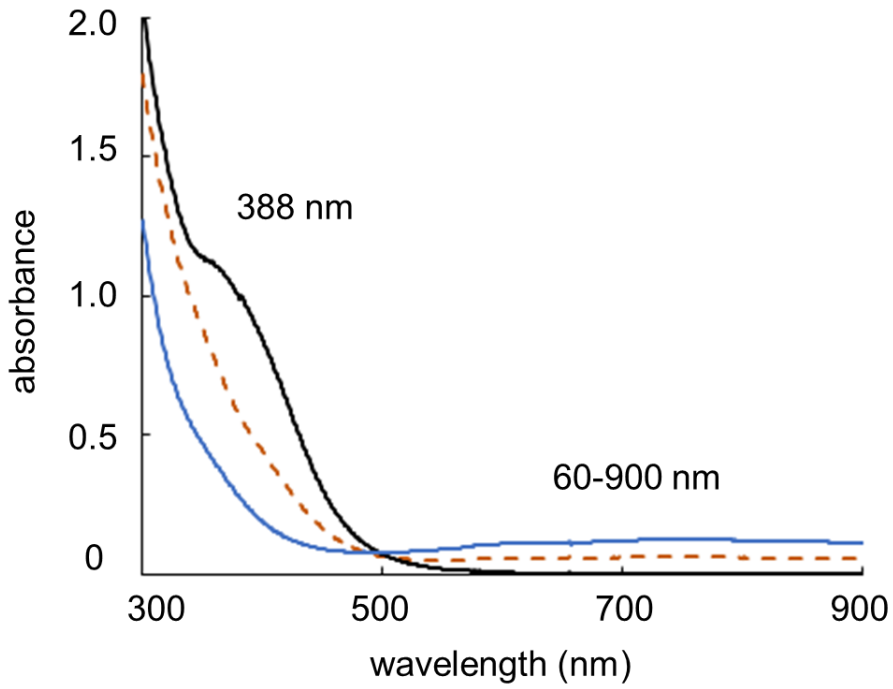

Figure 2.21. UV/Vis spectra of **NH_2V_6** upon reduction by $SnCl_2$. Black line represents fully-oxidized starting material. Dotted brown line is after the addition of 1 equivalent of the reductant $SnCl_2$, and the blue line is after addition of two equivalents of $SnCl_2$.

More significantly, **TBA-polyV$_6$** catalyzes oxidation of the HD simulant, CEES, by the mild and environmentally-friendly oxidant hydrogen peroxide. CEES is completely and rapidly oxidized in the presence of **TBA-polyV$_6$** and H_2O_2 (Figure 2.22), showing its promise as an effective catalyst for the removal of HD under mild conditions.

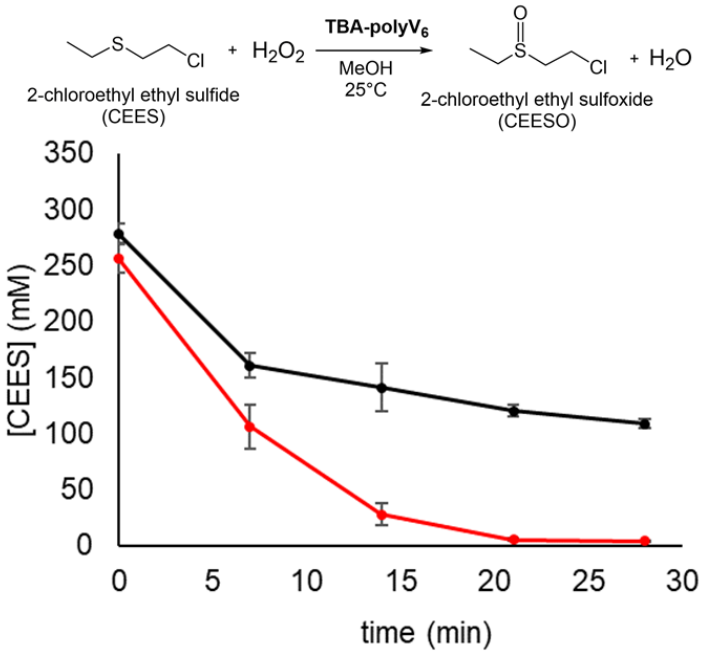

Figure 2.22. Oxidation of CEES by H_2O_2 catalyzed by **TBA-polyV$_6$**. The mole ratio of the catalyzed reaction (●) was 1 V_6: 120 CEES: 120 H_2O_2. The uncatalyzed control reaction (●) was run with the omission of **TBA-polyV$_6$**. Reactions were repeated in triplicate and error bars are reported.

Additionally, this reaction selectively forms the less toxic 2-chloroethyl ethyl sulfoxide (CEESO) without overoxidizing to the harmful 2-chloroethyl ethyl sulfone ($CEESO_2$) product, as confirmed by ^{1}H NMR analysis before and after the reactions (Figure 2.23).

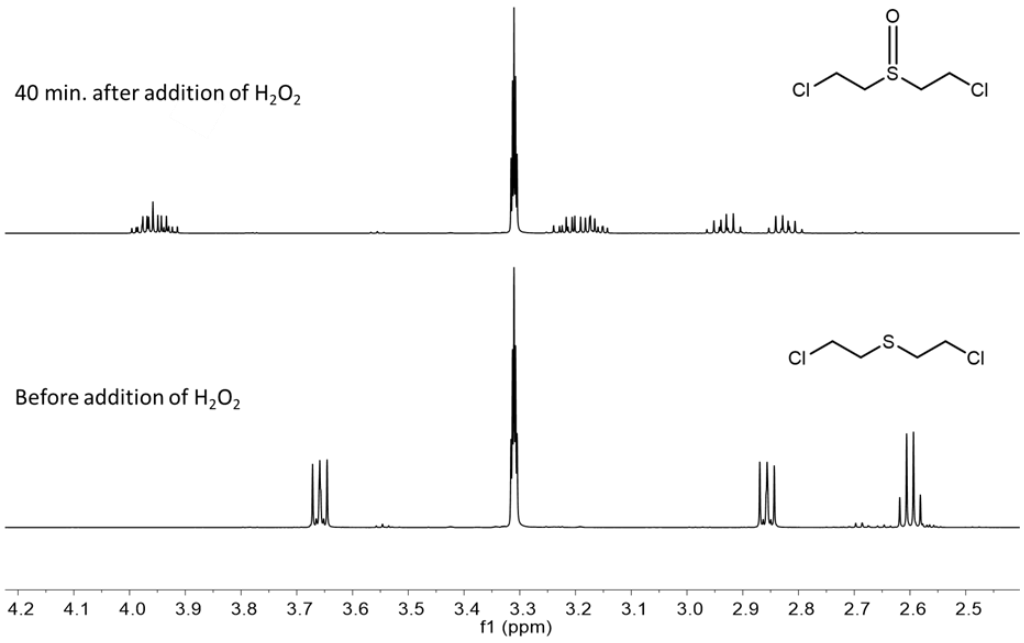

Figure 2.23. ^{1}H NMR used to quantify the CEES-derived products. ^{1}H NMR of reaction mixture before (below) and after (above) completion of the catalytic reaction, demonstrating near-quantitative conversion of CEES to CEESO without the formation of $CEESO_2$.

Both **Zr-polyV$_6$** and **Li-polyV$_6$** also exhibit catalytic sulfoxidation activity (Figure 2.24) compared to related heterogeneous sulfoxidation catalysts.[70-71] Through these two exemplary oxidation reactions, we demonstrate the applicability of the **TBA-polyV$_6$** polymer for catalytic oxidation of toxic or odorant molecules under mild conditions.

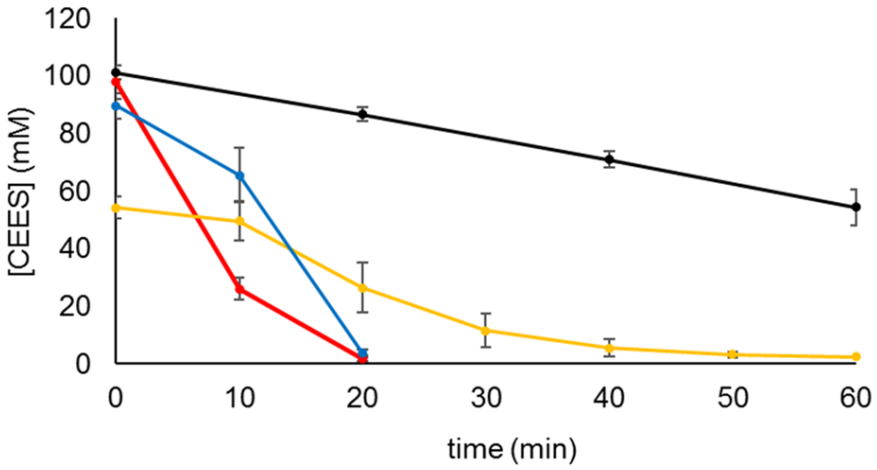

Figure 2.24. CEES sulfoxidation by H_2O_2 catalyzed by **polyBTAV$_6$** polymers. The mole ratio of the catalyzed reaction was 1 V_6: 40 CEES: 40 H_2O_2 in all cases. The uncatalyzed control reaction (●) was run with the omission of **TBA-polyV$_6$**. Reactions were repeated in triplicate and error bars are reported. **TBA-polyV$_6$** (●), **Li-polyV$_6$** (●), and **Zr-polyV$_6$** (●) reactions are shown. Interestingly, the reaction using **Zr-polyV$_6$** as the catalyst initially shows a very rapid oxidation of ~50% of the CEES, followed by slower kinetics to achieve complete conversion.

Both polyoxometalate-catalyzed hydrolysis of phosphoester bonds and hydrogen-bond-donor-catalyzed hydrolysis of OP agents have been demonstrated in recent studies.[53, 68, 72] We were therefore encouraged to examine the effectiveness of these polymers towards hydrolysis of OP analogues. **TBA-polyV$_6$** catalyzes the hydrolytic breakdown of the OP nerve agent analogue diethyl cyanophosphonate (DECP) to the nontoxic diethyl phosphate (Figure 2.25), likely through the formation of multiple hydrogen-bonding interactions between the polymer and DECP.[53]

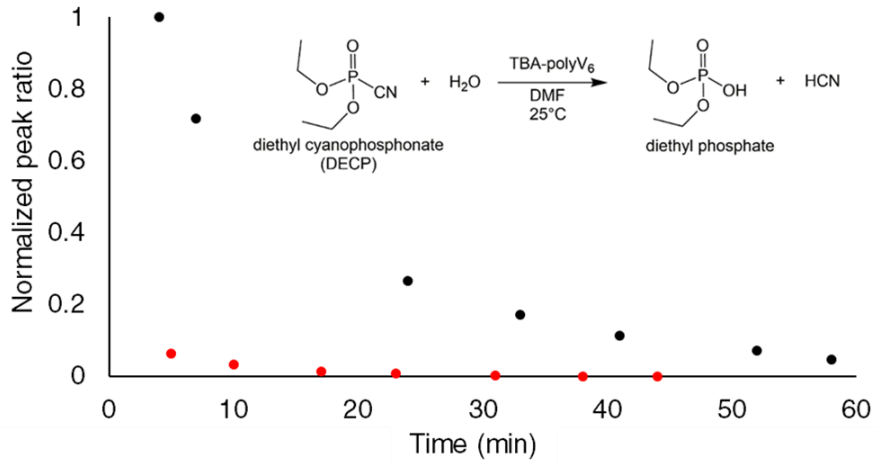

Figure 2.25. Hydrolysis of DECP catalyzed by **TBA-polyV$_6$.** Hydrolysis of diethyl cyanophosphonate (DECP) catalyzed by **TBA-polyV$_6$** in DMF. The DECP: **TBA-polyV$_6$** molar ratio was 20:1 based on V_6 units. Reactions were monitored by ^{31}P NMR. The control reaction (●) was run using the same conditions as the catalyzed reaction (●) but with the omission of **TBA-polyV$_6$**.

Despite the effectiveness of **TBA-polyV$_6$** in catalyzing hydrolysis of DECP, it is less effective against more realistic and challenging OP agent analogues. Zr-based materials have received a great deal of attention for their high activities towards hydrolysis of OP nerve agents, particularly in recent work using Zr-based MOFs.[73-74] Accordingly, the Zr-substituted **Zr-polyV$_6$** shows significant activity for catalyzing the hydrolysis of dimethyl *p*-nitrophenylphosphate (DMNP) and achieves full conversion to the hydrolysis products (Figure 2.26).

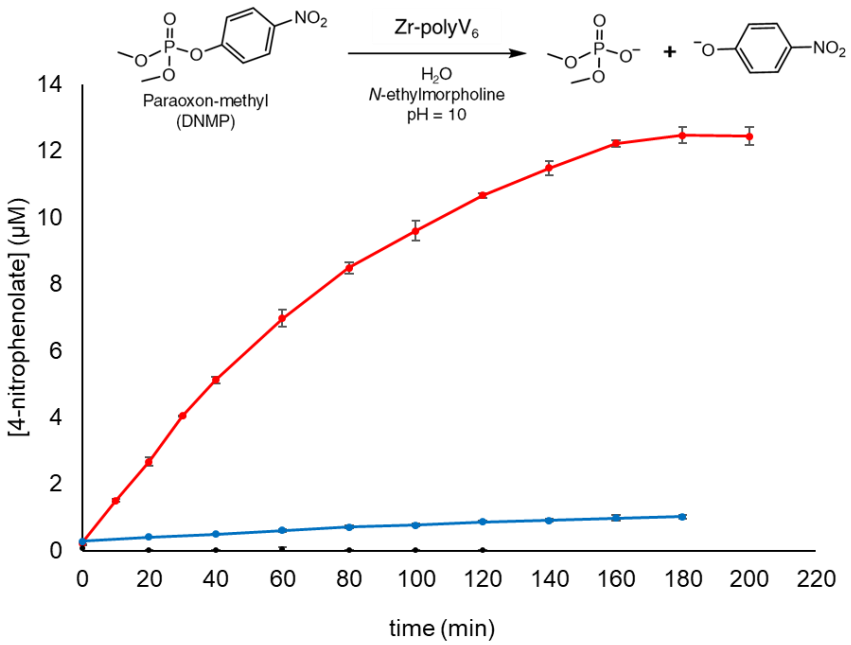

Figure 2.26. Hydrolysis of DMNP catalyzed by **Zr-polyV$_6$** (●) in aqueous 0.45M *N*-ethylmorpholine at pH 10.00, measured through formation of 4-nitrophenolate anion. The DMNP: **Zr-polyV$_6$** ratio was 10 : 1 based on Zr_4 units. Reactions run without catalyst (●) and **TBA-polyV$_6$** (●) are shown. Reactions were run in triplicate and error bars are reported.

To ensure that the reaction catalyzed by **Zr-BTAV$_6$** was truly heterogeneous, a sample of **Zr-BTAV$_6$** was stirred in NEM buffer at pH 10.00 for two hours followed by filtration using a 2 μm syringe filter to remove the solid material. The supernatant was found to have negligible catalytic activity, confirming that **Zr-BTAV$_6$** catalyzes the hydrolysis as a solid material (Figure 2.27).

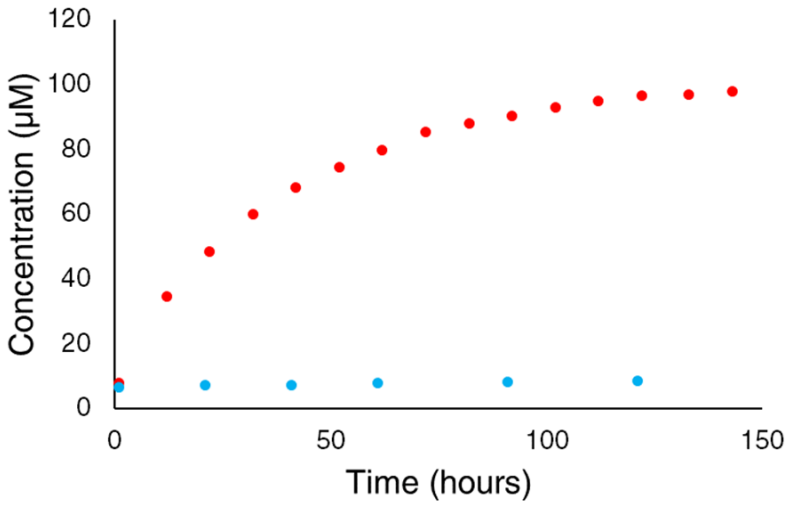

Figure 2.27. Filtration studies on hydrolysis of DMNP catalyzed by **Zr-polyV$_6$**. **Zr-polyV$_6$** (5.0 mg, 2.45 μmol) and 4 μL (25 μmol) DMNP were added to aqueous 0.45M *N*-ethylmorpholine (NEM) at pH 10 (●). Reactions were monitored by UV/Vis spectroscopy, detecting the formation of the 4-nitrophenolate hydrolysis product. To ensure a heterogeneous reaction, 5.0 mg of **Zr-polyV$_6$** was stirred in 0.45M NEM buffer at pH = 10.00 for two hours, followed by filtration using 0.2 μm syringe filters. The supernatant was collected and 4 μL DMNP were added to initiate the reaction, which exhibited negligible activity (●).

2.4 Conclusions

The studies outlined in this chapter have reported the synthesis and characterization of the multifunctional polymer **TBA-polyV$_6$**, identifying that it is composed of alternating hexavanadate POM and **trisBTA** units. The polymer is, to our knowledge, the first example of a material which forms gels upon contact with CWA analogues while simultaneously possessing catalytic oxidation and hydrolysis functions. The catalytic redox processes proceed under mild conditions for the representative odorant propane thiol and the HD analogue CEES. The chemical and physical properties of **TBA-polyV$_6$** can be readily tuned by judicious choice of counter cation, producing the two exemplary polymers **Zr-polyV$_6$** and **Li-polyV$_6$**. **Li-polyV$_6$** exhibits altered gelation properties, while **Zr-polyV$_6$** has increased ability to hydrolyze OP analogues. These POM-based polymers represent the first examples of a new type of multifunctional soft material with several

potential applications, including responsive catalytic materials for sequestration and decontamination of deleterious compounds. The ease of tunability of the polymer allows for many new related materials to be synthesized by altering the linker, POM, and counter cation.

2.5 References

1. Zeng, H. Toward functional supramolecular poly(polyoxometalate)s and materials. Emory University, 2004.

2. Neiwert, W. Polyoxometalates as nanoscale building blocks for the formation of fundamentally new materials. Emory University, 2004.

3. Hillesheim, D. Developing Oxidation Catalysts, Understanding Mechanisms of Polyoxometalate-based Oxidations, and Systems for Color-Change Detection Technology. Emory University, 2009.

4. Sullivan, K. P.; Neiwert, W. A.; Zeng, H.; Mehta, A. K.; Yin, Q.; Hillesheim, D. A.; Vivek, S.; Yin, P.; Collins-Wildman, D. L.; Weeks, E. R.; Liu, T.; Hill, C. L., *Chemical Communications* **2017,** 53 (83), 11480-11483.

5. Borrás-Almenar, J. J.; Coronado, E.; Müller, A.; Pope, M., *Polyoxometalate Molecular Science*. 1 ed.; Springer Netherlands: 2003; Vol. 98, p 475.

6. Dolbecq, A.; Dumas, E.; Mayer, C. R.; Mialane, P., *Chemical Reviews* **2010,** 110 (10), 6009-6048.

7. Judeinstein, P.; Sanchez, C., *Journal of Materials Chemistry* **1996,** 6 (4), 511-525.

8. Miras, H. N.; Yan, J.; Long, D.-L.; Cronin, L., *Chemical Society Reviews* **2012,** 41 (22), 7403-7430.

9. Wu, H.; Yang, H.-K.; Wang, W., *New Journal of Chemistry* **2016,** 40 (2), 886-897.

10. Carraro, M.; Gross, S., *Materials* **2014,** 7 (5), 3956.

11. Walsh, J. J.; Bond, A. M.; Forster, R. J.; Keyes, T. E., *Coordination Chemistry Reviews* **2016,** 306, 217-234.

12. Blazevic, A.; Rompel, A., *Coordination Chemistry Reviews* **2016,** 307, 42-64.

13. Xu, L.; Lu, M.; Xu, B.; Wei, Y.; Peng, Z.; Powell, D. R., *Angewandte Chemie International Edition* **2002,** 41 (21), 4129-4132.

14. Wang, R.; Li, Y.; Shetye, K.; Dutta, T.; Jin, L.; Li, S.; Peng, Z., *European Journal of Inorganic Chemistry* **2015,** 2015 (4), 656-663.

15. Haso, F.; Wang, R.; He, J.; Luo, J.; Eghtesadi, S. A.; Peng, Z.; Liu, T., *New Journal of Chemistry* **2016,** 40 (2), 910-913.

16. Kang, J.; Xu, B.; Peng, Z.; Zhu, X.; Wei, Y.; Powell, D. R., *Angewandte Chemie International Edition* **2005,** 44 (42), 6902-6905.

17. Tong, U.; Chen, W.; Ritchie, C.; Wang, X.; Song, Y.-F., *Chemistry – A European Journal* **2014,** 20 (6), 1500-1504.

18. Yang, H.-K.; Cheng, Y.-X.; Su, M.-M.; Xiao, Y.; Hu, M.-B.; Wang, W.; Wang, Q., *Bioorganic & Medicinal Chemistry Letters* **2013,** 23 (5), 1462-1466.

19. Yvon, C.; Surman, A. J.; Hutin, M.; Alex, J.; Smith, B. O.; Long, D.-L.; Cronin, L., *Angewandte Chemie International Edition* **2014,** 53 (13), 3336-3341.

20. Feng, X.; Zhou, W.; Li, Y.; Ke, H.; Tang, J.; Clérac, R.; Wang, Y.; Su, Z.; Wang, E., *Inorganic Chemistry* **2012,** 51 (5), 2722-2724.

21. Long, D.-L.; Tsunashima, R.; Cronin, L., *Angewandte Chemie International Edition* **2010,** 49 (10), 1736-1758.

22. Yin, P.; Wang, J.; Xiao, Z.; Wu, P.; Wei, Y.; Liu, T., *Chemistry – A European Journal* **2012,** 18 (30), 9174-9178.

23. Han, J. W.; Hill, C. L., *Journal of the American Chemical Society* **2007,** 129 (49), 15094-15095.

24. Proust, A.; Matt, B.; Villanneau, R.; Guillemot, G.; Gouzerh, P.; Izzet, G., *Chemical Society Reviews* **2012,** 41 (22), 7605-7622.

25. Zhang, B.; Yin, P.; Haso, F.; Hu, L.; Liu, T., *Journal of Cluster Science* **2014,** 25 (3), 695-710.

26. Linnenberg, O.; Kondinski, A.; Monakhov, K. 2017.

27. Jung, J. H.; Lee, J. H.; Silverman, J. R.; John, G., *Chemical Society Reviews* **2013,** 42 (3), 924-936.

28. Nicole, L.; Laberty-Robert, C.; Rozes, L.; Sanchez, C., *Nanoscale* **2014,** 6 (12), 6267-6292.

29. Zhang, K. Y.; Liu, S.; Zhao, Q.; Huang, W., *Coordination Chemistry Reviews* **2016,** 319, 180-195.

30. Yu, G. C.; Yan, X. Z.; Han, C. Y.; Huang, F. H., *Chem Soc Rev* **2013,** 42 (16), 6697-6722.

31. Suzuki, M.; Hanabusa, K., *Chemical Society Reviews* **2010,** 39 (2), 455-463.

32. Terech, P.; Weiss, R. G., *Chem Rev* **1997,** 97 (8), 3133-3159.

33. Buerkle, L. E.; Rowan, S. J., *Chem Soc Rev* **2012,** 41 (18), 6089-6102.

34. Shapiro, Y. E., *Progress in Polymer Science* **2011,** 36 (9), 1184-1253.

35. Yu, G.; Yan, X.; Han, C.; Huang, F., *Chemical Society Reviews* **2013,** 42 (16), 6697-6722.

36. Lan, Y.; Corradini, M. G.; Weiss, R. G.; Raghavan, S. R.; Rogers, M. A., *Chemical Society Reviews* **2015,** 44 (17), 6035-6058.

37. de Loos, M.; van Esch, J. H.; Kellogg, R. M.; Feringa, B. L., *Tetrahedron* **2007,** 63 (31), 7285-7301.

38. Du, X.; Zhou, J.; Shi, J.; Xu, B., *Chemical Reviews* **2015,** 115 (24), 13165-13307.

39. Ishioka, Y.; Minakuchi, N.; Mizuhata, M.; Maruyama, T., *Soft Matter* **2013**.

40. Lightfoot, M. P.; Mair, F. S.; Pritchard, R. G.; Warren, J. E., *Chemical Communications* **1999,** (19), 1945-1946.

41. He, P.; Xu, B.; Liu, H.; He, S.; Saleem, F.; Wang, X., *Scientific Reports* **2013,** 3, 1833.

42. He, Z.; Wang, H.; Wang, Y.; Wu, Y.; Li, H.; Bi, L.; Wu, L., *Soft Matter* **2012,** 8 (12), 3315-3321.

43. Liu, B.; Yang, J.; Yang, M.; Wang, Y.; Xia, N.; Zhang, Z.; Zheng, P.; Wang, W.; Lieberwirth, I.; Kubel, C., *Soft Matter* **2011,** 7 (6), 2317-2320.

44. Stuart, M. A. C.; Huck, W. T. S.; Genzer, J.; Muller, M.; Ober, C.; Stamm, M.; Sukhorukov, G. B.; Szleifer, I.; Tsukruk, V. V.; Urban, M.; Winnik, F.; Zauscher, S.; Luzinov, I.; Minko, S., *Nat Mater* **2010,** 9 (2), 101-113.

45. Zhuang, J.; Gordon, M. R.; Ventura, J.; Li, L.; Thayumanavan, S., *Chemical Society Reviews* **2013,** 42 (17), 7421-7435.

46. Bromberg, L.; Creasy, W. R.; McGarvey, D. J.; Wilusz, E.; Hatton, T. A., *ACS Applied Materials & Interfaces* **2015,** 7 (39), 22001-22011.

47. Doring, A.; Birnbaum, W.; Kuckling, D., *Chemical Society Reviews* **2013,** 42 (17), 7391-7420.

48. Okesola, B. O.; Smith, D. K., *Chemical Society Reviews* **2016,** 45 (15), 4226-4251.

49. Smith, B. M., *Chemical Society Reviews* **2008,** 37 (3), 470-478.

50. Wilson, C.; Main, M.; Cooper, N.; Briggs, M. E.; Cooper, A. I.; Adams, D., *Polymer Chemistry* **2017**.

51. Wright, A. J.; Main, M. J.; Cooper, N. J.; Blight, B. A.; Holder, S. J., *ACS Applied Materials & Interfaces* **2017,** 9 (37), 31335-31339.

52. Piana, F.; Facciotti, M.; Pileio, G.; Hiscock, J. R.; Van Rossom, W.; Brown, R. C. D.; Gale, P. A., *RSC Advances* **2015,** 5 (16), 12287-12292.

53. Sambrook, M. R.; Notman, S., *Chemical Society Reviews* **2013,** 42 (24), 9251-9267.

54. Hiemenz, P.; Rajagopalan, R., Principles of surface and colloid chemistry. Marcel Dekker Inc., New York: 1997.

55. Fung, B. M.; Khitrin, A. K.; Ermolaev, K., *Journal of Magnetic Resonance* **2000,** 142 (1), 97-101.

56. Torchia, D. A., *Journal of Magnetic Resonance (1969)* **1978,** 30 (3), 613-616.

57. Morcombe, C. R.; Zilm, K. W., *Journal of Magnetic Resonance* **2003,** 162 (2), 479-486.

58. Eckert, H.; Wachs, I. E., *The Journal of Physical Chemistry* **1989,** 93 (18), 6796-6805.

59. Crocker, J. C.; Grier, D. G., *Journal of Colloid and Interface Science* **1996,** 179 (1), 298-310.

60. Day, V. W.; Klemperer, W. G.; Maltbie, D. J., *Journal of the American Chemical Society* **1987,** 109 (10), 2991-3002.

61. Li, D.; Song, J.; Yin, P.; Simotwo, S.; Bassler, A. J.; Aung, Y.; Roberts, J. E.; Hardcastle, K. I.; Hill, C. L.; Liu, T., *Journal of the American Chemical Society* **2011,** 133 (35), 14010-14016.

62. Hernandez, B. A.; Chang, V.; Villanueva, I.; Heagy, M. D., *Journal of Organic Chemistry* **1999,** 64 (18), 6905-6906.

63. Han, J. W.; Hardcastle, K. I.; Hill, C. L., *European Journal of Inorganic Chemistry* **2006,** 2006 (13), 2598-2603.

64. Chen, Q.; Goshorn, D. P.; Scholes, C. P.; Tan, X. L.; Zubieta, J., *Journal of the American Chemical Society* **1992,** 114 (12), 4667-4681.

65. Wu, P.; Chen, J.; Yin, P.; Xiao, Z.; Zhang, J.; Bayaguud, A.; Wei, Y., *Polyhedron* **2013,** 52, 1344-1348.

66. Sullivan, M. J.; Maciel, G. E., *Anal Chem* **1982,** 54 (9), 1615-1623.

67. Cantekin, S.; de Greef, T. F. A.; Palmans, A. R. A., *Chemical Society Reviews* **2012,** 41 (18), 6125-6137.

68. Barba-Bon, A.; Costero, A. M.; Parra, M.; Gil, S.; Martínez-Máñez, R.; Sancenón, F.; Gale, P. A.; Hiscock, J. R., *Chemistry – A European Journal* **2013,** 19 (5), 1586-1590.

69. Sambrook, M. R.; Hiscock, J. R.; Cook, A.; Green, A. C.; Holden, I.; Vincent, J. C.; Gale, P. A., *Chemical Communications* **2012,** 48 (45), 5605-5607.

70. Carniato, F.; Bisio, C.; Psaro, R.; Marchese, L.; Guidotti, M., *Angewandte Chemie International Edition* **2014,** 53 (38), 10095-10098.

71. Li, J.-K.; Dong, J.; Wei, C.-P.; Yang, S.; Chi, Y.-N.; Xu, Y.-Q.; Hu, C.-W., *Inorganic Chemistry* **2017,** 56 (10), 5748-5756.

72. Kinnan, M. K.; Creasy, W. R.; Fullmer, L. B.; Schreuder-Gibson, H. L.; Nyman, M., *European Journal of Inorganic Chemistry* **2014,** 2014 (14), 2361-2367.

73. Mondloch, J. E.; Katz, M. J.; Isley Iii, W. C.; Ghosh, P.; Liao, P.; Bury, W.; Wagner, G. W.; Hall, M. G.; DeCoste, J. B.; Peterson, G. W.; Snurr, R. Q.; Cramer, C. J.; Hupp, J. T.; Farha, O. K., *Nat Mater* **2015,** 14 (5), 512-516.

74. Liu, Y.; Howarth, A. J.; Vermeulen, N. A.; Moon, S.-Y.; Hupp, J. T.; Farha, O. K., *Coordination Chemistry Reviews* **2016**.

Chapter 3: Selective Aerobic Sulfoxidation by Br_x/NO_x Systems

With Daniel Collins-Wildman, Yurii Geletii, and Rachel Slaugenhaupt

3.1 Introduction: Oxidation of Sulfides

The work outlined in this section is based on the studies on related systems performed by Zhen Luo in the Hill lab. In this work, a variety of experiments were undertaken to investigate the oxidation of sulfides to sulfoxides using a system consisting of tetrabutylammonium bromide (TBA-Br), tetrabutylammonium nitrate (TBA-NO_3), and an acid source. With mild heating, this system was able to quantitatively convert CEES to the sulfoxide CEESO using O_2 as the terminal oxidant.[1] This manuscript involved several mechanistic investigations which will be outlined in the following sections. The publication also notes that the tribromide anion (Br_3^-) may be an important intermediate in the reaction. Since this publication, several reports have investigated the use of tribromide in related sulfoxidation reactions. Reinvestigation of this work was carried out with this in mind, producing dramatic results including significant rate enhancements. Additionally, the current work investigates the use of transition metal catalysts in this system and reveals a significant rate enhancement effect as well as colorimetric detection capability through the addition of Cu(II). This work reveals substantial developments towards achieving rapid, selective, and mild catalytic systems for the decontamination of HD. However, due to the extraordinary complexity of these systems, a full understanding of the mechanism remains elusive.

3.1.1 Overview of Sulfoxidation Reactions

Sulfoxides are very important intermediates in the synthesis of a variety of chemically and biologically active molecules. [2-7] Since the first reports of the synthesis of sulfoxides in 1865, a multitude of methods have been developed for carrying out this transformation through oxidation of the corresponding sulfides.[4] However, sulfoxidation reactions are complicated due to the tendency for sulfoxides to be further oxidized to sulfones. Because of this, the development of

oxidants and catalysts that selectively synthesize sulfoxides from sulfides and avoid overoxidation to the sulfone are highly sought. Despite a variety of advances, this field remains an active area of research owing to the challenge of developing systems that are both rapid and selective for the sulfoxide product.

Many of the sulfoxidation catalysts that have been developed have employed harsh and stoichiometric oxidants, such as sodium hypochlorite or *m*-chloroperbenzoic acid. Recently, therefore, there has been significant interest in developing sulfoxidation catalysts that are both catalytic (and therefore do not produce as much waste) and use "green" oxidants such as oxygen or hydrogen peroxide as the terminal oxidants. Hydrogen peroxide is capable of oxidizing sulfides, but often results in formation of mixtures of sulfoxide and sulfone product.[8] The addition of catalysts to hydrogen peroxide-based oxidation systems is therefore required to improve selectivity. Many transition metals (Ti, Mo, Fe, V, W, Re, Ru, Mn) have been found to catalyze these transformations, some with high selectivity or the capability to generate chiral sulfoxides.[5, 9] However, despite the many substantial advances in this highly active field, a primary issue still persists in all systems involving the use of hydrogen peroxide: it is a stoichiometric oxidant and must be continuously supplied for reactions to continue. For this reason, catalysts capable of performing O_2-based oxidations under mild conditions are highly desirable in a variety of organic transformations.[10-15] Air-based oxidations are cheap, atom economical, and generally do not produce harmful byproducts, in accordance with "green" chemistry principles.[16-17] Because of this, selective aerobic oxidation of sulfides to sulfoxides has received a significant deal of attention for many years.[2-7]

The use of stoichiometric oxidants is particularly disfavored for use in decontamination reactions due to issues with transportation and stability of the reactive solutions. Sections 1.3.1 and 2.3.3 of this work discussed the oxidation of sulfides in the context of decontamination of CWAs. Sulfide-containing CWAs such as the vesicant HD remain significant threats despite international regulation by the Chemical Weapons Convention.[18-19] HD can be decontaminated through oxidation, hydrolysis, or dehalogenation, but the latter two processes are disfavored owing to the highly hydrophobic nature of HD.[20] Because of this, oxidation of the sulfide to the nonvesicant sulfoxide of the HD has been the topic of several recent studies.[21-26] This reaction is challenging because it must both be rapid and highly selective, as the sulfone product retains significant vesicant activity (Figure 3.1).[24]

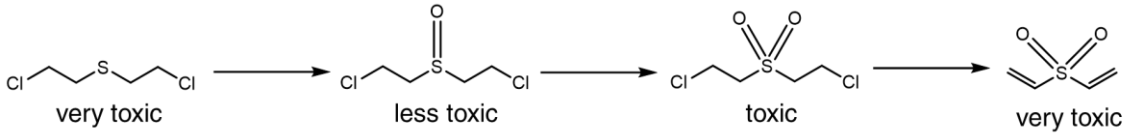

Figure 3.1. Oxidation pathways of HD and associated relative toxicities.

Oxygen by itself is not capable of rapidly oxidizing most sulfides. Thus, catalysts are required to facilitate this transformation. Development towards this aim has lagged due to issues with overoxidation of the sulfoxides.[27] Despite this, many reactions have successfully employed various transition metal catalysts such as those based on Ru, V, Cu, Mn, W, Pb, Ti, Al, or Fe for the selective aerobic synthesis of sulfoxides.[27-28] In addition, several photocatalytic systems have been developed which employ photocatalysts to generate triplet oxygen, which is capable of oxidizing sulfides.[29] However, light-activated catalysts also tend to have issues selectively producing the sulfoxide over the sulfone, and are generally not favorable for use in field decontamination situations due to the requirement for high-intensity light.

Several catalytic systems that have been developed for aerobic sulfoxidation do not require a transition metal catalyst.[9] Halogens have been widely studied and explored for their ability to carry out sulfoxidation reactions for many years. Cl_2 and Br_2 oxidize sulfides through formation of halosulfonium intermediates which are hydrolyzed to form sulfoxides.[4] A primary disadvantage of these methods is that they produce HCl or HBr, which can generate unfavorable side products. To prevent this, compounds such as tertiary amines can be added to scavenge the hydrogen halide products.[30-31] Quaternary ammonium tribromides have also shown promise as mild and efficient oxidants, selectively producing sulfoxides with minimal overoxidation. Several different cations have been employed, with a common reagent being cetyltrimethylammonium tribromide due to its dual surfactant and catalytic capabilities.[32-33] Recently, there have been efforts to incorporate tribromide anions in advanced materials such as magnetic nanoparticles or zeolites to create reactive solid catalysts.[34-35] Though systems incorporating tribromide show high activity, it remains unclear whether Br_3^- or Br_2 is the active oxidant. Further complicating this issue is the equilibrium between Br_3^- and Br_2/Br^-, which is shifted towards the formation of Br_3^- in MeCN (the solvent in which most of these oxidations have been studied) with a formation constant of $9 \bullet 10^6$ M^{-1} (Equation 1).[36-37]

$$Br_2 + Br^- \rightleftharpoons Br_3^- \quad (1)$$

Though these catalytic systems are highly effective for mild and selective sulfoxidation, halide-based reactions are stoichiometric, making them impractical and uneconomical. To address this, several reports have made bromine-based reactions catalytic by adding nitrogen oxide (NO_x) reagents that are capable of reoxidizing bromide to Br_2 or Br_3^-.[1, 38-41] Importantly, after oxidation of Br^-, the reduced NO_x species can be reoxidized by O_2, making air the terminal oxidant in these systems.

3.1.2 Introduction to Br_x/NO_x systems

Previous work has shown that NO_x species are capable of oxidizing Br^-. For example, Lengyel et. al. studied the oxidation of Br^- by HNO_3 in aqueous solution in the absence of oxygen, and proposed the reaction shown in Equation 2.[42]

$$NO_3^- + 2\,Br^- + 3H^+ \rightleftharpoons Br_2 + HNO_2 + H_2O \quad (2)$$

Due to the extremely complex speciation of NO_x and Br_x in solution (especially in mixed water/acetonitrile solvent that is typical for these reactions), characterization of systems involving these reactions is a significant challenge. Several NO_x species (NO_3^-, NO_2^-, NO, NO_2, N_2O_4, and BrNO) are thought to be involved as intermediates, but it is unclear exactly which species are active for which steps in the cycle, and if there may be additional species responsible for the observed activity.[1, 42] Because of this, reports that have studied Br_x/NO_x systems have generally been empirical in nature, with very few attempting to understand mechanistic details. A report by Luo et. al. in 2011 examined this reaction and suggested a hypothesis for the mechanism of the sulfoxidation in Br_x/NO_x systems, shown in Figure 3.2.

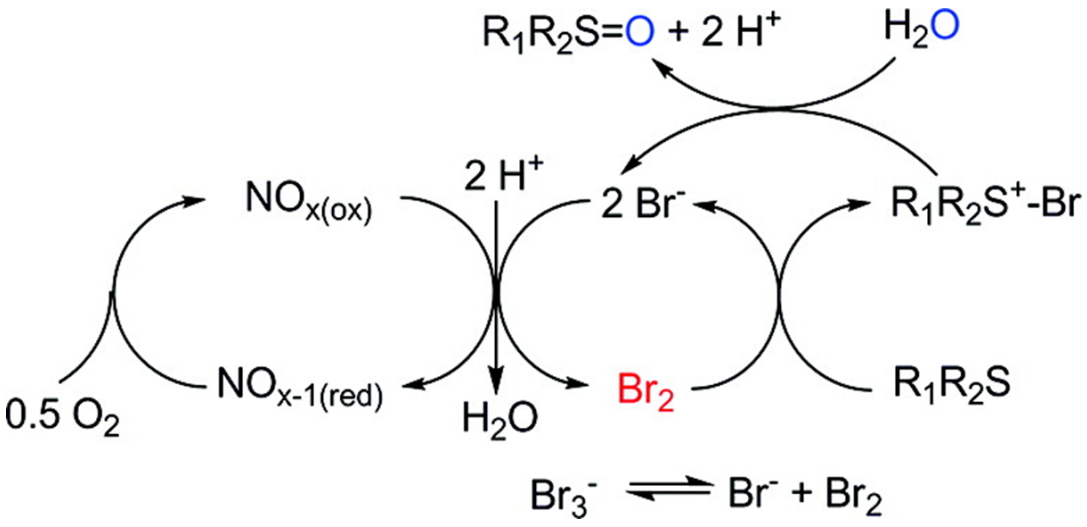

Figure 3.2. Proposed mechanism for aerobic sulfoxidation in Br_x/NO_x systems by Luo et. al. Reprinted with permission from Luo et. al., *ACS Catalysis* **2011**, 1 (10), 1364-1370. Copyright 2011 American Chemical Society.[1]

In this mechanism, the sulfide is first brominated to form a bromosulfonium intermediate. Some reports suggest that this intermediate may be further brominated to form a bromosulfonium bromide. This intermediate then reacts with water to generate the sulfoxide product and bromide anions. These bromide anions, under acidic conditions, react with the oxidized NO_x species to produce Br_2, and the reduced NO_x species react with O_2 to eventually regenerate the reactive NO_x oxidized species. This overall reaction is shown in Equation 3.

$$R_2S + \frac{1}{2}O_2 \xrightarrow{Br_x/NO_x} R_2SO \qquad (3)$$

A more recent study by Le et. al. proposes an alternate mechanism in which NO_3^- is directly involved in the oxidation of the bromosulfonium intermediate, as shown in Figure 3.3.

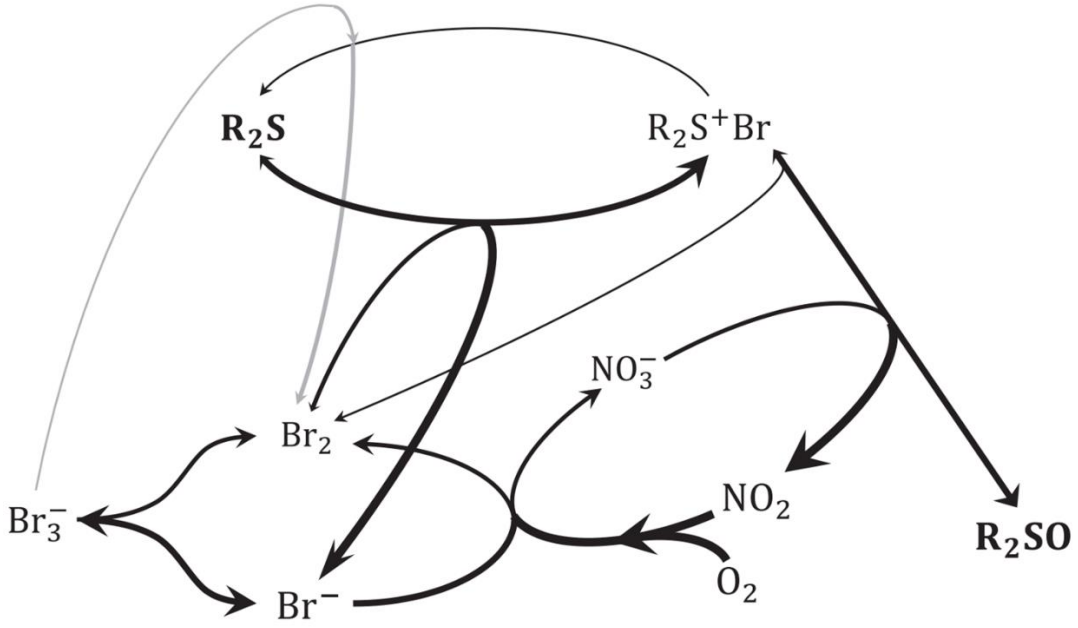

Figure 3.3. Proposed mechanism for aerobic sulfoxidation in Br_x/NO_x systems by Le et. al. Reprinted with permission from Le et. al., *J. Hazard. Mater.* **2019**, 365, 511-518. Copyright 2019 Elevisier.[38]

In this study, the authors suggest that it is NO_3^-, not H_2O, which converts the bromosulfonium intermediate to the sulfoxide product, with the resulting NO_2 ultimately being reoxidized by O_2. Other studies have suggested that there may be several independent mechanisms occurring simultaneously. One report demonstrated the catalytic oxidation of sulfides by NO_2 in the absence of any bromide species, through the mechanism shown in Figure 3.4.[43] The authors suggest that NO_2 (in equilibrium with N_2O_4) disproportionates to form a nitrosonium nitrate complex with the sulfide species, which undergoes an electron transfer to generate a sulfide cation radical and NO, followed by oxygen transfer from nitrate.

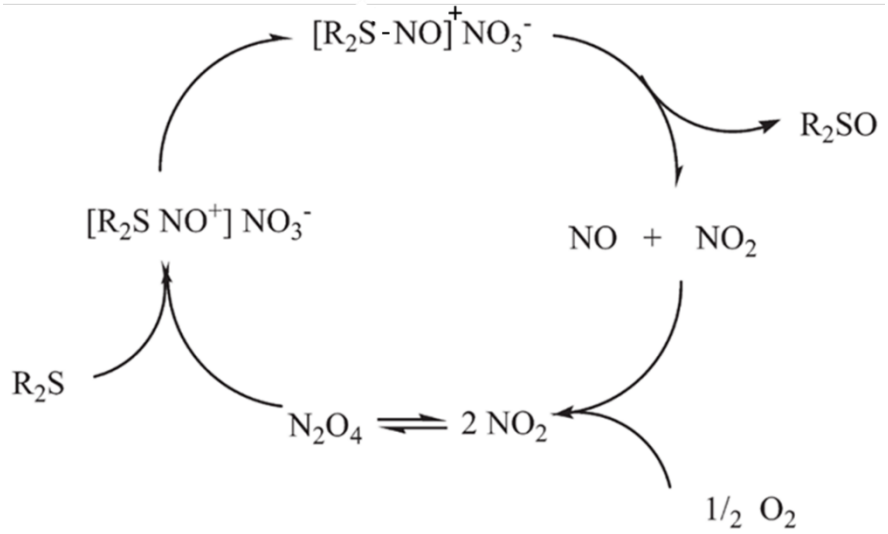

Figure 3.4. Proposed mechanism by Bosch et. al. for aerobic sulfoxidation by NO_2. Reprinted with permission from Kinen et. al., *J. Org. Chem*., **2009**, 74 (18), 7132–7139. Copyright 2009 American Chemical Society.[43-44]

In addition to research aimed at understanding the mechanism of sulfoxidation in Br_x/NO_x systems, a few studies have examined ways of catalyzing these reactions using transition metals. In particular, Rossi, Martin et. al. have shown fast and selective sulfoxidation using $FeBr_3$ in several different systems.[44-46] The authors postulated that there were two primary reaction pathways, one in which the sulfide binds to Fe(III) before oxidation by NO_x species, and one where the sulfide is directly oxidized by NO_x species. Interestingly, they do not claim that bromide has any role in the reaction in this system.

Clearly, these systems are extremely complex and their mechanisms are difficult to quantify, rendering a complete understanding of these systems elusive despite active research in this area. The following sections describe experiments aimed at developing a greater understanding of the Br_x/NO_x system. Additionally, they will describe research demonstrating the significant rate enhancements achieved upon addition of Cu(II) to the system.

3.2 Experimental

3.2.1 General Methods

Uv/Vis measurements. All UV-Vis spectra were acquired using Agilent 8453 spectrophotometer equipped with a diode-array detector.

GC data were obtained using a Hewlett Packard HP 6890 GC system equipped with a HP-5 5% phenyl methyl siloxane column.

Solution ^{13}C NMR spectroscopic measurements were made on a Bruker Ascend^{TM} 600 MHz spectrometer with a prodigy cryoprobe.

Stopped-flow kinetics. Kinetic curves were obtained using a HI-TECH Scientific KinetAsyst SF-61sX2 sample-handling unit with a diode array spectrophotometer.

Oxidation of CEES catalyzed by Br_x and NO_x. The following is a generalized scheme. Specific reaction details can be found in the figure captions for the corresponding experiments. Stock solutions of tetrabutylammonium tribromide (TBA-Br_3), tetrabutylammonium bromide (TBA-Br), tetrabutylammonium nitrate (TBA-NO_3), tetrabutylammonium nitrite (TBA-NO_2), *p*-toluenesulfonic acid monohydrate (*p*-TsOH) and metal nitrates were prepared with a concentration of 50mM in acetonitrile. To prepare the catalytic reactions, volumes of each of these stock solutions were added to a 20-mL glass vial fitted with a polytetrafluoroethylene (PTFE) septum followed by addition of H_2O and the 1,3-dichlorobenzene (40 µL) internal standard. MeCN was

added to make the total volume equal to 5 mL after addition of all components, including CEES. CEES (60 L, 514 mmol, 103 mM) was added to initiate the reaction. For reactions run under O_2 atmosphere, the 20-mL glass vial was purged with O_2 and CH_3CN used in all stock solutions and for the reaction were purged with O_2 prior to use. O_2 concentration was maintained during reaction by a balloon attached to the vial. Conversion to product was monitored by GC analysis of the CEES peak. The selectivity for CEESO was determined using ^{13}C NMR of the reaction mixture after the reaction.

3.3 Results and Discussion

3.3.1 Revisiting the Br_x/NO_x reaction

The studies by Luo et. al. employed Br^-, NO_3, and H^+ as starting materials for their sulfoxidation studies. Though these reactions do proceed to completion, they occur with a significant induction period and then only slowly lead to product formation, even with heating of the solution.[1] After analyzing more recent studies, and based off of suggestions from the Luo et. al. paper that Br_3^- may be a key reactive species, reactions were performed to assess the difference that the substitution of Br^- for Br_3^- would make. Figure 3.5 shows a comparison between these two systems.

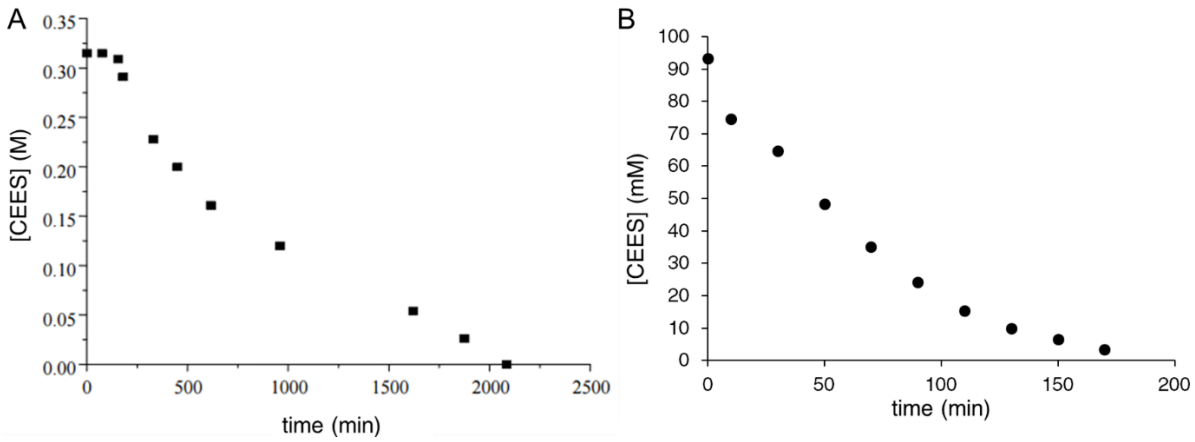

Figure 3.5. Comparison of Br_x/NO_x catalytic conditions between Luo et. al. and the present work. (**A**) [CEES] = 320 mM, [TBA-NO_3] = 16 mM, [TBA-Br] = 16 mM, MeCN, 70 ºC, 1 atm air. (**B**) [CEES] = 100 mM, [TBA-NO_3] = 5 mM, [TBA-Br_3] = 5 mM, MeCN, 23 ºC, 1 atm air. Br_x in terms of potential Br_2 created from Br^- or Br_3^- for ease of comparison. The Br_2: NO_3: CEES ratios are (**A**) 1: 2: 40 and (**B**) 1: 0.67: 75.

Even though the reaction from Luo et. al. has a higher catalyst: substrate ratio and takes place at elevated temperature, the reaction is more than an order of magnitude slower than if Br_3^- is used as the Br_x source. There is also the absence of an induction period with Br_3^- present. This suggests that in the original system, oxidation of Br^- to form Br_2 and Br_3^- is a very slow process that, once a critical concentration of the active catalyst is produced, then proceeds to oxidize CEES. This difference in rate is quite dramatic and was a promising discovery that led to further investigations into this system, as will be described below.

3.3.2 Reaction Optimization

Due to the complex nature of the Br_x/NO_x reaction system, the first steps taken to probe the reaction were to examine the effect of varying the concentrations of each of the reaction components. Many of the reports on these systems note a substantial dependence of the reaction rate on water. Thus, one of the first experiments in reinvestigating this system was to test the water dependence of the

reaction rate in the catalytic system so that an optimal [H_2O] could be used in subsequent studies (Figure 3.6).

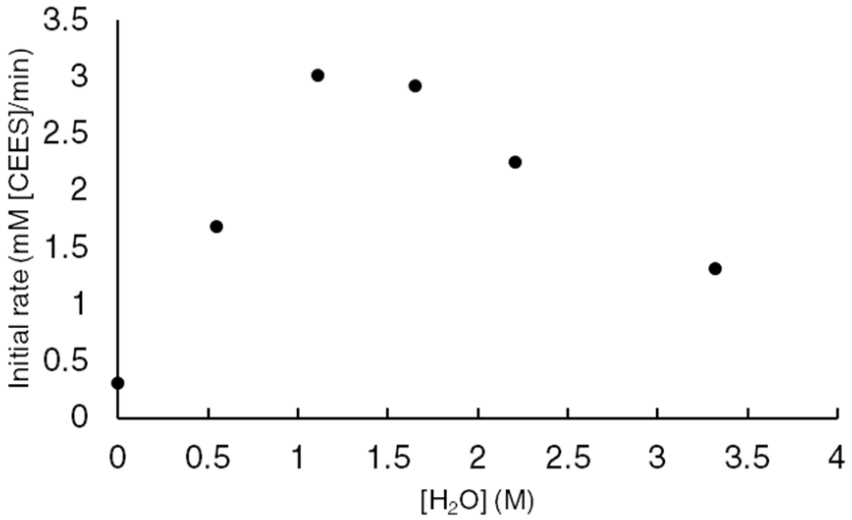

Figure 3.6. Optimization of [H_2O] in Br_x/NO_x-catalyzed CEES oxidation. [CEES] = 100 mM, [TBA-NO_3] = 10 mM, [TBA-Br_3] = 10 mM, X µL H_2O, 4.9-X µL MeCN, 23 ºC, 1 atm air.

There is clearly a strong and complex dependence on [H_2O] in this system. At low [H_2O], the reduced rate is likely due to water being directly involved in the conversion of the sulfide. However, the situation becomes more complicated at elevated [H_2O]. The observed decrease in the rate at higher concentrations is potentially attributable to water affecting the equilibrium in Equation 1: more water decreases the Br_3^- concentration and favors the formation of Br_2 and Br^-. Because both Br_2 and Br_3^- absorb in the visible region, we can use UV/Vis spectroscopy techniques to investigate the formation of these compounds under various conditions. Despite being relatively well-studied, the reported molar absorptivity values for Br_3^- range from 25,000 M^{-1} cm^{-1} at 266 nm to 39,000 M^{-1} cm^{-1} at 270 nm.[47-48] Br_2 has a much lower molar absorptivity (~200 M^{-1} cm^{-1} at 412 nm).[49] The absorption peaks for Br_3^- and Br_2 overlap, making it challenging to quantify the exact amount of each compound. However, Br_2 and Br_3^- exhibit an isosbestic point at 446 nm, allowing for measurements taken at that wavelength to reflect the concentration of both Br_2 and Br_3^-.[50-51]

Because of the difference in molar absorptivity, the absorbance at 446 nm arises primarily from Br_3^- but includes some contribution from Br_2. Using UV/Vis spectroscopy, we observe that increasing the [H_2O] causes the Br_3^- peak to decrease substantially (Figure 3.7).

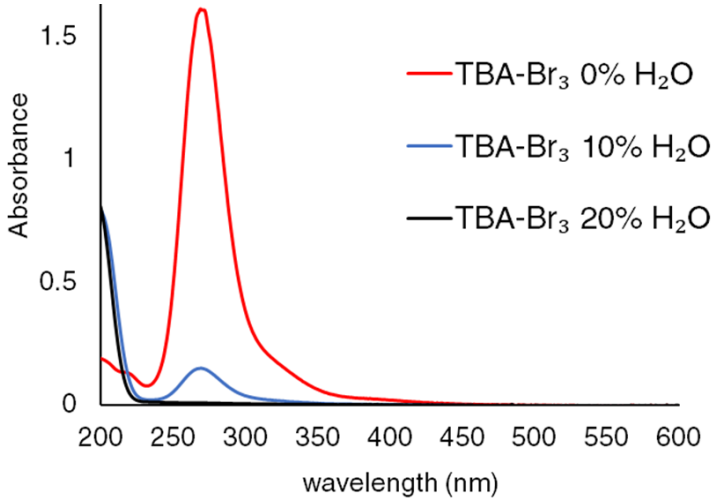

Figure 3.7. UV/Vis spectra of Br_3^- with different amounts of H_2O. Solutions composed of TBA-Br_3 in MeCN with different % H_2O. Absorbance measurements taken at 466 nm.

If the decrease in activity from elevated [H_2O] is caused by a reduction in the amount of tribromide present, it would suggest that Br_3^- is a more active oxidant in the system. To test this, catalytic reactions were run beginning with Br_3^- and Br_2 as reagents while keeping the total amount of bromine constant for ease of comparison. These studies, shown in Figure 3.8, reveal that starting the reaction with Br_3^- instead of Br_2 does appear to result in an increased rate of sulfoxidation. Addition of Br^- to the Br_2 system (which would result in formation of Br_3^-) achieves the same rate as in the Br_3^--only system.

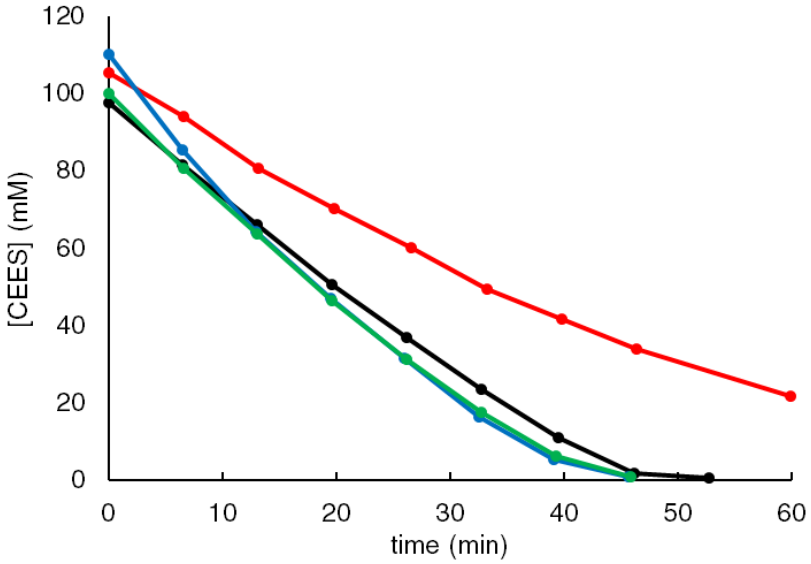

Figure 3.8. Catalytic sulfoxidation rates comparing Br_3^- and Br_2. [CEES] = 100 mM, [TBA-NO_3] = 10 mM, [*p*-TsOH] = 10 mM, 2% H_2O in MeCN, 23 ºC, 1 atm air. Bromide source: (●) 7.5 mM Br_2, (●) 5 mM TBA-Br_3, (●) 5 mM TBABr_3 + 5 mM TBA-Br, (●) 5 mM Br_2 + 5mM TBA-Br.

Though Br_3^- does appear to have an increased rate compared to Br_2, the relative rate difference is not enough to account for the observed decrease in rate from adding excess water in Figure 3.6. Thus, it is likely that an increased [H_2O] affects the complex NO_x equilibria in a way that decreases the rate. Another effect could be the change in pKa as the solvent composition changes through the addition of water, which may profoundly impact the species present in these solutions. Neutral reaction components have substantially lower activities in non-aqueous solvents, and even small changes in the amount of water can substantially alter the solvent polarity and other parameters.[52] The effect of H_2O, then, is too complex for a complete understanding at this stage. However, for future reactions, the optimized [H_2O] determined from the experiments in Figure 3.6 are used.

The Luo et. al. study also mentioned the requirement of H^+ for the reaction to proceed and suggested it was involved in the reoxidation of Br^-. In the initial studies reexamining this system, high rates were achieved in the absence of H^+ addition. In the Br_3^--containing system, H^+ was

likely formed after the hydrolysis step, as shown in Figure 3.2. One advantage of using Br_3^- instead of Br^- as the starting material, then, is that it generates the H^+ that is used in the reaction and does not require external acidification. In order to understand the effect of H^+, reactions were carried out on the catalytic system with varying amounts of *p*-TSOH (Figure 3.9).

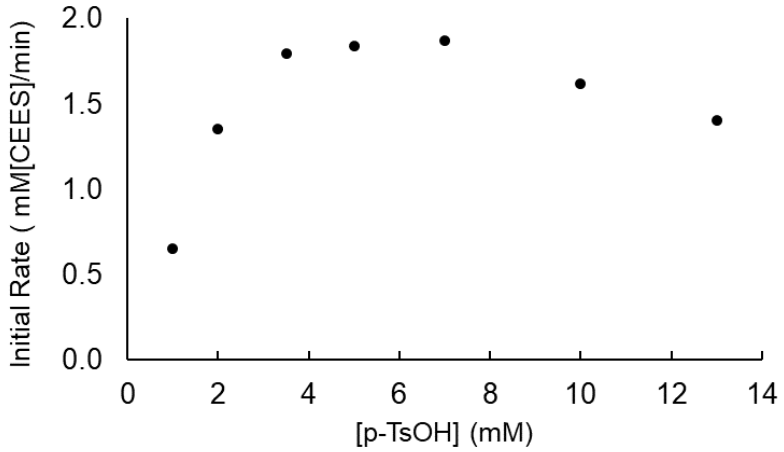

Figure 3.9. Optimization of [p-TsOH] in the Br_x/NO_x catalytic oxidation of CEES. [CEES] = 100 mM, [TBA-NO_3] = 5 mM, [TBA-Br_3] = 5 mM, 2% H_2O in MeCN, 23 ºC, 1 atm air. Varied [*p*-TsOH].

These results also show a complex relationship on the amount of acid present in solution. There is a clear increase after the addition of up to 4 mM *p*-TsOH. However, as the concentration increases past 8 mM a decrease in the initial rate is observed. It is unclear exactly what causes this difference in rates due to $[H^+]$ because of the large number of pathways that this would likely affect. However, this allows for the use of an optimized amount of *p*-TsOH in subsequent experiments.

There was also interest in determining whether alternate acids could be used in the reaction, such as the phosphovanamolybdate POM $H_5PV_2Mo_{10}O_{40}$ and the sulfonic acid-based fluoropolymer Nafion (Figure 3.10). These experiments demonstrated that these alternative acids could be employed with only minor differences in the reaction rate.

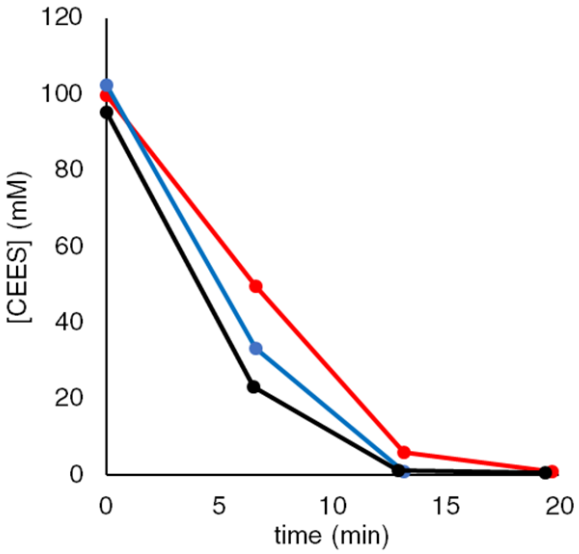

Figure 3.10. CEES sulfoxidation using different acidic materials. [CEES] = 100 mM, [TBA-NO_3] = 5 mM, [TBA-Br_3] = 3.3 mM, 2% H_2O in MeCN, 23 ºC, 1 atm air. Acid source: (●) 1.67 mM, (●) 20 mg Nafion, (●) 10 mM *p*-TsOH.

After optimizing the amount of water and acid, the effect of the concentration of each of the catalytic components on the reaction rate was considered. The effect of [Br_3^-] shows a much more straightforward behavior, with a linear increase of the rate with increasing [Br_3^-] up to ~ 2.5 mM Br_3^- (Figure 3.11). After this, the initial rate reaches a plateau, which is likely attributed to the maximum rate that can be achieved given the rate of diffusion of O_2 from the atmosphere into solution.

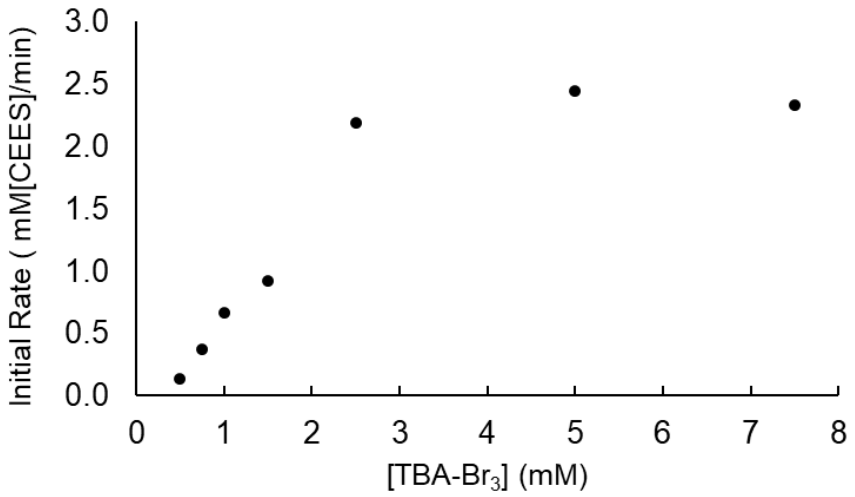

Figure 3.11. Effect of [Br_3^-] on rate of catalytic sulfoxidation reaction. [CEES] = 100 mM, [TBA-NO_3] = 5 mM, [*p*-TsOH] = 5 mM, 2% H_2O in MeCN, 23 ºC, 1 atm air. Varied [TBA-Br_3].

Similarly, the [NO_3^-] has a relatively straightforward effect on the reaction rate, as initially there appears to be a linear dependence followed by a plateau at roughly the same rate as where the [Br_3^-] experiments plateau (Figure 3.12).

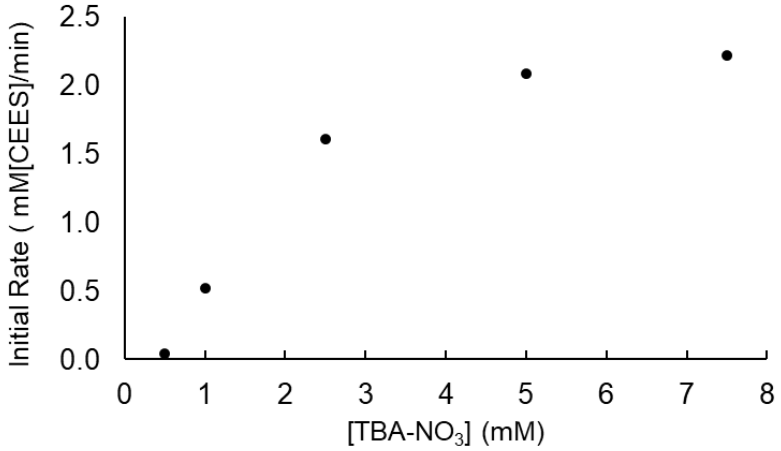

Figure 3.12. Effect of [NO_3^-] on rate of catalytic sulfoxidation reaction. [CEES] = 100 mM, [TBA-Br_3] = 5 mM, [*p*-TsOH] = 5 mM, 2% H_2O in MeCN, 23 ºC, 1 atm air. Varied [TBA-NO_3].

3.3.3 Mechanistic Studies

The mechanism of Br_x/NO_x sulfoxidation is clearly extremely complex. However, information about the system can be obtained to understand key reaction steps, which then inform the design of more effective catalytic systems. One of the parameters to be explored was the effect of the nucleophilicity/electrophilicity of the sulfide on the reaction rate, as the first step in the proposed mechanism by Luo et. al. involves a nucleophilic attack of the sulfide on Br_x. Reactions using different sulfides were therefore used to observe these trends (Figure 3.13).

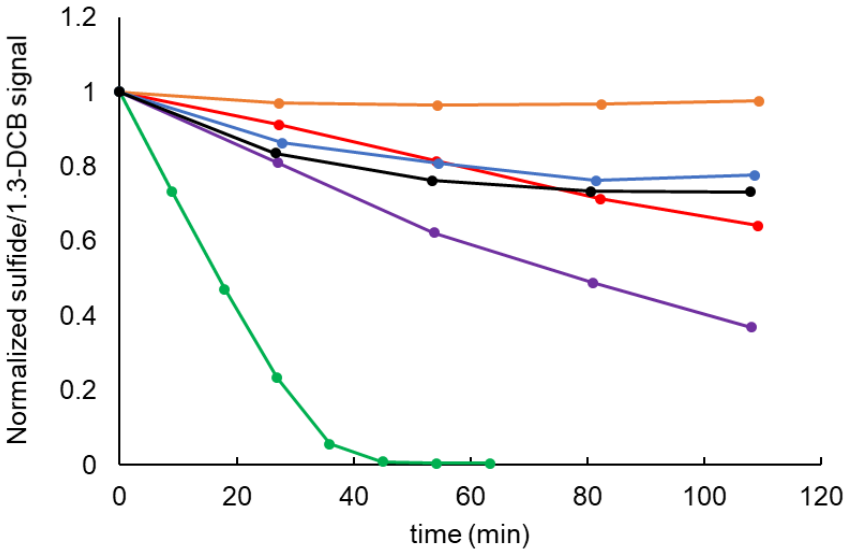

Figure 3.13. Catalytic sulfoxidation reaction using different sulfides. [Sulfide] = 100 mM, [TBA-NO_3] = 5 mM, [TBA-Br_3] = 5 mM, [*p*-TsOH] = 5 mM, 2% H_2O in MeCN, 23 ºC, 1 atm air. Sulfide: (●) CEES, (●) thioanisole, (●) methylthioanisole, (●) chlorothioanisole, (●) benzyl methyl sulfide, (●) THT.

The sulfides employed in this study in order of nucleophilicity were: tetrahydrothiophene (THT) > benzyl methyl sulfide > CEES > methylthioanisole > thioanisole > chlorothioanisole. These reactions were run with identical conditions and with a constant molar amount of sulfide. Counterintuitively, no clear trend emerges from these experiments. Even with the thioanisole derivatives, there is no trend between the nucleophilicity of the sulfide and the rate of the catalytic

reaction. The reason behind the seeming independence of the reaction rate on the sulfide source currently remains unexplained. However, a serendipitous result is that CEES shows the highest activity of all sulfides tested, which is promising for eventual reactions of this catalytic system on HD itself.

Stopped-flow UV/Vis spectroscopy is a very useful method for studying mechanistic details, as it allows for the analysis of individual reaction steps on a rapid timescale. Stopped-flow UV/vis studies were performed by mixing Br_3^- with each of these sulfides, observing the disappearance of the Br_3^- signal at rapid timescales. However, analysis of the thioanisole derivatives was not possible because the corresponding bromosulfonium intermediates have absorptions which overlap with that of Br_3^-. We were, however, able to look at comparisons between THT and CEES using this method, shown in Figure 3.14.

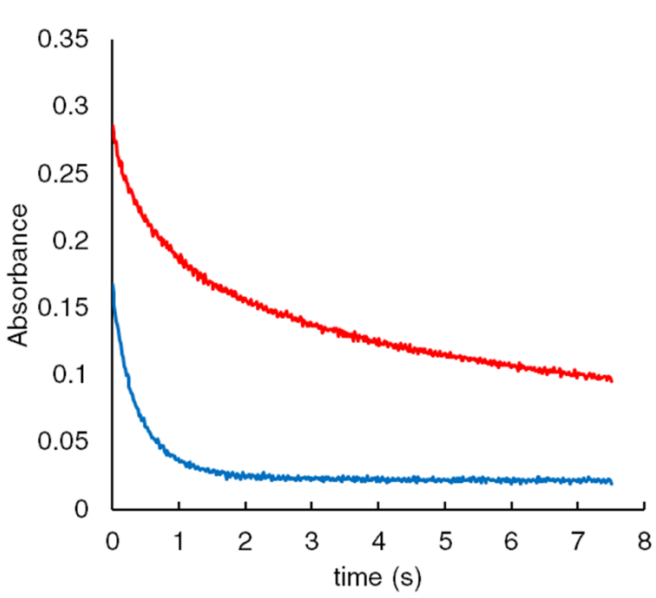

Figure 3.14. Stopped-flow UV/Vis comparison of THT and CEES reactions with Br_3^-. Syringe 1: 6 mM TBA-Br_3, 4% H_2O, 1.5% $HClO_4$ in MeCN. Syringe 2: 200 mM sulfide. (●) THT, (●) CEES. Absorbance measurements taken at 466 nm.

These results show that THT reacts with Br_3^- faster than CEES, though THT has a slower overall catalytic rate. This indicates that the increased nucleophilicity of the sulfide in THT allows it to react with the Br_x species more rapidly, but the corresponding bromosulfonium intermediate formed is stronger than with CEES, making the subsequent hydrolysis step more challenging. This suggests that hydrolysis of the bromosulfonium intermediate may be a rate-limiting step in the overall catalytic process. Accordingly, as the amount of water present is increased, the reaction with THT proceeds more rapidly and further towards completion, as observed in Figure 3.15.

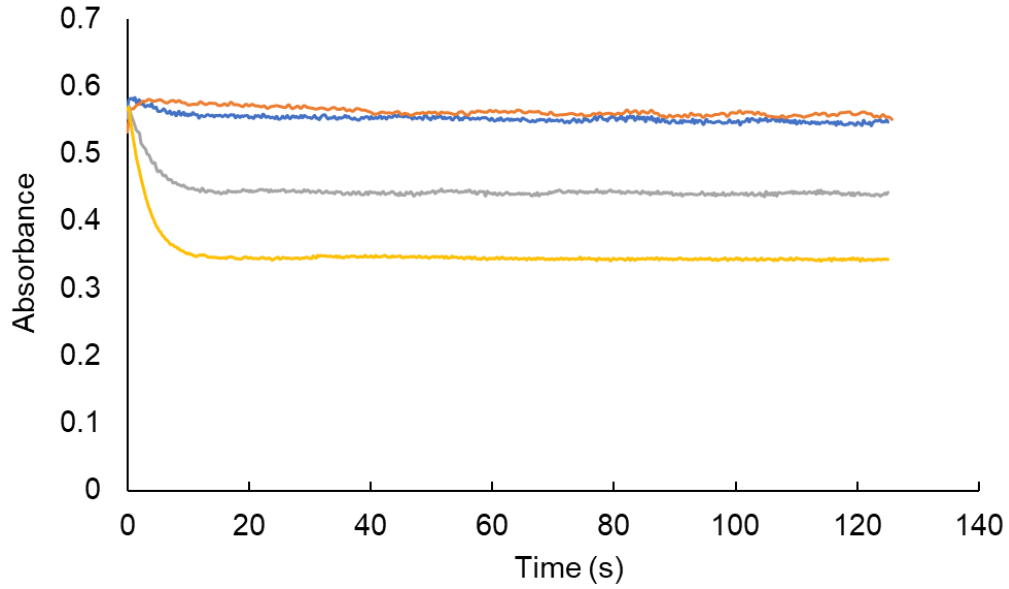

Figure 3.15. Stopped-flow UV/vis of Br_3^- oxidation of THT with different amounts of H_2O. Syringe 1: 5 mM TBA-Br_3, 1.5% $HClO_4$ in MeCN. Syringe 2: 200 mM THT in MeCN with (●) 0 µL, (●) 38 µL, (●) 75 µL, and (●) 100 µL. Absorbance measurements taken at 466 nm.

This lends further evidence to the hypothesis that hydrolysis of the bromosulfonium intermediate is the rate-limiting step under these conditions. After examining the effect of the sulfide, the next step was to perform the reaction using different NO_x sources to observe the effect on the reaction rate. These studies, which used NO_3^-, NO_2^-, and *tert*-butyl nitrite as the NO_x source, are shown in Figure 3.16.

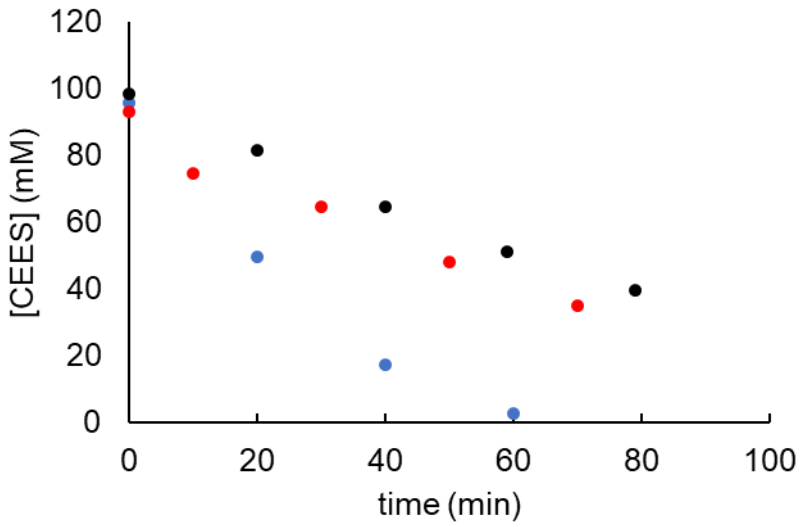

Figure 3.16. Catalytic sulfoxidation reactions using different NO_x starting materials. [CEES] = 100 mM, [NO_x source] = 5 mM, [TBA-Br_3] = 5 mM, [*p*-TsOH] = 5 mM, 1% H_2O in MeCN, 23 ºC, 1 atm air. NO_x sources: (●) $TBANO_3$, (●) $TBANO_2$, (●) *t*-BuONO.

Surprisingly, the reactions with NO_3^- and NO_2^- gave comparable rates. This suggests that NO_3^- or NO_2^- are likely not involved in the rate-limiting step. This is contrary to the expected result based on the study by Le et. al., as they suggest that NO_3^- is involved in the oxidation of the sulfide species.[38] This does not appear to be the case. However, using *tert*-butyl nitrite as the NO_x source results in a faster reaction rate. *Tert*-butyl nitrate dissociates in solution to form NO, which can react with O_2 to form NO_2. NO_2 can react with sulfides through the mechanism shown in Figure 3.4 and can also reoxidize Br^- to Br_2. However, the exact reason behind the enhanced activity is difficult to prove. Stoichiometric reactions performed using NO_3^-, NO_2^-, Br_2, and Br_3^- show that none of these reagents alone are capable of full decontamination of the system (Figure 3.17).

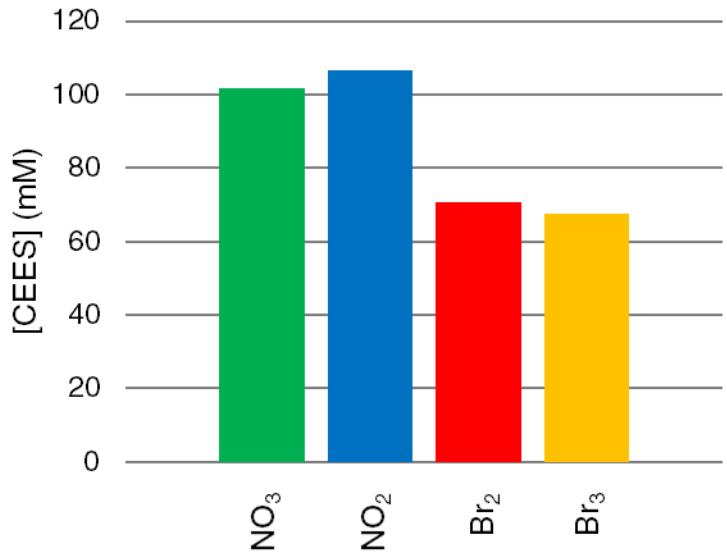

Figure 3.17. Stoichiometric reaction between CEES and NO_x or Br_x species. [CEES] = 50 mM, [NO_x source] = 50 mM, [Br_x source] = 50 mM, [*p*-TsOH] = 10 mM, 2% H_2O in MeCN, 23 ºC, 1 atm air.

Strangely, stoichiometric reactions run with CEES and either Br_2 or Br_3^- only reduce the amount of CEES by ~40%. With NO_3^- or NO_2^-, there is no observable reaction over this timescale. This indicates that there is synergistic activity between these reaction components, as suggested by Le et. al.

An effect that is substantially easier to study is reoxidation of Br^- by NO_x species, as the formation of Br_2/Br_3^- can be tracked by stopped-flow UV/Vis spectroscopy. When mixed with NO_2^-, rapid formation of Br_2/Br_3^- is observed, as shown in Figure 3.18.

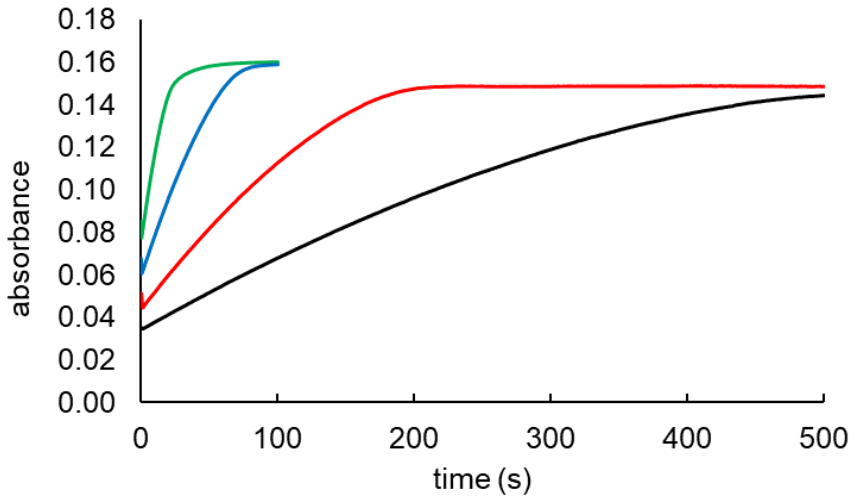

Figure 3.18. Stopped-flow UV/Vis studies of the reoxidation of Br^- by NO_2^-. Syringe 1: 25 mM TBA-Br, 4% H_2O, in MeCN. Syringe 2: 1.5% $HClO_4$, TBA-NO_2 at concentrations of: (●) 1 mM, (●) 2 mM, (●) 4 mM, (●) 8 mM in MeCN. Absorbance measurements taken at 430 nm.

There is a significant [NO_2^-] dependence on the reoxidation rate of Br^-. However, even at elevated concentrations, it is clear that the reoxidation reaction takes place much more slowly than the consumption of the Br_x species, as shown in Figure 3.15. This suggests that for the CEES reaction (where it seems the bromosulfonium intermediate is more reactive than in the case of the other sulfides), the reoxidation of Br^- may be the rate-limiting step. This process has a clear dependence on O_2, as can be seen in Figure 3.19.

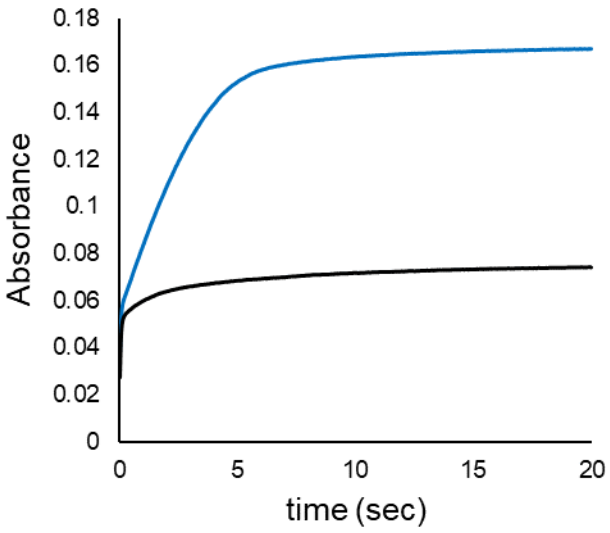

Figure 3.19. Stopped-flow UV/Vis studies of the O_2 dependence of reoxidation of Br^- by NO_2^-. Syringe 1: 25 mM TBA-Br, 4% H_2O, in MeCN. Syringe 2: 1.5% $HClO_4$, 4 mM TBA-NO_2 in MeCN. Measurements taken after purging both syringes with O_2 (●) and with argon (●). Absorbance measurements were taken at 430 nm.

This experiment also demonstrates that NO_2^- reacts with Br^- directly, as there is a very rapid initial rise in absorbance suggestive of this stoichiometric reaction, followed by a more gradual increase attributed to the catalytic reoxidation of Br^-.

3.3.4 Metal-Catalyzed Reactions

Several studies have shown that transition metals can have significant effects in catalyzing the oxidation of sulfides.[44-45, 53-57] Only a small number of studies have examined the effect of transition metals in increasing the rates of sulfoxidation in Br_x/NO_x systems, as described in section 3.1.2. To determine if the addition of transition metals would speed up the system under study, screening trials employing a variety of transition metal nitrates were undertaken (Figure 3.20).

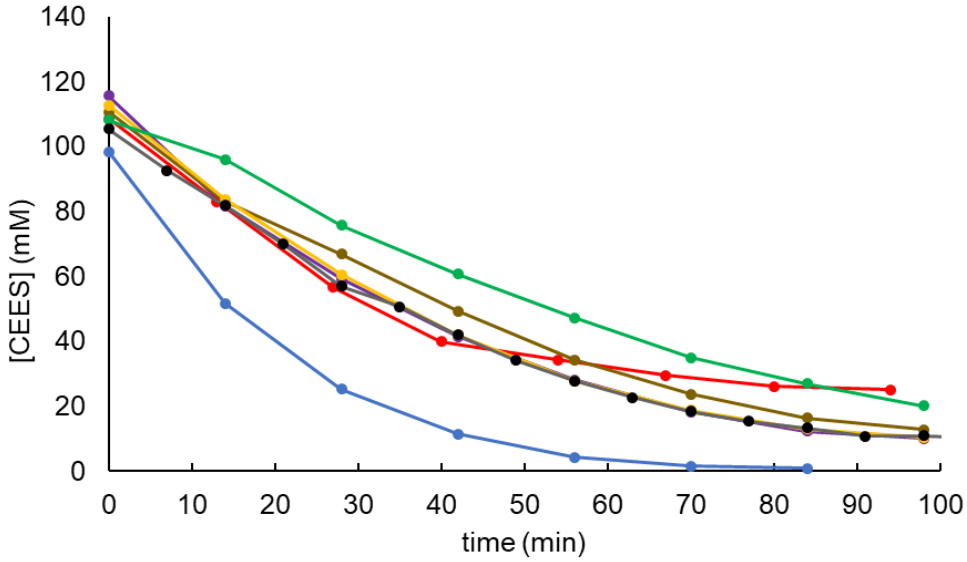

Figure 3.20. Metal screening for Br_x/NO_x sulfoxidation reaction. All reactions run with same total [NO_3^-], [Br_3^-]. [metal], [H_2O], and ionic strength. [metal] = 1.67 mM, [CEES] = 100 mM, [NO_3^-] = 5 mM, [Br_3^-] = 5 mM, 2% H_2O in MeCN, 23 ºC, 1 atm air. Metals: (●)$Cu(NO_3)_2$•3H_2O, (●) $Mn(NO_3)_2$•4 H_2O, (●) $Co(NO_3)_3$•6 H_2O, (●) $Ni(NO_3)_2$•6 H_2O, (●) $Zn(NO_3)_2$,•6 H_2O (●) $Ce(NO_3)_2$•6H_2O. (●) control run without metal. Tetrabutylammonium tetrafluoroborate ($TBABF_4$) was added to equalize the ionic strength.

In general, most of the transition metals in the screening reaction performed no better than the control run in the absence of any metal, and in several instances slowed down the reaction rate. However, the use of $Cu(NO_3)_2$ substantially increased the rate relative to the control, spurring further investigation of the role of Cu in this reaction. Copper is a well-known oxygen activation catalyst, and the development of copper-based oxidation catalysts is a highly active field of research.[27, 58] Aerobic oxidation of reduced POMs by Cu(II) was recently studied by our group.[59]

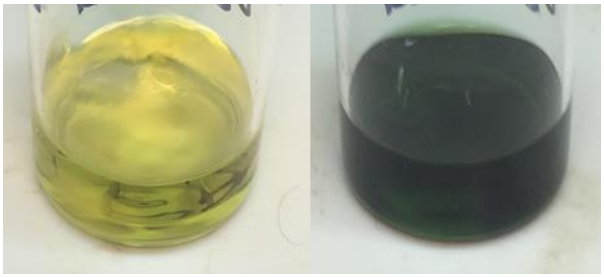

Figure 3.21. Responsive color change behavior in the Br_x/NO_x/Cu(II) system. Left: solution contains 5mM TBA-Br_3, 5mM TBA-NO_3, 10mM *p*-TsOH, and 2% H_2O in MeCN. Right: the system immediately after addition of 100mM CEES.

Addition of Cu(II) to the reaction is especially notable due to a dramatic color change that occurs immediately upon addition of CEES to the catalytic solutions (Figure 3.21). Before CEES addition, the solution is pale yellow in color. However, after CEES addition there is a dramatic color change to produce a dark green color. When the reaction is complete, the solution returns to the initial pale yellow color. The color change can be attributed to the formation of copper bromide species as Br^- is produced during the formation of the bromosulfonium intermediate. A variety of copper bromide species can exist in acetonitrile/water solutions. Titration studies suggest that the green color is a result of a copper dibromide species.[60] Stopped-flow UV/vis studies show the rapid color change activity of this system after Br^-, NO_2^-, and $Cu(ClO_4)_2$ are mixed (Figure 3.22).

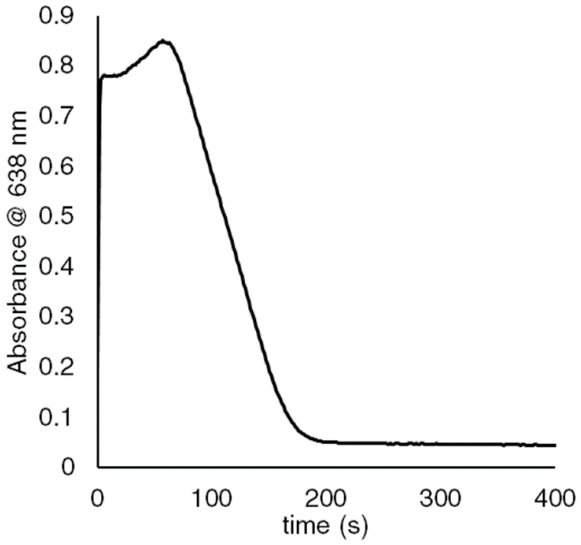

Figure 3.22. Stopped-flow UV/Vis study of the color change resulting from copper bromide species. Syringe 1: 1 mM $Cu(ClO_4)_2$ + 2 mM TBA-NO_2. Syringe 2: 15 mM TBA-Br + 15 mM p-TsOH. Absorbance measurements taken at 638 nm.

In this experiment, one of the syringes contained $Cu(ClO_4)_2$ and HNO_2, and the other contained Br^-. Upon mixing a very rapid (~1s) increase in absorbance at 638nm is observed, consistent with the rapid complexation or Br^- by Cu(II).[60-61] There is a further increase in absorbance over the next ~100s, likely attributed to slower speciation to form other copper bromide species. As the Br- becomes reoxidized by the NO_x species, Br^- is consumed, eventually returning the solution to its original color. The immediate color change during the catalytic reaction, then, indicates that there is rapid formation of Br^- directly upon addition of CEES, confirming that the formation of the bromosulfonium intermediate is a very rapid process. This color change activity is quite promising for applications in decontamination of HD, as the decontaminating solution is capable not only of detecting when the sulfide is present, but also when it has been fully decontaminated.

To understand the effect of [Cu(II)] on the rate of the reaction, initial rates of reactions run with varying amounts of Cu(II) were compared (Figure 3.23). Interestingly, addition of $Cu(ClO_4)_2$ to

the reaction generally increases the rate relative to the reaction run without copper, but further increases in the amount of $Cu(ClO_4)_2$ does not further increase the rate and prevents the reaction from running to completion.

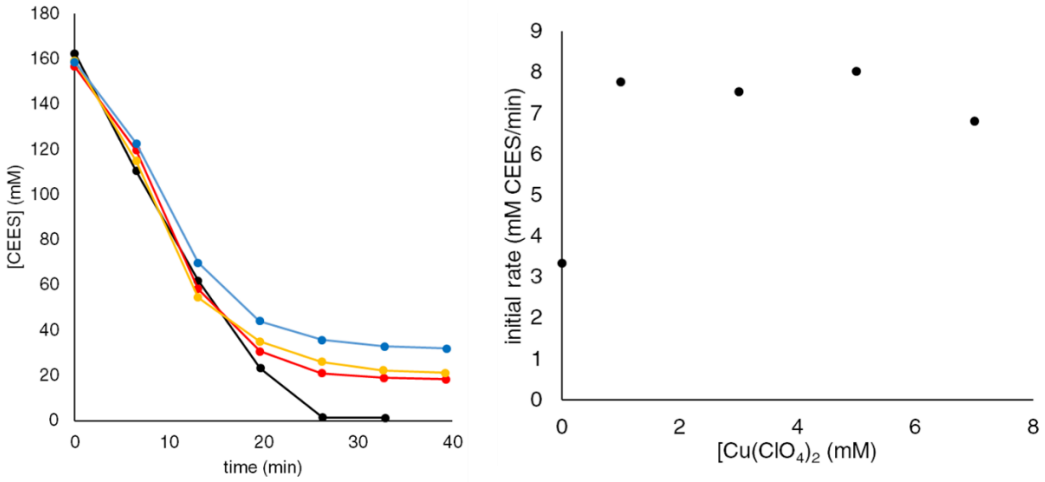

Figure 3.23. Effect of [Cu(II)] on sulfoxidation of CEES by Br_x/NO_x. [CEES] = 100 mM, [TBA-NO_3] = 50 mM, [TBA-Br_3] = 50 mM, [*p*-TsOH] = 10 mM, 2% H_2O in MeCN, 23 ºC, 1 atm air. [$Cu(ClO_4)_2$]: (●) 1mM, (●) 3mM, (●) 5mM, (●) 7mM.

This data suggests that Cu(II) may bind with CEES, resulting in product inhibition. CEES binding to copper is therefore likely not a reason behind the observed rate enhancement. One possibility is that formation of $CuBr_x$ species facilitates the reoxidation of Br^- to form Br_2. To test this, we performed reactions starting with Br- as the bromine source, with and without Cu(II) (Figure 3.24). There was no observable difference in rate between these two cases, suggesting that this is not responsible for the enhanced activity observed in the presence of Cu(II). The reason for the enhancement of activity by copper therefore remains undiscovered.

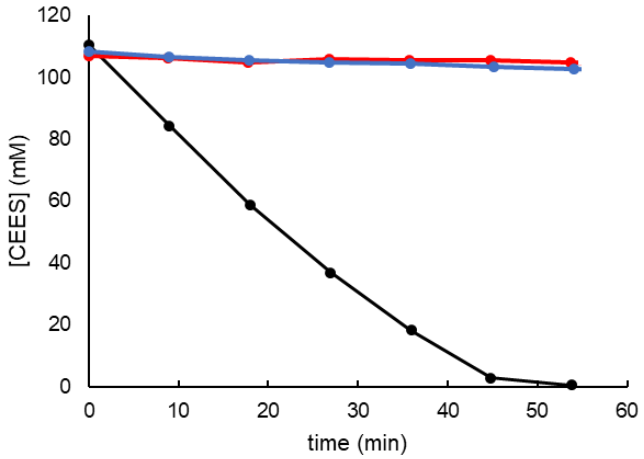

Figure 3.24. CEES sulfoxidation using Br^- with and without copper. [CEES] = 100 mM, [TBA-NO_3] = 2.5 mM, [*p*-TsOH] = 2 mM, 2% H_2O in MeCN, 23 ºC, 1 atm air. Br_x and Cu(II) conditions: (●) [TBA-Br] = 7.5 mM, [$CuClO_4)_2$] = 0.75 mM, (●) [TBA-Br] = 7.5 mM, [$CuClO_4)_2$] = 0 mM, (●) [TBA-Br_3] = 2.5 mM, [$CuClO_4)_2$] = 0 mM.

After establishing that Cu(II) increases the reaction rate, we then applied the optimized conditions to systems containing Cu(II) and demonstrated the substantial rate enhancement over the unoptimized Cu-free system (Figure 3.25).

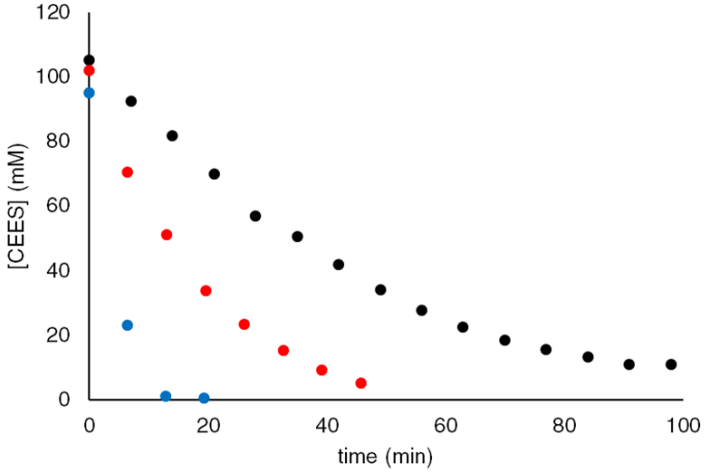

Figure 3.25. Optimized Br_x/NO_x sulfoxidation of CEES with Cu(II). [CEES] = 100 mM, 2% H_2O in MeCN, 23 ºC. Specific conditions: (●) [TBA-NO_3] = 5 mM, [TBA-Br_3] = 5 mM, 1 atm. air. (●) [TBA-NO_3] = 1.67 mM, [$Cu(NO_3)_2$] = 1.67 mM, [TBA-Br_3] = 3.33 mM, 1 atm. air. (●) [TBA-NO_3] = 1.67 mM, [$Cu(NO_3)_2$] = 1.67 mM, [TBA-Br_3] = 3.33 mM, 1 atm O_2.

To test whether product inhibition affected the reaction rate, another 20 equivalents of CEES were added after full oxidation of the first 20 equivalents (Figure 3.26). The reaction goes to completion, but at a slightly slower rate, suggesting that the sulfoxide product does slightly inhibit the reaction.

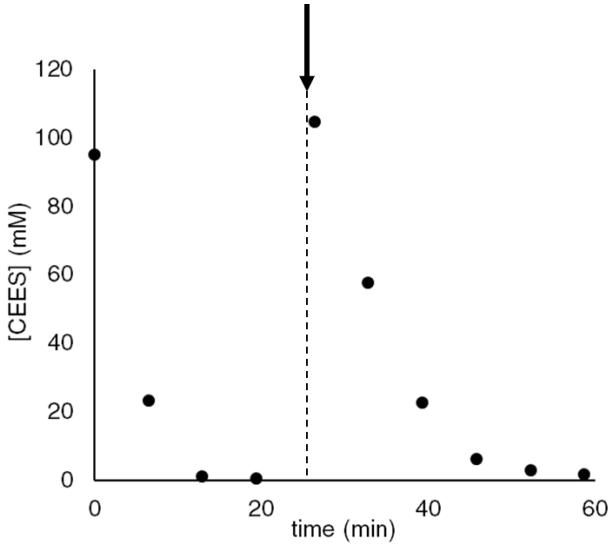

Figure 3.26. Reuse experiment for oxidation of CEES by Br_x/NO_x/Cu. [CEES] = 100 mM, [$Cu(NO_3)_2$] = 1.66 mM, [TBA-NO_3] = 1.67 mM, [TBA-Br_3] = 3.3 mM, [p-TsOH] = 10 mM, 2% H_2O in MeCN, 23 ºC, 1 atm O_2. Dotted line indicates point at which another 100 mM CEES was added to the solution.

As mentioned in section 3.1.1, selectivity for the sulfoxide product is especially important in this reaction to prevent formation of the toxic sulfone product. We therefore used ^{13}C NMR to examine the selectivity of the sulfoxidation reactions both with and without copper (Figure 3.27). The spectra taken after the oxidation reactions have been completed (as determined by GC) show no sulfide or sulfone product, confirming that the reaction is selective for the sulfoxide product.

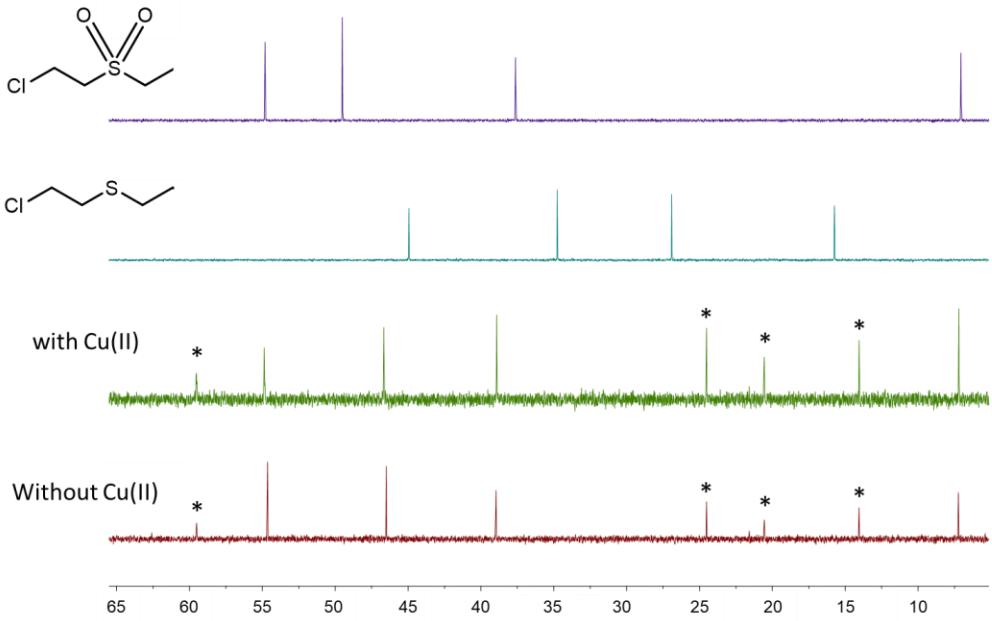

Figure 3.27. ^{13}C NMR of products of sulfoxidation reactions. Conditions for catalytic trials prior to NMR analysis: [CEES] = 100 mM, [TBA-NO_3] = 5 mM, [TBA-Br_3] = 5 mM, [p-TsOH] = 10 mM, 2% H_2O and 10% CD_3CN in MeCN, 23 ºC, 1 atm air. Reaction run with copper: [$Cu(ClO_4)_2$] = 1.5 mM. (*) = TBA counter cations.

To our knowledge, the fastest published system for selective aerobic sulfoxidation under mild conditions is a study that used pyridinium tribromide as the bromine source, and *tert*-butyl nitrite as the NO_x source.[41] We have reproduced this system using the optimized conditions we have developed, and demonstrate that the catalytic system with Cu(II) exhibits faster CEES decontamination rates, thus making it the fastest catalytic system for this reaction (Figure 3.28).

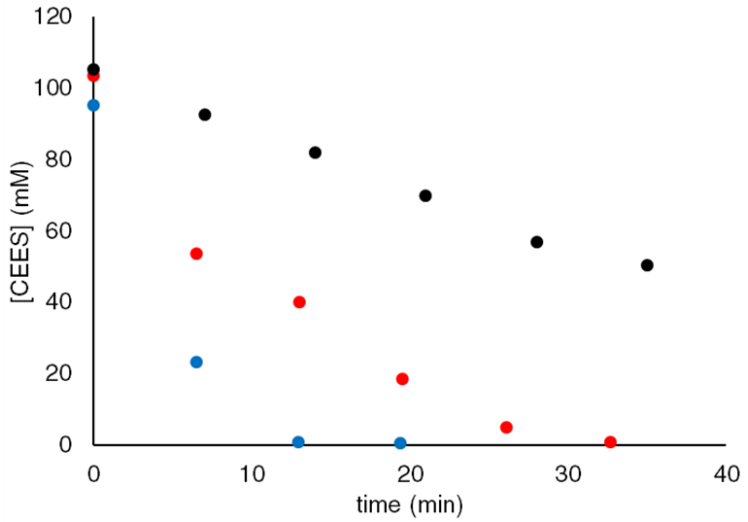

Figure 3.28. Comparison between the Br_x/NO_x system developed in this work and the one developed by Zhang et. al.[41] [CEES] = 100 mM, , 2% H_2O in MeCN, 23 ºC, 1 atm air. Specific conditions: (●) [TBA-NO_3] = 5 mM, [TBA-Br_3] = 5 mM, 1 atm. air. (●) [TBA-NO_3] = 1.67 mM, [$Cu(NO_3)_2$] = 1.67 mM, [TBA-Br_3] = 3.33 mM, [*p*-TsOH] = 10 mM,1 atm. O_2. (●) [*tert*-butyl nitrite] = 5 mM, [pyridinium tribromide] = 3.3 mM, [*p*-TsOH] = 10 mM, 1 atm. O_2.

3.3.5 Solid formulation

Reactive solids that can decontaminate upon contact are ideal for use in most environments and circumstances. Because of this, there is significant interest in the development of solid formulations of catalysts that can both sequester and decontaminate deleterious or undesirable compounds. We therefore aimed to produce a solid formulation of the catalytic system for aerobic oxidations described above. Several solid supports were tested first as dispersions in solution including MOFs and zeolites, but the presence of these solids inhibited or completely shut down the reaction. This was likely due to reactions between Br_3^- or Br_2 and the support materials themselves. However, success was achieved when using tetrafluoroethylene sulfonic acid polymer, Nafion, as a solid support. Previous experiments demonstrated that Nafion could be used instead of *p*-TsOH as the source of H^+ in the system (Figure 3.1). The solid formulation involved adding solutions containing TBA-Br_3 and $Cu(NO_3)_2$ to solid Nafion before drying, allowing the

catalytic components to disperse evenly. Neat CEES was then added to several reaction vials, and data points were taken by toluene extraction of the CEES at the specified times (Figure 3.29).

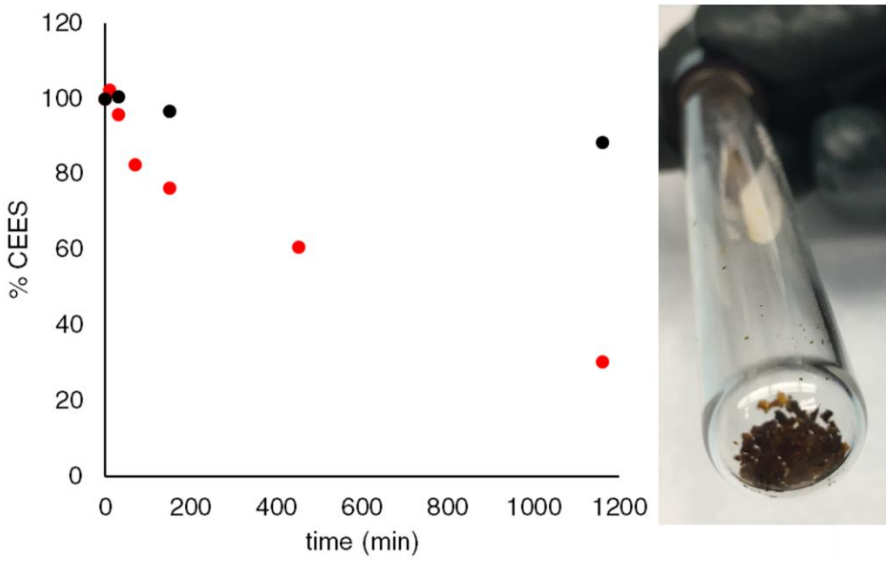

Figure 3.29. Solid formulation for aerobic sulfoxidation by the Br_x/NO_x/Cu(II) system. Each time point was taken from a separate reaction. In each vial, 20 µmol TBA-Br_3, 20 mg dry Nafion, and 215 µL of 50 mM $Cu(NO_3)_2$ (11 µmol) in MeCN was added to evenly disperse the catalytic components. Each vial was air dried for 12 hours and vacuum dried for 1 hour. To each vial, 50 µL CEES (430 µmol) was added to initiate the reaction. Reaction run under 1 atm. O_2. Control reaction was run on dry Nafion without addition of any reactive components. Image: picture of catalytic solid before CEES addition.

Though the solid reaction system requires significant optimization, this experiment demonstrates the potential for this system to be formulated as a solid that would indicate contact with HD through a color change and catalyze its decontamination. Current studies include the addition of the catalytic components to polymer systems that are known to form gels with HD, such as a fluorobenzene-based polymer developed by Wilson et. al.[62-63] If successful, this system would represent a significant advance in the field of reactive materials for sequestration, detection, and decontamination of toxic compounds.

3.4 Conclusions

The aerobic oxidation of sulfides catalyzed by Br_x and NO_x species is clearly extremely complex. This presents significant challenges towards developing a complete understanding of the reaction system, including elucidation of the full mechanism. Despite this, we have explored a variety of aspects of this reaction and have developed an extremely effective catalytic system. We have shown that the use of Br_3^- instead of Br^- as a bromine source leads to substantial acceleration of the reaction rate. Several parameters have been investigated, revealing the complex dependence of water and acid on the system and the more straightforward dependence on Br_3^- and NO_3^-. We have attempted to gain mechanistic insights through a variety of different methods including stopped-flow UV/vis spectroscopy to study individual reaction components and examining the reactivity of different sulfide species, but many of these results are challenging to interpret.

Adding Cu(II) to the reaction results in a significant acceleration of the rate, though the nature of this effect is unclear. Several insights have been obtained, such as inhibition of the reaction at elevated [Cu(II)] likely from binding of the sulfide, and results suggesting that copper is not directly involved in the reoxidation of Br^-. The copper reaction is particularly noticeable due to dramatic color change that detects both the presence of the sulfide and indicates when decontamination is complete. Both the copper-containing and copper-free systems are selective for the desired sulfoxide product, with no overoxidation products detected. This copper-containing aerobic oxidation system that operates under mild conditions is, to our knowledge, the fastest system of its kind. Solid formulations were made using the catalytic components embedded within the fluoropolymer, Nafion, resulting in a material that can decontaminate neat CEES upon contact. Further developments of the solid system and additional experiments to provide more mechanistic

insights are currently underway, and will lead to still more effective systems for decontamination of HD.

3.5 References

1. Luo, Z.; Geletii, Y. V.; Hillesheim, D. A.; Wang, Y.; Hill, C. L., *ACS Catalysis* **2011,** 1 (10), 1364-1370.

2. Carreno, M. C., *Chemical Reviews* **1995,** 95 (6), 1717-1760.

3. Fernández, I.; Khiar, N., *Chemical Reviews* **2003,** 103 (9), 3651-3706.

4. Kowalski, P.; Mitka, K.; Ossowska, K.; Kolarska, Z., *Tetrahedron* **2005,** 61 (8), 1933-1953.

5. Kaczorowska, K.; Kolarska, Z.; Mitka, K.; Kowalski, P., *Tetrahedron* **2005,** 61 (35), 8315-8327.

6. Mashkina, A. V., *Catalysis Reviews* **1990,** 32 (1-2), 105-161.

7. Uematsu, T.; Miyamoto, Y.; Ogasawara, Y.; Suzuki, K.; Yamaguchi, K.; Mizuno, N., *Catalysis Science & Technology* **2016,** 6 (1), 222-233.

8. Mata, E. G., *Phosphorus, Sulfur, and Silicon and the Related Elements* **1996,** 117 (1), 231-286.

9. Madesclaire, M., *Tetrahedron* **1986,** 42 (20), 5459-5495.

10. Guo, Z.; Liu, B.; Zhang, Q.; Deng, W.; Wang, Y.; Yang, Y., *Chemical Society Reviews* **2014,** 43 (10), 3480-3524.

11. Weinstock, I. A.; Schreiber, R. E.; Neumann, R., *Chemical Reviews* **2018,** 118 (5), 2680-2717.

12. Punniyamurthy, T.; Velusamy, S.; Iqbal, J., *Chemical Reviews* **2005,** 105 (6), 2329-2364.

13. Gunasekaran, N., *Advanced Synthesis & Catalysis* **2015,** 357 (9), 1990-2010.

14. Cavani, F.; Teles, J. H., *ChemSusChem* **2009,** 2 (6), 508-534.

15. Stahl, S. S.; Alsters, P. L., *Liquid Phase Aerobic Oxidation Catalysis : Industrial Applications and Academic Perspectives*. Wiley-VCH: Weinheim, Germany, 2016.

16. *Process Intensification for Green Chemistry*. John Wiley & Sons: 2013.

17. Anastas, P.; Eghbali, N., *Chemical Society Reviews* **2010,** 39 (1), 301-312.

18. Szinicz, L., *Toxicology* **2005,** 214 (3), 167-181.

19. Ghabili, K.; Agutter, P. S.; Ghanei, M.; Ansarin, K.; Panahi, Y.; Shoja, M. M., *Critical Reviews in Toxicology* **2011,** 41 (5), 384-403.

20. Smith, B. M., *Chemical Society Reviews* **2008,** 37 (3), 470-478.

21. Jang, Y. J.; Kim, K.; Tsay, O. G.; Atwood, D. A.; Churchill, D. G., *Chemical Reviews* **2015,** 115 (24), PR1-PR76.

22. Hiscock, J. R.; Bustone, G. P.; Clark, E. R., *ChemistryOpen* **2017,** 6 (4), 497-500.

23. Liu, Y.; Buru, C. T.; Howarth, A. J.; Mahle, J. J.; Buchanan, J. H.; DeCoste, J. B.; Hupp, J. T.; Farha, O. K., *Journal of Materials Chemistry A* **2016,** 4 (36), 13809-13813.

24. Wagner, G. W.; Yang, Y.-C., *Industrial & Engineering Chemistry Research* **2002,** 41 (8), 1925-1928.

25. Kumar, J. P.; P.V.R.K, R.; G.K, P.; Singh, B., *Applied Clay Science* **2015,** 116-117, 263-272.

26. Sullivan, K. P.; Neiwert, W. A.; Zeng, H.; Mehta, A. K.; Yin, Q.; Hillesheim, D. A.; Vivek, S.; Yin, P.; Collins-Wildman, D. L.; Weeks, E. R.; Liu, T.; Hill, C. L., *Chemical Communications* **2017,** 53 (83), 11480-11483.

27. Allen, S. E.; Walvoord, R. R.; Padilla-Salinas, R.; Kozlowski, M. C., *Chemical Reviews* **2013,** 113 (8), 6234-6458.

28. Bryliakov, K. P., *Chemical Reviews* **2017,** 117 (17), 11406-11459.

29. Zhang, X.; Rakesh, K. P.; Ravindar, L.; Qin, H.-L., *Green Chemistry* **2018,** 20 (21), 4790-4833.

30. Choudhary, K.; Suri, D.; Kothari, S.; Banerji, K. K., *Journal of Physical Organic Chemistry* **2000,** 13 (5), 283-292.

31. Shaabani, A.; Teimouri, M. B.; Safaei, H. R., *Synthetic Communications* **2000,** 30 (2), 265-271.

32. Ghorbani-Choghamarani, A.; Azadi, G.; Tahmasbi, B.; Hadizadeh-Hafshejani, M.; Abdi, Z., *Phosphorus, Sulfur, and Silicon and the Related Elements* **2014,** 189 (4), 433-439.

33. Kar, G.; Saikia, A. K.; Bora, U.; Dehury, S. K.; Chaudhuri, M. K., *Tetrahedron Letters* **2003,** 44 (24), 4503-4505.

34. Otokesh, S.; Kolvari, E.; Amoozadeh, A.; Koukabi, N., *RSC Advances* **2015,** 5 (66), 53749-53756.

35. Gogoi, P.; Hazarika, S.; Barman, P., *RSC Advances* **2015,** 5 (48), 38044-38047.

36. Iwasita, T.; Giordano, M. C., *Electrochimica Acta* **1969,** 14 (10), 1045-1059.

37. Allen, G. D.; Buzzeo, M. C.; Villagrán, C.; Hardacre, C.; Compton, R. G., *Journal of Electroanalytical Chemistry* **2005,** 575 (2), 311-320.

38. Le, N. H.; Han, Y.-h.; Ryu, S. G.; Cho, J., *Journal of Hazardous Materials* **2019,** 365, 511-518.

39. Zolfigol, M. A.; Amani, K.; Ghorbani-Choghamarani, A.; Hajjami, M.; Ayazi-Nasrabadi, R.; Jafari, S., *Catalysis Communications* **2008,** 9 (8), 1739-1744.

40. Zhang, H.; Chen, C.; Liu, R.; Xu, Q.; Zhao, W., *Molecules (Basel, Switzerland)* **2009,** 15 (1), 83-92.

41. Zhang, H.; Wang, G., *Tetrahedron Letters* **2014,** 55 (1), 56-58.

42. Lengyel, I.; Nagy, I.; Bazsa, G., *The Journal of Physical Chemistry* **1989,** 93 (7), 2801-2807.

43. Bosch, E.; Kochi, J. K., *The Journal of Organic Chemistry* **1995,** 60 (10), 3172-3183.

44. Kinen, C. O.; Rossi, L. I.; de Rossi, R. H., *The Journal of Organic Chemistry* **2009,** 74 (18), 7132-7139.

45. Martín, S. E.; Rossi, L. I., *Tetrahedron Letters* **2001,** 42 (41), 7147-7151.

46. Rossi, L. I.; Martín, S. E., *Applied Catalysis A: General* **2003,** 250 (2), 271-278.

47. Wang, T. X.; Kelley, M. D.; Cooper, J. N.; Beckwith, R. C.; Margerum, D. W., *Inorganic Chemistry* **1994,** 33 (25), 5872-5878.

48. Price, D.; Iddon, B.; International Conference on the, C.; Applications of, B.; Its, C., *Bromine compounds : chemistry and applications*. Elsevier: Amsterdam, 1988.

49. Bellucci, G.; Bianchini, R.; Chiappe, C., *The Journal of Organic Chemistry* **1991,** 56 (9), 3067-3073.

50. Beck, G. R. G. B. M. T., *International Journal of Chemical Kinetics* **1981,** 13 (12), 1277-1288.

51. Côrtes, C. E. S.; Faria, R. B., *Inorganic Chemistry* **2004,** 43 (4), 1395-1402.

52. Cox, B. G., *Organic Process Research & Development* **2015,** 19 (12), 1800-1808.

53. Partenheimer, W.; Fulton, J. L.; Sorensen, C. M.; Pham, V.-T.; Chen, Y., *Journal of Molecular Catalysis A: Chemical* **2014,** 387, 130-137.

54. Islam, S. M.; Roy, A. S.; Mondal, P.; Tuhina, K.; Mobarak, M.; Mondal, J., *Tetrahedron Letters* **2012,** 53 (2), 127-131.

55. Prasanth, K. L.; Maheswaran, H., *Journal of Molecular Catalysis A: Chemical* **2007,** 268 (1), 45-49.

56. O'Mahony, G. E.; Ford, A.; Maguire, A. R., *The Journal of Organic Chemistry* **2012,** 77 (7), 3288-3296.

57. Ren, C.; Fang, R.; Yu, X.; Wang, S., *Tetrahedron Letters* **2018,** 59 (11), 982-986.

58. McCann, S. D.; Stahl, S. S., *Accounts of Chemical Research* **2015,** 48 (6), 1756-1766.

59. Kim, M.; Weinstock, I. A.; Geletii, Y. V.; Hill, C. L., *ACS Catalysis* **2015,** 5 (12), 7048-7054.

60. Barnes, J. C.; Hume, D. N., *Inorganic Chemistry* **1963,** 2 (3), 444-448.

61. Olshin, P. K.; Myasnikova, O. S.; Kashina, M. V.; Gorbunov, A. O.; Bogachev, N. A.; Kompanets, V. O.; Chekalin, S. V.; Pulkin, S. A.;

Kochemirovsky, V. A.; Skripkin, M. Y.; Mereshchenko, A. S., *Chemical Physics* **2018,** 503, 14-19.

62. Wilson, C.; Main, M.; Cooper, N.; Briggs, M. E.; Cooper, A. I.; Adams, D., *Polymer Chemistry* **2017**.

63. Wright, A. J.; Main, M. J.; Cooper, N. J.; Blight, B. A.; Holder, S. J., *ACS Applied Materials & Interfaces* **2017,** 9 (37), 31335-31339.

Chapter 4: Speciation and Dynamics in the $Na_{10}[Co_4V_2W_{18}O_{68}]/Co(II)_{aq}/CoO_x$ Catalytic Water Oxidation System

4.1 Earth-Abundant Catalysts for Water Oxidation

As detailed in Chapter 1, the creation of inexpensive and active catalysts for generation of hydrogen fuel from sunlight is a central goal of green energy technologies. Advances in this field are imperative in order to meet the increasing high-energy-density needs as well as mitigate the effects of anthropogenic climate change.[1-2] Accordingly, the development of renewable energy systems has been called the greatest challenge for humanity in the 21st century.[3] A wide body of research has developed in recent years on this topic, with a variety of WOCs reported.[4-10] Many of the most active systems are based on expensive and scarce transition metals such as Rh, Ir, and Ru, which is prohibitive for large-scale use.[10] In order to reduce the costs, substantial effort has been expended to realize active WOCs based on earth-abundant metals.[10]

A variety of catalysts based on first-row transition metals have been developed due to their higher abundance in earth's crust. Many these use manganese, cobalt, nickel, and nickel-iron oxides as the catalysts.[11-12] In particular, cobalt oxide (CoO_x) water oxidation catalysts have been studied extensively. A study by Nocera et. al. reported high activity for water oxidation in neutral water under ambient conditions using amorphous cobalt phosphate.[13-14] In this system, Co(IV) is generated and is the active species in the reaction.[15] All known Co-based WOCs feature edge-sharing CoO_6 octahedra, with O-O bond formation occurring at the edges of the CoO_x clusters.[16] However, the activity of this process depends substantially on factors such as particle size or the identity of anions or cations present. Because of the challenge of carefully controlling and studying heterogeneous systems, homogeneous species such as POMs have been synthesized and used as tractable models of heterogeneous CoO_x systems.

4.1.1 Cobalt Polyoxometalate-Catalyzed Water Oxidation

POMs are useful in the formulation of molecular WOC because their modularity in design allows for small changes to be made to the POMs (such as control of cations, heteroatoms, or metal substitutions). Such systematic changes can then be studied to gain insights into mechanistic details of these reactions.[8] POMs do not contain organic ligands and therefore are not susceptible to ligand degradation under water oxidation conditions. As introduced in Chapter 1, several Co-based POMs have been developed which efficiently catalyze water oxidation.[10] The most common are of the general form $[M_4X_2W_{18}O_{68}]^{10-}$ (M = Zn, Ni, Mn, Cu, Co, Fe, X = Si, P, V, Al) consisting of a four-transition-metal "belt" arranged between two trilacunary Keggin POMs (Figure 4.1).

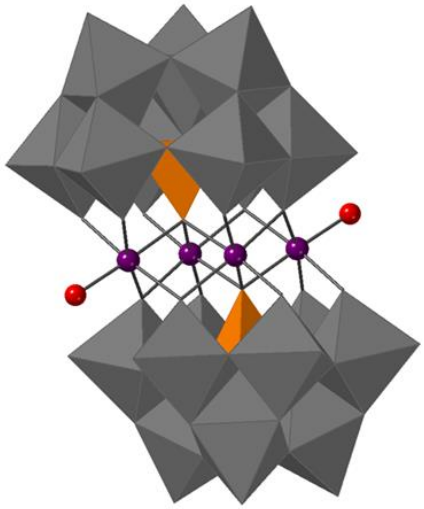

Figure 4.1. Representation of the $[M_4X_2W_{18}O_{68}]^{10-}$ POM unit.

The first Co-based POM shown to be a WOC was $[Co_4P_2W_{18}O_{68}]^{10-}$(**$Co_4P_2$**) and was reported by Yin et. al. from the Hill lab.[17] This all-inorganic POM has a TOF of ~6 mol O_2 $catalyst^{-1}$ s^{-1} for the WOC reaction. The "belt" of this POM resembles a monolayer of CoO_x, and the presence of PO_4^{3-} units immediately adjacent mimics the structure of the amorphous CoP_i-based catalysts studied by Nocera et. al. Since this initial publication, other Co-based POMs have been developed, including

$[Co_9(H_2O)_6(OH)_3(HPO_4)_2(PW_9O_{34})_3]^{16-}$ (**Co_9**).[18] A further notable publication is a paper by Lv. et. al. from the Hill lab, who reported a POM WOC wherein the P heteroatom was replaced by V, making $Na_{10}[Co_4(H_2O)_2(VW_9O_{34})_2]\cdot 35H_2O$ (**Co_4V_2**). This POM was reported to have a TON of ~1000 mol O_2 catalyst^{-1} s^{-1}.[19] Several characterization methods were used to confirm the stability of the POM in solution, such as FT-IR and UV/Vis spectroscopy, as well as ^{51}V NMR which attributed a peak at -507 ppm to the V heteroatom in **Co_4V_2**. UV/Vis spectroscopy measurements taken over extended timescales indicated few changes over time. Further DFT studies suggested that the increased speed of this catalyst was due to coupling of the d orbitals of V and Co atoms in **Co_4V_2**, which increases the oxidation potential of the Co centers.[20] There has been much recent work on related systems including in the Hill lab with the current development of mixed-metal POMs containing both Co and Ni in the "belt" structure. However, despite these promising advances in Co-POM WOCs, there have been concerns about the stability of these catalysts in solution, and their potential to act as pre-catalysts by releasing $Co(II)_{aq}$ ions into solution which can be oxidized, leading to CoO_x nanoparticles which are then responsible for the observed WOC activity. The following chapter addresses this discussion.

4.1.2 Stability of Polyoxometalate Water Oxidation Catalysts

POM solutions exhibit complex equilibria with hydrated metal ions and metal oxide particles in aqueous conditions.[21] Because of this, there have often been debates regarding the identity of the active WOC species under catalytic conditions.[22-28] The first discussion of the stability of **Co_4P_2** was published by Finke et. al.[29] In this publication, the authors claim that the activity observed in the **Co_4P_2** WOC system can be attributed solely to the presence of CoO_x species that are formed *in situ*. They support this claim using electrochemical measurements in which they observe the

oxidation wave increasing 10-fold in magnitude and shifting to lower onset potentials, suggesting that the initial material in solution is converting to a more active catalytic species over time. They also performed elemental analysis on films deposited on the electrode surface during the measurements and found that no W was present, suggesting that CoO_x species, not POMs, were deposited on the electrode and were responsible for the observed WOC activity. A subsequent publication by Finke et. al. using higher potential conditions with lower **Co_4P_2** concentrations was not able to distinguish between CoO_x and **Co_4P_2** as the active WOC.[30] Furthermore, Bonchio et. al. studied **Co_4P_2** using flash photolysis, and suggested that the catalyst was neither CoO_x nor **Co_4P_2**.[31] These studies all examined **Co_4P_2** under different conditions and obtained results that were not consistent with one another. To address this, a paper examining the stability of **Co_4P_2** was published by Vickers et. al. from the Hill group.[32] This work describes several experiments that confirm that the observed activity in the **Co_4P_2** system is due to the POM and cannot be explained simply by CoO_x species. Cathodic adsorptive stripping voltammetry was used to determine that the concentration of $Co(II)_{aq}$ ions in solution was very low even after aging **Co_4P_2** for several hours under conditions used for WOC reactions. Furthermore, tetraheptylammonium nitrate (THpA-NO_3) dissolved in toluene was used to selectively extract the POM from aqueous solution after aging. This extraction was followed by WOC measurements and revealed very low WOC activity in the aqueous layer, confirming that CoO_x (which would remain in the aqueous layer) is not responsible for the WOC activity in this system. ICP-MS of the aqueous solution after extraction confirmed that there was a very low concentration of Co in the aqueous layer. These studies conclusively confirmed that **Co_4P_2**, and not CoO_x, is the active WOC under the specific conditions outlined in the paper.

After this issue was concluded, two new papers by Finke et. al. were published questioning the solution stability of the **Co$_4$V$_2$** POM. The first established some of the hydrolytic features of this **Co$_4$V$_2$**-based system, identifying errors in the ^{51}V NMR peak assignments.[33] In this study, the authors report difficulties in obtaining a pure product based on the synthetic method provided, and confirm that the ^{51}V NMR signal attributed to **Co$_4$V$_2$** from the original report by Lv et. al. is in fact that of the POM $V_2W_4O_{19}^{4-}$ (V_2W_4), a product of **Co$_4$V$_2$** decomposition. The authors then use this to suggest that there is no **Co$_4$V$_2$** present in solution, and that the observed WOC activity is due to CoO_x species formed from decomposition of the POM. The second report by Finke et. al. on **Co$_4$V$_2$** examined the stability of the POM under water oxidation conditions.[34] In this paper, the authors used cathodic adsorptive stripping voltammetry and ^{31}P NMR line broadening analysis to determine [Co(II)$_{aq}$] in solution under different conditions. Additionally, various techniques were used to confirm that under the conditions they used, CoOx films were deposited on the electrode surface during WOC experiments, suggesting that activity was attributed exclusively to CoO_x formed as a result of POM decomposition.

To address concerns raised in these publications, and to add further insight into the behavior of these systems, a recent publication from the Hill lab has further investigated the stability in solution of **Co$_4$V$_2$** and has reported experimental data on its stability and activity.[35] This work provides an account of some of the challenges associated with the synthesis of **Co$_4$V$_2$**, examines its solution-state purity and speciation, and reveals updated ^{51}V NMR assignments of **Co$_4$V$_2$**. The study also examines the early-time kinetics of **Co$_4$V$_2$**, Co(II)$_{aq}$, and other species in the system, allowing for a more comprehensive characterization of these complex POM solutions. The remainder of the chapter outlines these studies.

4.2 Experimental

4.2.1 General Methods

General considerations. Materials, reagents and solvents were purchased from commercial sources in the highest purity available and used without further purification unless otherwise noted. Infrared spectra were recorded on a Nicolet 6700 FT-IR with Smart Orbit Diamond ATR accessory. UV-Vis spectra were measured using an Agilent 8453 diode-array spectrophotometer equipped with an Agilent 8909A Peltier temperature-control unit. For studies of *cis*-$[V_2W_4O_{19}]^{4-}$ and $[VW_5O_{19}]^{3-}$, the compounds $K_4V_2W_4O_{19} \cdot 8H_2O$ and $TMA_3[VW_5O_{19}]$ were prepared according to literature procedures.[36]

4.2.2 Synthesis of POMs

Synthesis of $Na_{10}[Co_4(H_2O)_2(VW_9O_{34})_2] \cdot 26\ H_2O$. The sodium salt of **$Co_4V_2$** was prepared by modifications of the literature procedure.[37] In a 150 mL beaker, $Na_2WO_4 \cdot 2\ H_2O$ (2.97g, 9 mmol) and V_2O_5 (91 mg, 0.5 mmol) were dissolved with stirring in 50 mL of NaOAc buffer (1.0 M, pH 4.8) at 70−80 °C to yield a slightly turbid brownish yellow solution. The solution may be filtered at this point, however, we found that it did not significantly affect the yield versus filtration at a later stage. To the stirring heated solution was added $Co(OAc)_2 \cdot 4\ H_2O$ (498 mg, 2 mmol), and immediately the solution became deep brown. The stirred solution was maintained at 75 °C for minutes uncovered, until the solution was concentrated to approximately half the original volume (~40-60 minutes). The solution was filtered while hot over a medium-porosity fritted glass funnel. We observed that the use of a coarse-porosity funnel did not sufficiently trap the fine solid. Within minutes upon cooling to room temperature, dark brown crystals began to form. The solution was

allowed to cool to room temperature before ~5mL EtOH was added dropwise over several minutes without stirring (to avoid the crystals turning a fine powder that is difficult to collect.) The crystals were grown for 24 – 72 hours and then collected on a coarse-porosity fritted glass funnel with aspiration and the brown crystals were washed gently with EtOH. The material was dried with aspiration for ~30 minutes until it could be transferred to dry overnight on a piece of filter paper to afford the compound in 46-58% yield based on W. Some additional details: addition of 1 g of NaOAc increased the yield to 66-70%, however, additional purification was required to remove acetate; IR was used to verify that excess acetate had been removed. In cases where acetate was still present (indicated primarily by the presence of strong bands at 1413 and 1563 cm^{-1} and medium bands at 1640 and 1690 cm^{-1}) washing the material with EtOH again was effective although this tended to turn the crystalline material into a fine powder. Isolation of the target POM from solution in a timely fashion is important. After 72 hours, isolated yields did not increase and ^{51}V NMR revealed an increased proportion of side-products present in the bulk material.

Synthesis of $TBA_6H_4[Co_4V_2W_{18}O_{68}]$ (TBA-Co_4V_2). The TBA salt of **Co_4V_2** was prepared *via* the method used to prepare the $TBA_6H_4[Co_4(H_2O)_2(PW_9O_{34})_2]$ (**TBA-Co_4P_2)** analogue,[38] which was based on modifications of literature procedures as follows.[39-40] An aqueous solution of 537 mg of $Na_{10}[Co_4(H_2O)_2(VW_9O_{34})_2] \cdot 26H_2O$ (0.1 mmol in 20 mL) was extracted with three 10-mL portions of a solution of tetrabutylammonium bromide in 1,2-dichloroethane (1.5 g in 30 mL). Some brown precipitate formed, which largely redissolved upon stirring of the biphasic mixture. The organic extracts were combined, filtered with suction, and washed with three 5-mL portions of water. The solution was layered with diethyl ether and dark brown crystals formed over 2-3 days. When allowed to stand in solution over long periods of time, the dark brown crystals of

TBA-Co_4V_2 separated from a dark green supernatant. Attempts to isolate solid crystalline product from this solution were largely unsuccessful, however, a combination of UV-Vis and preliminary X-ray diffraction suggest the solution contains $CoBr_4^{2-}$ and *cis*-$V_2W_4O_{19}^{3-}$ anions with TBA cations. This phenomenon is not observed with **TBA-Co_4P_2**, suggesting that Br^- anions may accelerate decomposition of **TBA-Co_4V_2** in solution. Thus, the timely isolation of the crystals is important to ensure high yield and purity when Br^- is present, and a different anion may be more suitable for the extraction procedure. The crystals were washed with water and dried, affording 358 mg of the title compound in 58% yield.

4.2.3 Experimental Methods

NMR spectroscopy. All ^{51}V NMR spectra were collected using a Bruker Ascend™ 600 MHz NMR instrument. Spectra were collected from 600 to -600 ppm with 512 scans, 0.5 s relaxation delay, 10 µs pulse width, and 0.08 s acquisition time. It was challenging to properly phase the spectra due to the large spectral window used in the experiment. Because of this, all spectra were manually phase corrected using the MestreNova software. Whittaker smoothing was used for baseline correction, with manual input assuring that the line fitting had minimal effect on the peak integration. Line widths and peak integrations were determined using the MestreNova software.

For initial NMR studies, solutions were composed of 90% H_2O and 10% D_2O for aqueous conditions and 100% CD_3CN for organic conditions. For the spectra taken in sodium borate buffer (240 mM, pH 8.26), a coaxial insert containing 100% D_2O was used instead of adding D_2O to the solution, so that the pH could be more accurately measured. For these kinetic measurements, the timer was started immediately upon dissolution of the solid powder by the liquid. These solutions

were all mixed by swirling for 5 minutes before being put into the NMR tubes and subsequent placement into the instrument. The time points recorded for each spectrum are the time that the acquisition was started (the total acquisition time is ~5 minutes), thus each time point represents the average of the spectra taken over that time.

For initial kinetics NMR studies using an internal standard, a coaxial NMR tube containing $VOCl_3$ dissolved in C_6D_6 was used as both the external standard and as the deuterated sample for locking. This facilitated control of the pH for the sample and provided an external reference. However, because of the volatile and moisture-sensitive nature of $VOCl_3$, we could not easily control the concentration of $VOCl_3$ in the C_6D_6 standard, and had to remake the standard for each new set of experiments due to concerns about gradual $VOCl_3$ degradation. This made it challenging to compare data across multiple experiments done at different times. Because of this concern, we switched to using Na_3VO_4 in the coaxial NMR tube as the external standard instead; this allowed us to use the same standard for all subsequent experiments. For these trials, 10mM Na_3VO_4 in D_2O was used as the external reference, but all peaks are still chemical shift referenced relative to neat $VOCl_3$. The same procedures were used for these kinetic measurements as for the original standard trials.

Solid-state ^{51}V MAS NMR. Spectra were collected on a Bruker Avance 600 spectrometer using a 4mm HCN biosolids probe, with a solid-echo pulse sequence with rotor-synchronized 1.6 μs long $\pi/2$ pulses and a spectral width of 1.0 MHz. Peaks were referenced to $VOCl_3$.

TGA measurements. Thermogravimetric analyses were conducted on a STA 6000 thermal analyzer.

Stopped-flow kinetics. Kinetic curves were obtained by monitoring spectral changes during the reaction of **Co_4V_2** with $[Ru(bpy)_3](ClO_4)_3$ using a HI-TECH Scientific KinetAsyst SF-61sX2 sample-handling unit with a diode array spectrophotometer. One syringe was filled with **Co_4V_2** in buffered solution and the second syringe was filled with $[Ru(bpy)_3](ClO_4)_3$ in water. All solutions were freshly prepared before each experiment, with ~3 minutes between dissolution and the start of the experiment. The kinetics of consumption of $[Ru(bpy)_3]^{3+}$ under catalytic conditions, where $[[Ru(bpy)_3]^{3+}] >> [\mathbf{Co_4V_2}]$, were measured by the decrease in absorbance at λ_{max} = 670 nm (ε = 4.2 x 10^2 M^{-1} cm^{-1}). In the experiments to study the effect of **V_2W_4** on the kinetics of $[Ru(bpy)_3](ClO_4)_3$ reduction catalyzed by $Co(NO_3)_2$, $Na_2V_2W_4$ was added as a solid material to the stock solution of $Co(NO_3)_2$ in borate buffer, and the kinetic curves were recorded after the desired aging time of the stock solution.

XPS measurements. XPS measurements were performed using a Thermo K-Alpha XPS. A monochromated aluminum Kα source (1486.6 eV) was used for excitation of photoelectrons. The base pressure of the analysis chamber was around 10^{-7} Pa during collection. High resolution scans were performed over a pass energy of 50 eV at 0.1 eV energy steps. All measurements were done on dried powders of **Co_4V_2**. V2p was recorded along with O1s. Samples were standardized against V_2O_5 and VO_2 powder. All samples were vacuum dried using Schlenk line techniques before introduction into the XPS chamber. The Thermo K-Alpha flood gun was used for charge neutralization during all experiments. Binding energy measurements were referenced to

adventitious carbon C1s peak at 284.8 eV. Analysis of all spectra were done using CasaXPS software (version 2.3.18). Shirley backgrounds are used unless otherwise stated. A mixture of Gaussian and Lorentzian functions (GL(30)) was used to fit the high resolution peaks of W. No deconvolutions were done for the high resolution vanadium or cobalt XPS due to extremely low signal-to-noise ratio that is the result of relatively low concentration of these species and surface charging effects. Reasonable fits were achieved using symmetric lineshapes for W(VI)4f. Fitting constraints were applied in such a manner as to be chemically sensible. The spin-orbit separation for the W4f7/2 and the W4f5/2 were set to be 2.18 eV, and all peak FWHM were constrained to be the same. All $V2p_{1/2}$ peaks are extremely broad and are not easily fitted. Quantification of vanadium concentration is therefore done by quantifying the $V2p_{3/2}$ peak. Oxygen is taken in the same spectrum for baseline fitting purposes and was not deconvoluted due to extensive speciation. It is important to note that the ratio of the main metallic elements present changes from the crystalline form of the POM to the two different batches of aging precipitates. The ratios of elements obtained via XPS is as follows, crystalline: Co:V:W = 2.0 : 1.0 : 9.6; after one day: Co:V:W = 3.2 : 1.0 : 10.7; after one week: Co:V:W = 3.3 : 1.0 : 9.1.

Uv/Vis measurements. All UV-Vis spectra were acquired using an Agilent 8453 spectrophotometer equipped with a diode-array detector.

Tetra-*n*-heptylammonium extraction method. Tetra-*n*-heptylammonium nitrate (THPA-NO_3) was synthesized from the reaction of tetra-*n*-heptylammonium bromide (THPA-Br) with $AgNO_3$. An aqueous solution of $AgNO_3$ was added to a solution of THPA-Br in toluene. The resulting mixture was shaken vigorously, forming light yellow AgBr. The colorless organic layer was

filtered to remove AgBr precipitate, and dried to isolate THPA-NO_3. During the extraction, a 50 mM solution of THPA-NO_3 in toluene was added to the aqueous solution of **Co_4V_2** and vigorously shaken for 5 minutes before use in subsequent analyses.

^{31}P NMR line-broadening analysis of Co(II)$_{aq}$ concentration. For these studies, we employed a method as has been previously described for these systems.[34] All ^{31}P NMR measurements were conducted using a Bruker Ascend™ 600 MHz NMR. The spectral width was −64.9 to +64.9 ppm (26,272.6 Hz) with a 45° pulse angle, 1.000 s relaxation delay, and 0.624 s acquisition time.

Cathodic absorptive stripping voltammetry. A Bi-film electrode was first fabricated by electrodeposition of metallic bismuth onto a glassy carbon electrode (0.071 cm^2) in a plating solution containing 0.079 g of $Bi(NO_3)_3 \cdot 5H2O$ and 0.4342 g of LiBr in 10 mL of 1.0 N HCl. This was achieved by performing chronoamperometry at -0.26 V vs 1M KCl Ag/AgCl for 75 seconds, passing approximately 11 mC of charge. A standard calibration curve was then generated using known quantities of $Co(NO_3)_2$ and 400 µM DMG. The concentration of the aqueous cobalt species was then determined using adsorptive cathodic stripping voltammetry. After the THPA extraction of **Co_4V_2** is complete, the aqueous layer is sampled and diluted 1000-fold. The analytic solution also contains 400 µM DMG and 0.1 M sodium borate buffer (pH 8.3). Pre-concentration of Co-DMG onto the Bi working electrode was done by performing chronoamperometry at -1.3 V vs Ag/AgCl for 15 seconds while stirring. Stirring was then stopped and differential pulse voltammetry was conducted on the analytic solution. Scanning from -0.7 to -1.3 V at 0.004 V increments with 0.05 V amplitude, 0.1 s pulse width, 0.01 s sampling width, and 0.2 s pulse period.

This entire procedure is a modified version of the adsorptive cathodic stripping technique reported in literature.[34, 41]

X-ray crystallography. Single red prism-shaped crystals of **TBA-Co_4V_2** were grown by layering diethyl ether onto a concentrated solution of **TBA-Co_4V_2** in MeCN. A suitable single crystal ($0.42\times0.28\times0.18$ mm^3) was selected and mounted on a loop with paratone oil on an APEX2 Mo source diffractometer equipped with an Oxford Cryosystems low-temperature device, operating at T = 100(2) K. The absence of nitrile stretching bands in the IR spectrum (~2250 cm^{-1}) confirmed the loss of co-crystallized and coordinated MeCN upon drying and the crystal was coated and mounted quickly to avoid crystal decomposition due to loss of solvent of crystallization. Data were measured using ω scans of 0.5° per frame for 20.0 s using MoK_α radiation (fine-focus sealed X-ray tube, 45 kV, 35 mA). The total number of runs and images was based on the strategy calculation from the program APEX2 (Bruker). The maximum resolution that was achieved was Θ = 29.575°. The diffraction patterns were indexed using SAINT (Bruker, V8.37A) and the unit cells were refined using SAINT (Bruker, V8.37A) on 50248 reflections, 76 % of the observed reflections. Data reduction, scaling and absorption corrections were performed using SAINT (Bruker, V8.37A) and CrysAlisPro 1.171.38.41 (Rigaku Oxford Diffraction, 2015) with a spherical absorption correction using equivalent radius and absorption coefficient. Empirical absorption correction using spherical harmonics was implemented in SCALE3 ABSPACK scaling algorithm software. The final completeness is 99.70 out to 29.575° in Θ. The absorption coefficient μ of this material is 11.958 mm^{-1} at this wavelength (λ = 0.71073 Å) and the minimum and maximum transmissions are 0.00773 and 0.02831. The structure was solved and the space group $P2_1/n$ (# 14) determined by the ShelXT [42] structure solution program using the Intrinsic Phasing solution

method and by using Olex2 [43] as the graphical interface. The model was refined with version 2014/7 of ShelXL-2014/7 (Sheldrick, 2014) using Least Squares minimization. All non-hydrogen atoms were refined anisotropically. Hydrogen atom positions were calculated geometrically and refined using the riding model.

This structure is essentially isostructural to the recently-reported **TBA-Co_4P_2** analogue,[38] however, the **TBA-Co_4V_2** structure exhibits significantly more disorder than the P analogue. The alkyl chains of the TBA cations show some disorder that is typical of TBA while the anion is fully disordered into more than two components; all nine W atoms were split into only two components where the second component is ~5% occupied. Due to the significant disorder, the overall quality of the structure model is much lower for **TBA-Co_4V_2**. Additional challenges in the refinement which contribute to the differences in magnitude of the largest peak and deepest hole are presented by the volatility of the diethyl ether and acetonitrile solvents, which rapidly escape the crystal lattice upon removal of the crystals from solution.

CCDC 1540222 for **TBA-Co_4V_2** contains the supplementary crystallographic data. These data can be obtained free of charge via http://www.ccdc.cam.ac.uk/conts/retreiving.html, or from the Crystallographic Data Centre, 12 Union Road, Cambridge CB2 1EZ, UK.

4.3 Results and Discussion

4.3.1 Synthesis of Co_4V_2

Finke et. al. noted that the synthesis outlined in the initial publication on **Co_4V_2** by Wu *et. al.* does not produce **Co_4V_2** in its pure form.[33, 44] This original synthetic route employed a 3:2:9 atomic ratio of V:Co:W - three times the stoichiometry for vanadium in the target POM. Indeed, following this procedure results in the formation of primarily vanadium-containing Lindqvist ions such as *cis*-$[V_2W_4O_{19}]^{4-}$ (**V_2W_4**) and $[VW_5O_{19}]^{3-}$ (**VW_5**). Considering the large formation constant (K = 10^{57} at 25 °C) in 0.6 M NaCl for **V_2W_4**,[45] it is favorable for excess vanadium in solution to react with the available tungsten, shifting the equilibrium towards a mixture of **V_2W_4** and **VW_5**.[33] To mitigate this problem, the synthesis performed by Lv et. al. employed only a slight excess of vanadium.[46] This synthetic methodology has now been improved, and can be successfully reproduced with typical yields of 50 - 60%. These synthetic details are discussed in the corresponding methods section.

4.3.2 ^{51}V NMR Studies

The purity of samples is imperative for quantitative work, and while pure *solid* phases of POMs can be obtained through crystallization, the speciation of POMs in *solution* is defined by the relative ratios of equilibrated species. Vanadium (^{51}V) NMR is a useful spectroscopic technique for identifying and tracking V-containing species in solution, owing to the high sensitivity and natural abundance of the ^{51}V nucleus.[47] The publication by Lv et. al. identifying **Co_4V_2** as a WOC incorrectly attributed the observed ^{51}V NMR signal at -507 ppm to the POM, and erroneously used this to assess its solution stability. This peak was correctly shown to result from **V_2W_4** by Finke

et. al.[33] Upon reexamination of the ^{51}V NMR spectra, it was confirmed that both **V_2W_4** (δ = -510 ppm) and **VW_5** (δ = -526 ppm) are present after the bulk solid is dissolved in H_2O (resulting in a solution pH of 6.2) (Figure 4.2).

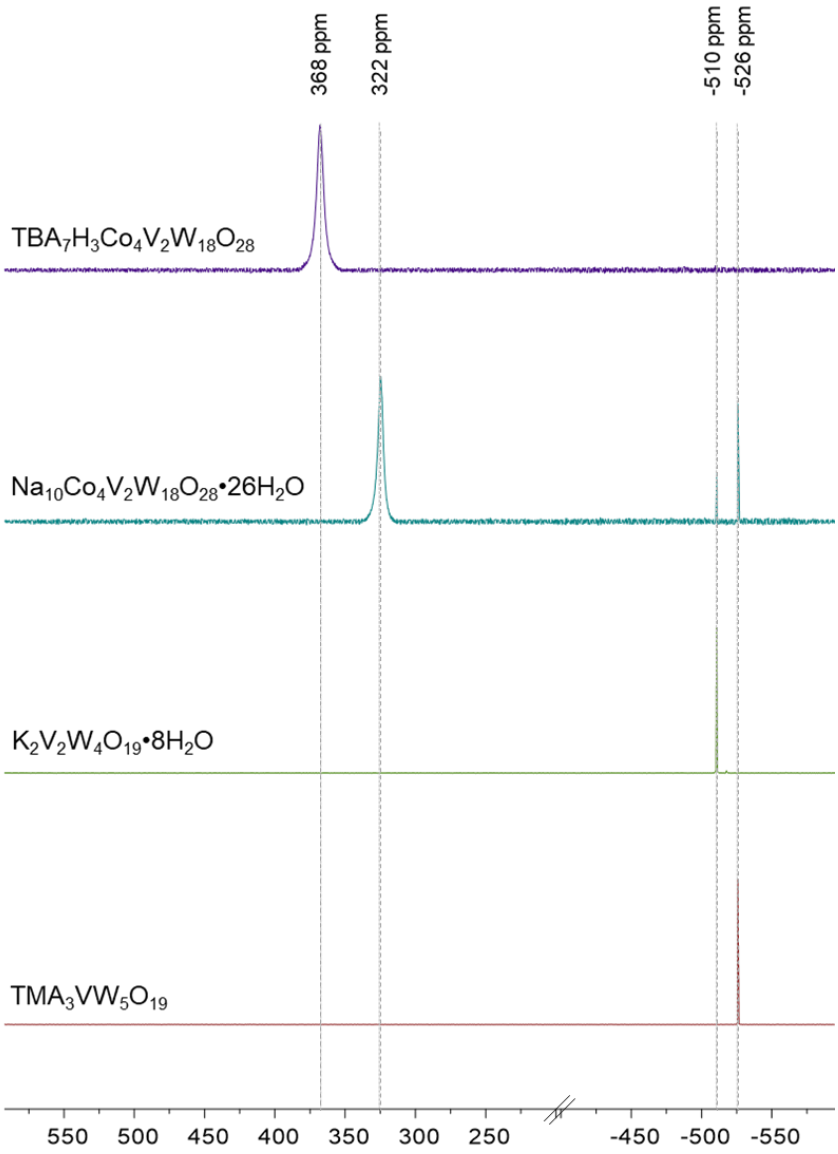

Figure 4.2. The ^{51}V NMR spectra of **Co_4V_2** and $[V_xW_{6-x}]^{(2+x)-}$ POMs (top to bottom); 5 mM **Co_4V_2** as TBA^+ salt in CD_3CN (purple) and as Na^+ salt in 10%D_2O/H_2O (green); 5 mM **V_2W_4** (yellow) and 5 mM **VW_5** in 10% D_2O/H_2O.

Vanadium nuclei located adjacent to the paramagnetic cobalt centers in **Co_4V_2** are expected to be significantly shifted and broadened relative to structurally similar, diamagnetic vanadium-containing species. [47-51] Therefore, upon revisiting ^{51}V NMR as a spectroscopic handle for **Co_4V_2**, the spectral window was expanded far beyond the expected region for vanadium-containing POMs (which are generally found between -500 and -600 ppm). This reveals a peak located at +320 ppm, which is substantially broadened and shifted relative to the diamagnetic **V_2W_4** and **VW_5** POMs (a chemical shift difference of greater than 800 ppm and more than an order of magnitude difference in linewidth (Table 4-1).

Table 4-1. Summary of ^{51}V NMR of compounds under investigation.

Species	Conditions	Chemical shift, δ (ppm)	Linewidth (Hz)
Na-Co_4V_2	10% D_2O/H_2O	320	680
Na-Co_4V_2	Solid state	400	N/A
TBA-Co_4V_2	CD_3CN	370	690
TBA-Co_4V_2	Solid state	420	N/A
V_2W_4	10% D_2O/H_2O	-510	22
VW_5	10% D_2O/H_2O	-526	15

The presence of this peak as the primary ^{51}V NMR signal after dissolution of crystalline **Co_4V_2**, as well as the significant chemical shift difference and line broadening relative to other vanadium-containing diamagnetic POMs suggests that the peak is that of **Co_4V_2** in solution. To support this assignment, the solid-state magic angle spinning ^{51}V NMR spectrum of a crystalline sample of **Co_4V_2** was obtained, revealing a peak centered at +405 ppm (Figure 4.3). This is shifted 85 ppm relative to the solution peak, but ^{51}V chemical shifts are known to deviate from solution chemical shift values due to several factors, including solvation effects.[52-54]

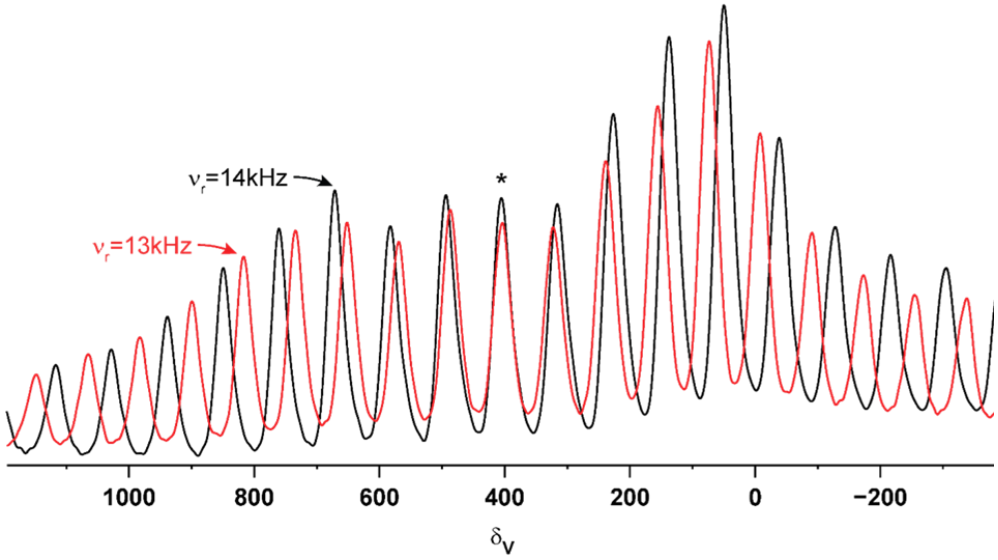

Figure 4.3. The solid-state ^{51}V NMR of **Co$_4$V$_2$**. ^{51}V NMR (157.9MHz) room temperature magic-angle spinning (MAS) NMR spectrum of **Co$_4$V$_2$** The two spinning speeds allow identification of the center band, indicated by (*).

To further support this assignment, the tetra-*n*-butylammonium (TBA) salt $TBA_6H_4[Co_4(H_2O)_2(VW_9O_{34})_2]$ (**TBA-Co$_4$V$_2$**) was synthesized (Figure 4.4).[38] This hydrophobic POM is soluble in MeCN where it is less susceptible to hydrolysis and speciation. The X-ray crystal structure of **TBA-Co$_4$V$_2$** is isostructural to the P congener $TBA_6H_4[Co_4(H_2O)_2(PW_9O_{34})_2]$ (**TBA-Co$_4$P$_2$**) the Hill group has reported;[38] both structures reveal MeCN coordination to the outside cobalt centers in the central belt of the polyanion.

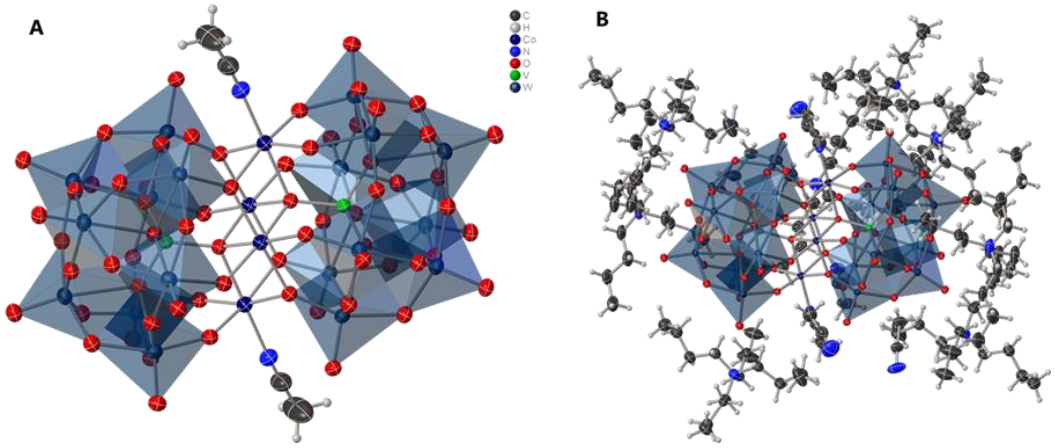

Figure 4.4. X-ray crystal structure of $TBA_6H_4[Co_4V_2W_{18}O_{68}]$. Thermal ellipsoids are shown at the 50% probability level. The TBA counterions and the co-crystallized solvent molecules are omitted for clarity.

The ^{51}V NMR spectrum of this compound reveals a single peak located at +370 ppm, with no signal observed for any hydrolytic breakdown products (Figures 4.2, 4.5). The chemical shift difference between the Na^+ and TBA^+ salts (50 ppm) is expected due to the difference in solvent, counterion, and substitution of H_2O for MeCN on the outside cobalt atoms.[55] The linewidth of the **TBA-Co_4V_2** peak in MeCN ($v_{1/2}$ = 690 Hz) is similar to that of the **Co_4V_2** peak in water ($v_{1/2}$ = 680 Hz), suggesting similarities in the paramagnetic environment of the vanadium atoms.

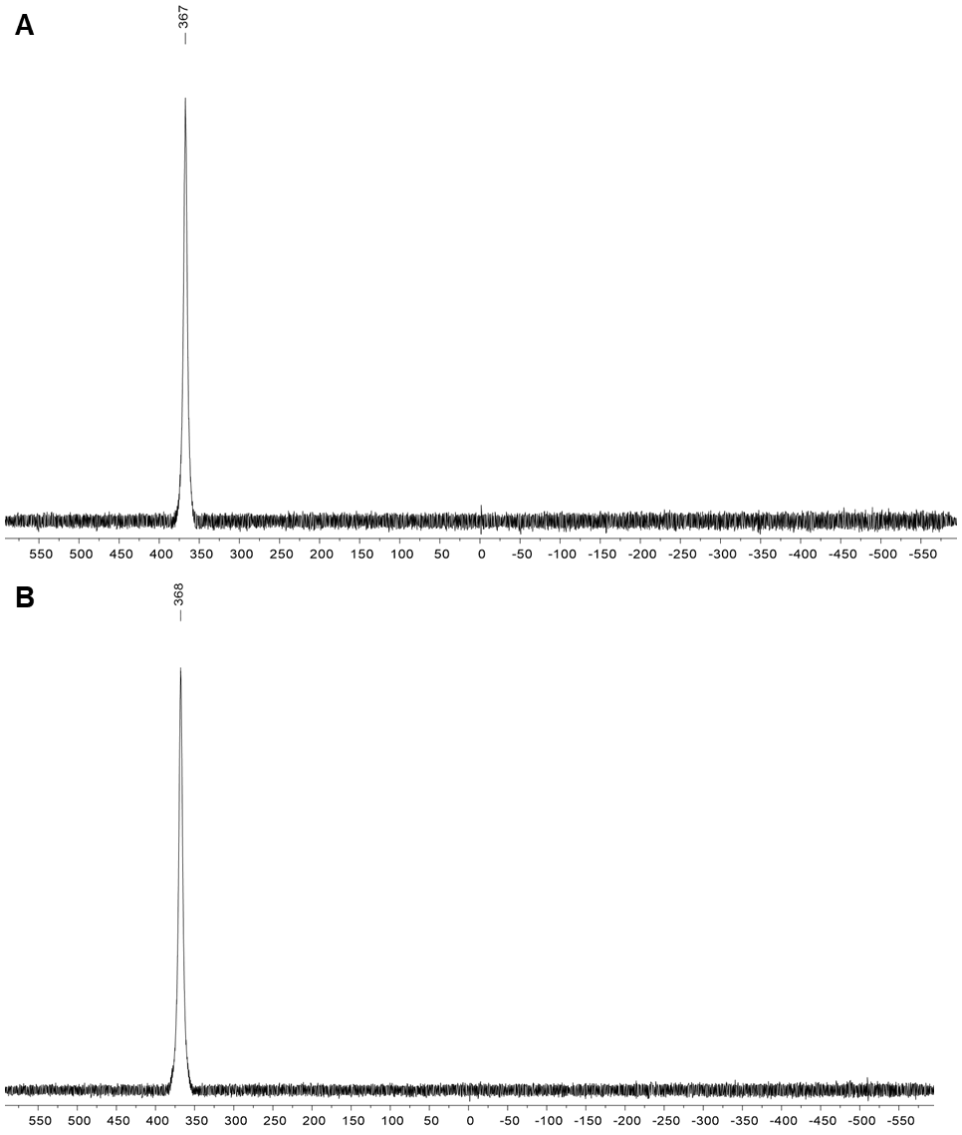

Figure 4.5. ^{51}V NMR of 5mM **TBA-Co_4V_2** in MeCN after 30 minutes and 50 days aging**.** (**A**) The ^{51}V NMR spectrum of **TBA-Co_4V_2** taken 30 minutes after dissolution in CD_3CN. (**B**) The ^{51}V NMR spectrum of **TBA-Co_4V_2** taken after aging 50 days in the same NMR tube at room temperature. Chemical shifts referenced to neat $VOCl_3$ (0 ppm).

The ^{51}V solid-state magic-angle spinning (MAS) NMR spectrum was obtained for **TBA-Co_4V_2** as well, revealing a peak centered at +420 ppm (Figure 4.6). This peak is shifted only 20 ppm relative to the Na^+ salt **Co_4V_2** ^{51}V MAS NMR signal (as opposed to a 50 ppm shift difference between the solution spectra), demonstrating that the interaction of solvent molecules is a significant factor in

the solution phase chemical shifts. The presence of this peak as the primary signal in the solution and solid-state NMR for the Na^+ salt, and the exclusive signal for the TBA^+ salt, strongly suggests that the observed ^{51}V NMR peaks are a result of **Co_4V_2** in solution. The use of ^{51}V as a spectroscopic handle to assess the stability of **Co_4V_2** is therefore established.

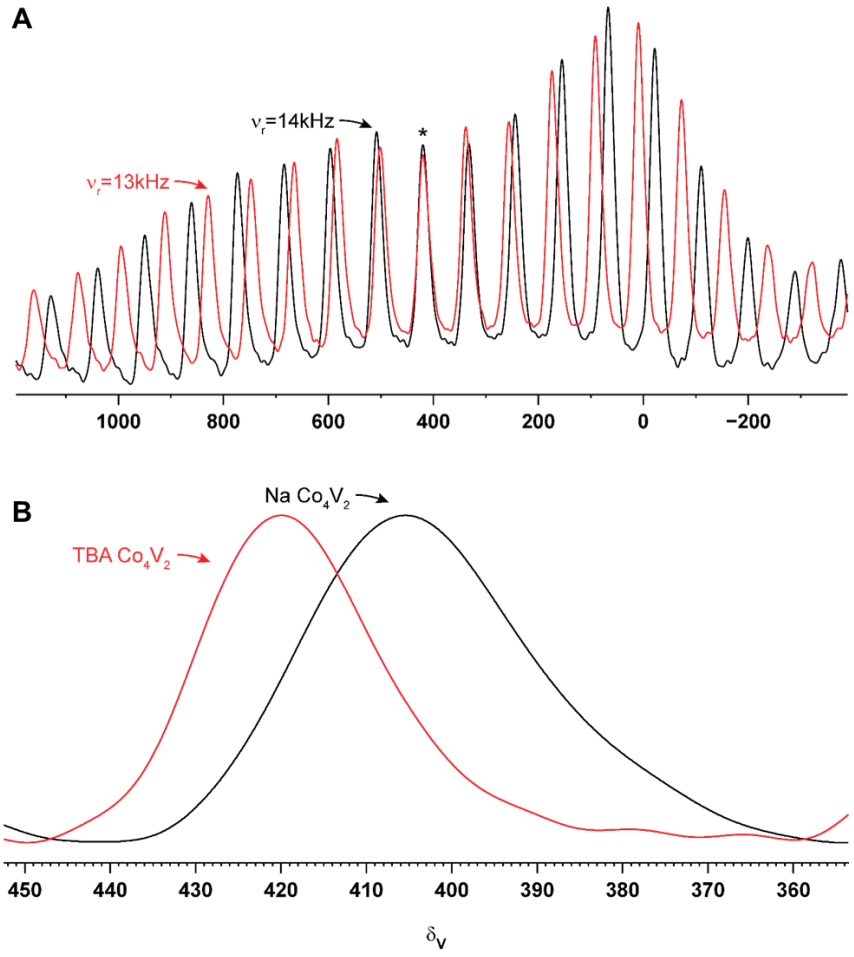

Figure 4.6. The solid-state ^{51}V NMR of **TBA-Co_4V_2**. (**A**) ^{51}V NMR (157.9MHz) room temperature magic-angle spinning (MAS) NMR spectrum of **TBA-Co_4V_2** at 14.1 T with a MAS rate of 13kHz (red) and 14kHz (black). The two spinning speeds allow identification of the center band, indicated with an "*" for the two species. (**B**) ^{51}V spectrum highlighting the center bands of **TBA-Co_4V_2** (red) at 420ppm and **Co_4V_2** (black) at 405ppm.

The discovery of this characteristic peak is significant, considering examples of ^{51}V spectra of paramagnetic molecules are exceedingly rare.[33] This spectroscopic handle allows for a more thorough investigation of the purity, stability, and solution behavior of **Co_4V_2**. The ^{51}V NMR spectrum of 5 mM **Co_4V_2** taken 30 minutes after dissolution in 10% D_2O/ H_2O reveals ~2% **V_2W_4** and **VW_5** relative to **Co_4V_2** (Figure 4.7). After aging 50 days at room temperature, signal integration for these side products increases to ~30% relative to **Co_4V_2** with the predominant side product being **V_2W_4**. Thus, though conversion to side products occurs over an extended timescale, **Co_4V_2** persists for many days when dissolved in water.

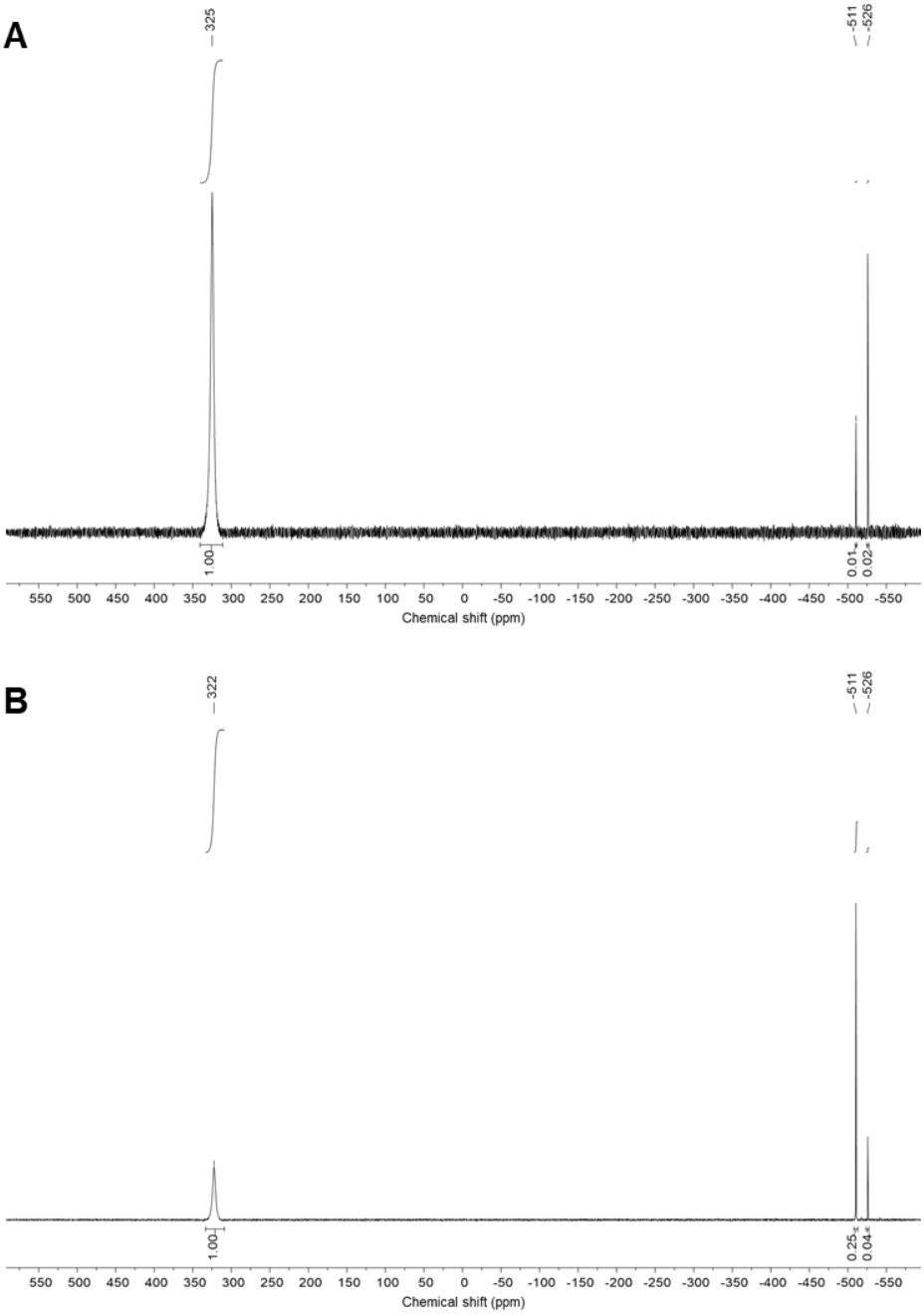

Figure 4.7. ^{51}V NMR of 5mM **Co_4V_2** in H_2O/10% D_2O after 30 minutes and 50 days aging**.** (**A**) The ^{51}V NMR spectrum of **Co_4V_2** taken 30 minutes after dissolution in neutral nanopure water. (**B**) The ^{51}V NMR spectrum of **Co_4V_2** taken after aging 50 days in the same NMR tube at room temperature. Chemical shifts referenced to neat $VOCl_3$ (0 ppm).

Water oxidation experiments are typically conducted in buffered solutions above pH 8.0. The stability of **Co_4V_2** under these conditions is therefore an issue of primary importance. To assess the stability in a more quantitative fashion, the **Co_4V_2** ^{51}V NMR signal was tracked over time after dissolution under a variety of conditions, referencing the observed peaks to an external standard inserted in a coaxial NMR tube (Figure 4.8).

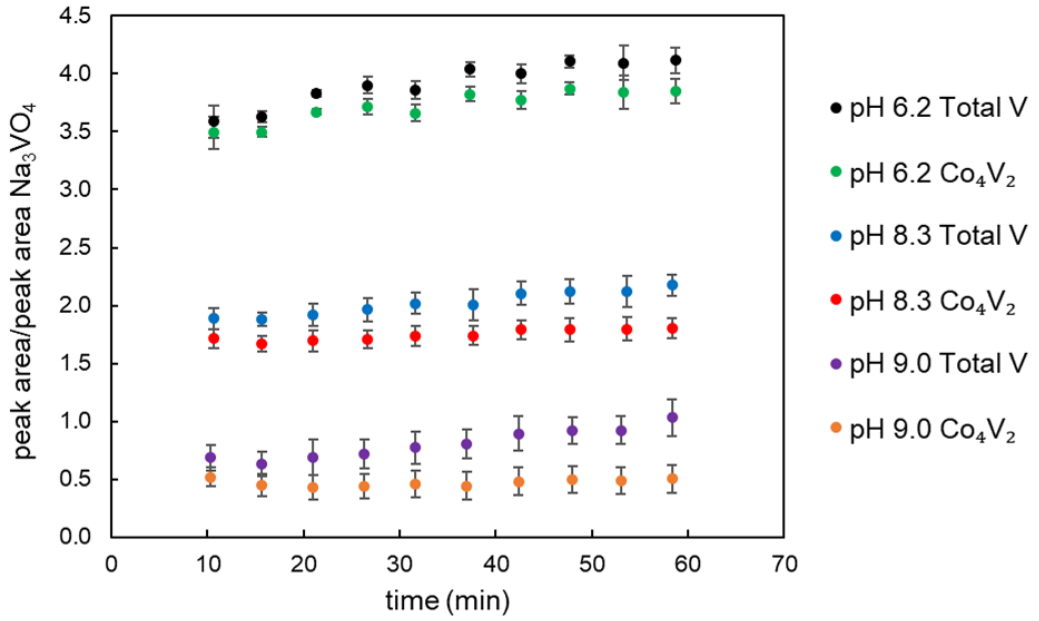

Figure 4.8. ^{51}V NMR kinetic profiles of **Co_4V_2** and total vanadium signal at varying pH. The time was started after addition of the liquid to the solid sample. The **Co_4V_2** peaks are referenced to an external standard of 10 mM Na_3VO_4 in D_2O in a coaxial NMR tube. Data at pH 6.2 represents **Co_4V_2** after addition to unbuffered nanopure H_2O, and data at pH 8.3 and 9.0 are both in 80mM NaB buffer. **Co_4V_2** solid added was calculated based on 5 mM resulting solution. Total V refers to the sum of all observed ^{51}V NMR signals in the spectra. Error bars are calculated from triplicate measurements.

Due to the very large chemical shift window used for these experiments, baseline smoothing techniques were required to obtain peak integration data. As a result, these measurements are semi-quantitative in nature and will be used to discuss general trends rather than quantitative results.

The ^{51}V NMR experiments reveal several significant findings, most notably the strong dependence of the **Co_4V_2** peak on the pH of the solution. The **Co_4V_2** signal changes little over a 1-hour timescale in all cases, but the initial peak area decreases substantially with increasing pH. This is not simply due to the conversion of **Co_4V_2** to species such as **V_2W_4**: when the total observable vanadium signal over this same timescale is plotted (comparing the sum of the ^{51}V NMR peaks relative to the external standard) the same trend is observed (Figure 4.9).

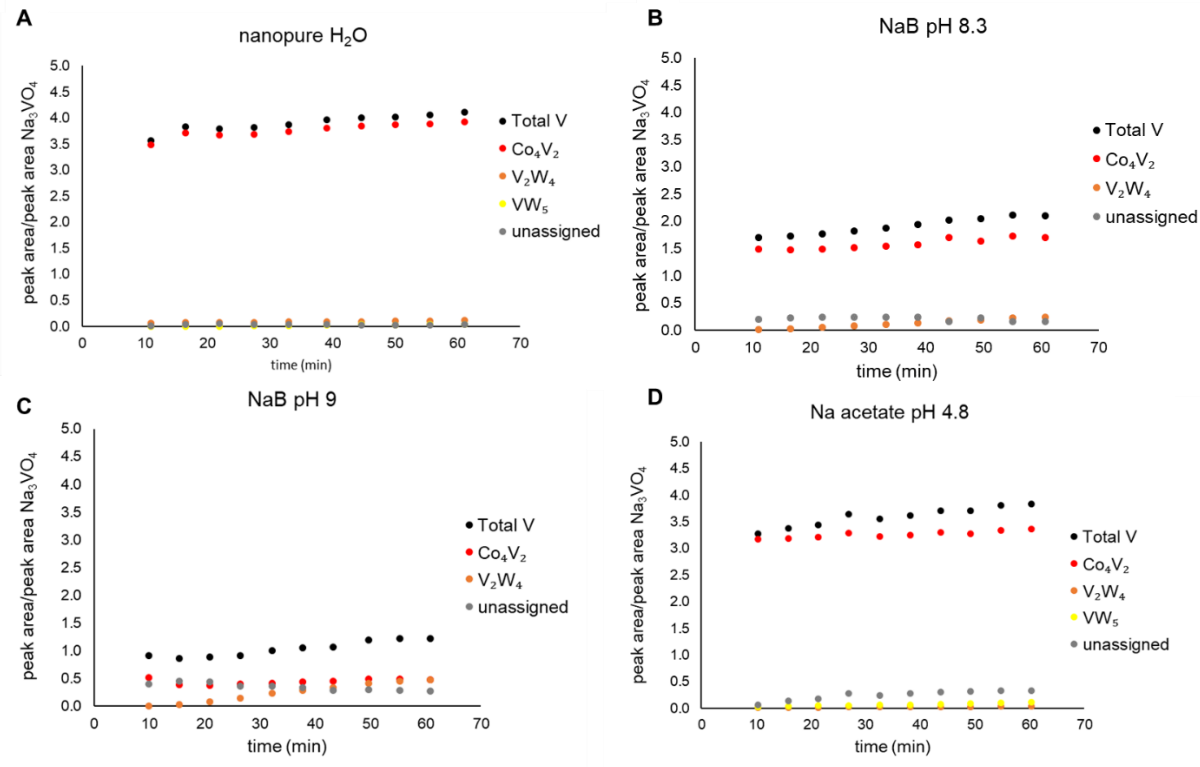

Figure 4.9. ^{51}V NMR signal kinetic measurements of **Co_4V_2** speciation for all species observed in the spectra under various conditions. Conditions were 5mM **Co_4V_2** in (**A**) nanopure water, (**B**) 80mM NaB buffer pH 8.3, (**C**) 80mM NaB buffer pH 9.0, (**D**) 80mM Na acetate buffer pH 4.8. Timer was started upon addition of the solution to the solid POM, and solution was stirred for 5 min to ensure complete dissolution before placement of the solution into the NMR tube and acquisition. A coaxial insert containing 10mM Na_3VO_4 in D_2O was used for locking and for peak area comparison. Various unidentified and unassigned peaks are summed together and labeled as "unassigned." Peaks are referenced to neat $VOCl_3$ at 0 ppm.

In all cases, **Co₄V₂** remains the major component of the total observed vanadium signal, but the total signal is substantially reduced as the pH is increased. Over the course of one hour, there is an increase in concentration of other vanadium-containing species (Figure 4.10). However, the **Co₄V₂** signal remains relatively constant and the observed vanadate peaks are not proportional to the amount of **Co₄V₂** signal missing. This suggests that at higher pH, a vanadium-containing species is formed that is not observed in the ^{51}V NMR spectrum, which then converts to the observed by-products over time.

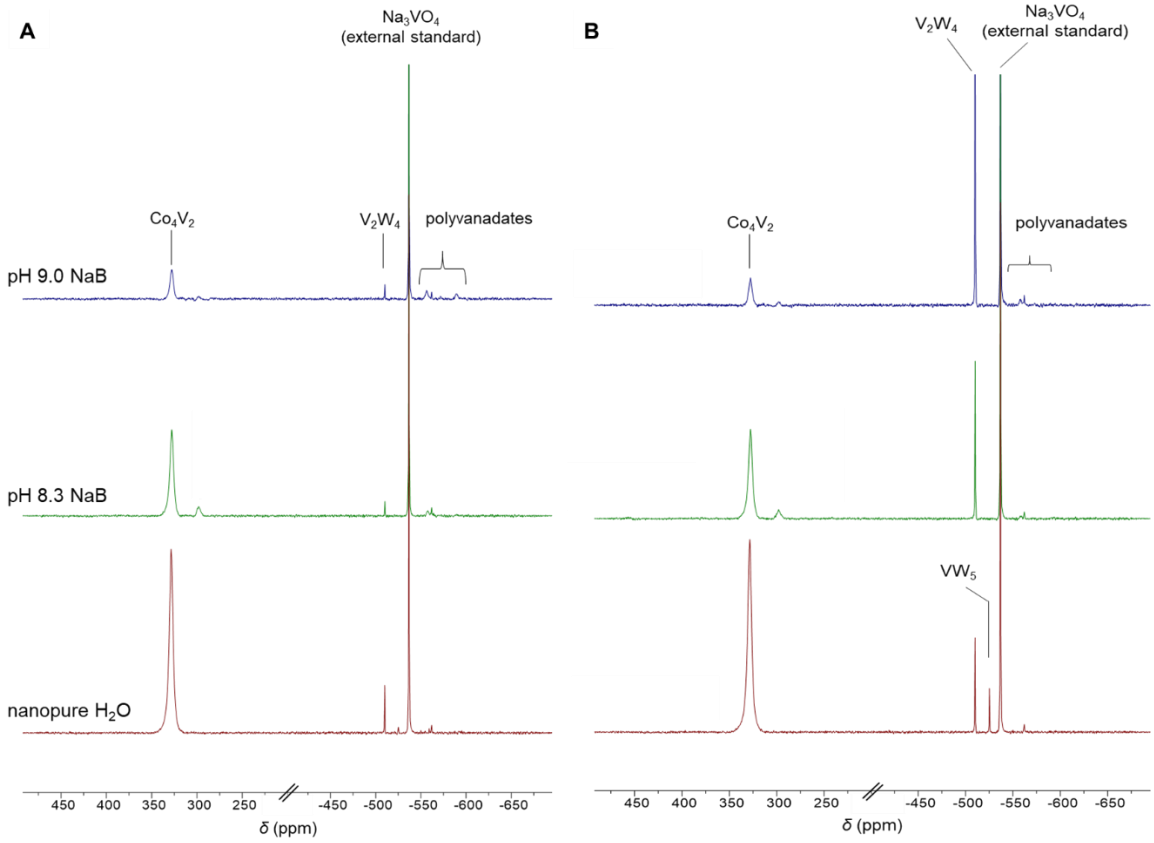

Figure 4.10. ^{51}V NMR spectra for **Co₄V₂** before (**A**) and after (**B**) 1-hour aging in different conditions. **Co₄V₂** solutions (5mM) in nanopure water, 80mM NaB buffer pH 8.3, or 80mM NaB buffer pH 9.0. Timer was started upon addition of the solution to the solid POM, and solution subsequently stirred for 5 min to ensure complete dissolution before placement of the solution into the NMR tube and acquisition. A coaxial insert containing 10mM Na_3VO_4 in D_2O was used for locking and for peak area comparison. Peaks are referenced to neat $VOCl_3$ at 0 ppm.

The equilibria of soluble metal oxides and hydroxides are quite complex and vary with many factors including pH, concentration, and ionic strength. This leads to the potential for many species to exist simultaneously in solution. Studies done on systems of molybdovanadates have revealed as many as 40 distinct equilibrated species.[56] In addition, these equilibria occur at different rates, with tungstate species generally exhibiting very slow equilibration.[57] The natural pH of a 5 mM solution of **Co_4V_2** is 6.2, and remains constant over the ~1-hour timescale typical for the NMR experiments. Adding equivalents of NaOH to a solution of **Co_4V_2** in neutral water reveals that the system is self-buffering, as the pH initially increases substantially after each addition before returning to an equilibrium value. The speciation was tracked by ^{51}V NMR after the addition of subsequent equivalents of NaOH, measuring both the NMR spectrum and pH after equilibration (Figure 4.11.).

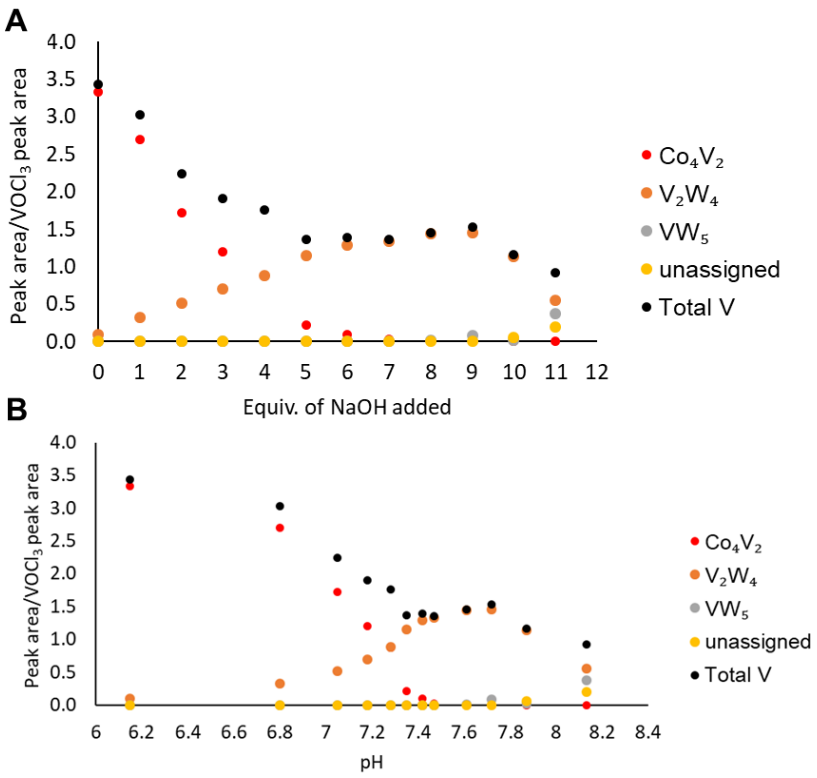

Figure 4.11. Titration studies of **Co₄V₂** observed by ^{51}V NMR. **Co₄V₂** was dissolved in nanopure water followed by equilibration for 30 minutes to obtain a stable pH. After the addition of each equivalent, the pH of the solution increased rapidly before falling slowly as the POM equilibrated. Because of this, 30 minutes was given for equilibration before the solution was used for NMR. A coaxial insert containing $VOCl_3$ in C_6D_6 was used for locking and for peak area comparison. Peaks are referenced to neat $VOCl_3$ at 0ppm. (**A**) shows the data relative to the number of equivalents of NaOH added, and (**B**) shows the same data but scaled to the pH of the solution after equilibration following the addition of NaOH.

These data show that adding equivalents of NaOH results in the decomposition of **Co₄V₂** and the formation of **V₂W₄**. This provides direct observation of the equilibrium behavior of **Co₄V₂** by changing the pH of the solution over time and observing the resulting ^{51}V NMR signal. A freshly prepared solution of **Co₄V₂** was dissolved in NaB buffer at pH 8.3 followed by nitric acid addition to decrease the pH, resulting in an increased signal for **Co₄V₂** (Figure 4.12). The pH was then increased by the addition of NaOH, which decreased the observed **Co₄V₂** signal, confirming that **Co₄V₂** is in equilibrium with other species that are not observed in the ^{51}V NMR spectrum.

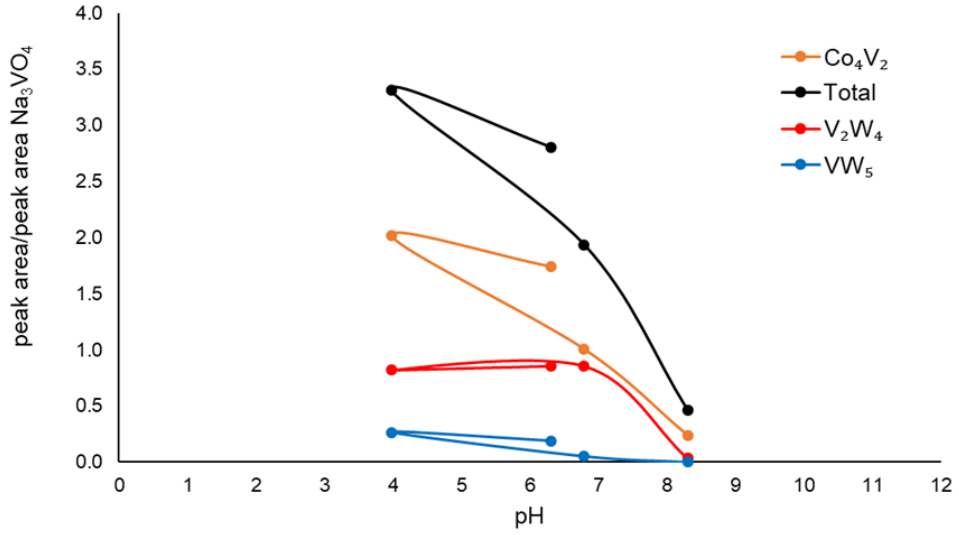

Figure 4.12. ^{51}V NMR study of pH equilibrium in **Co_4V_2** signal. **Co_4V_2** was dissolved in water for 5 min in 80mM NaB buffer at pH 8.3. A concentrated HNO_3 solution was added to decrease the pH to 6.8 and then to 4, followed by the addition of a concentrated NaOH solution to increase the pH to 6.3.

A significant observed effect in Figures 4.8 and 4.9 is the overall *increase* in the amount of both **Co_4V_2** and total vanadium signal over time. This is consistent with an equilibrium between the unobserved species, **Co_4V_2**, and the observed decomposition products, where dissolving **Co_4V_2** in a buffer at higher pH generates lower initial amounts of **Co_4V_2**, followed by a slow equilibration that results in the re-formation of some **Co_4V_2**.

4.3.3 Additional Speciation Characterization

There are three primary scenarios which could explain a decreased amount of total vanadium signal at elevated pH: a) reduction of V(V) to the paramagnetic V(IV); b) precipitation of **Co_4V_2** or a decomposition product to form a solid; or c) decomposition of the POM resulting formation of Co-containing species not observed by NMR. These scenarios are addressed in the following sections:

a) Reduction of V(V) to the paramagnetic V(IV).

V(IV) is a paramagnetic species and would not be observed by ^{51}V NMR. However, increasing the pH is unlikely to result in reduction of vanadate to vanadyl, as there is no species present in this system capable of reducing V(V). Additionally, XPS studies show that there is no V(IV) in samples of **Co_4V_2** that have been added to NaB buffer and subsequently dried and stored under argon before analysis (Figure 4.13). The peak shape of the Co2p peaks and their satellites shown in all three spectra are consistent with Co(II) being the predominant species. Deconvolution efforts are consistent with a single species of Co(II) present, and with only V(V) species present. The presence of V(IV), therefore, is very unlikely to account for the missing ^{51}V NMR signal.

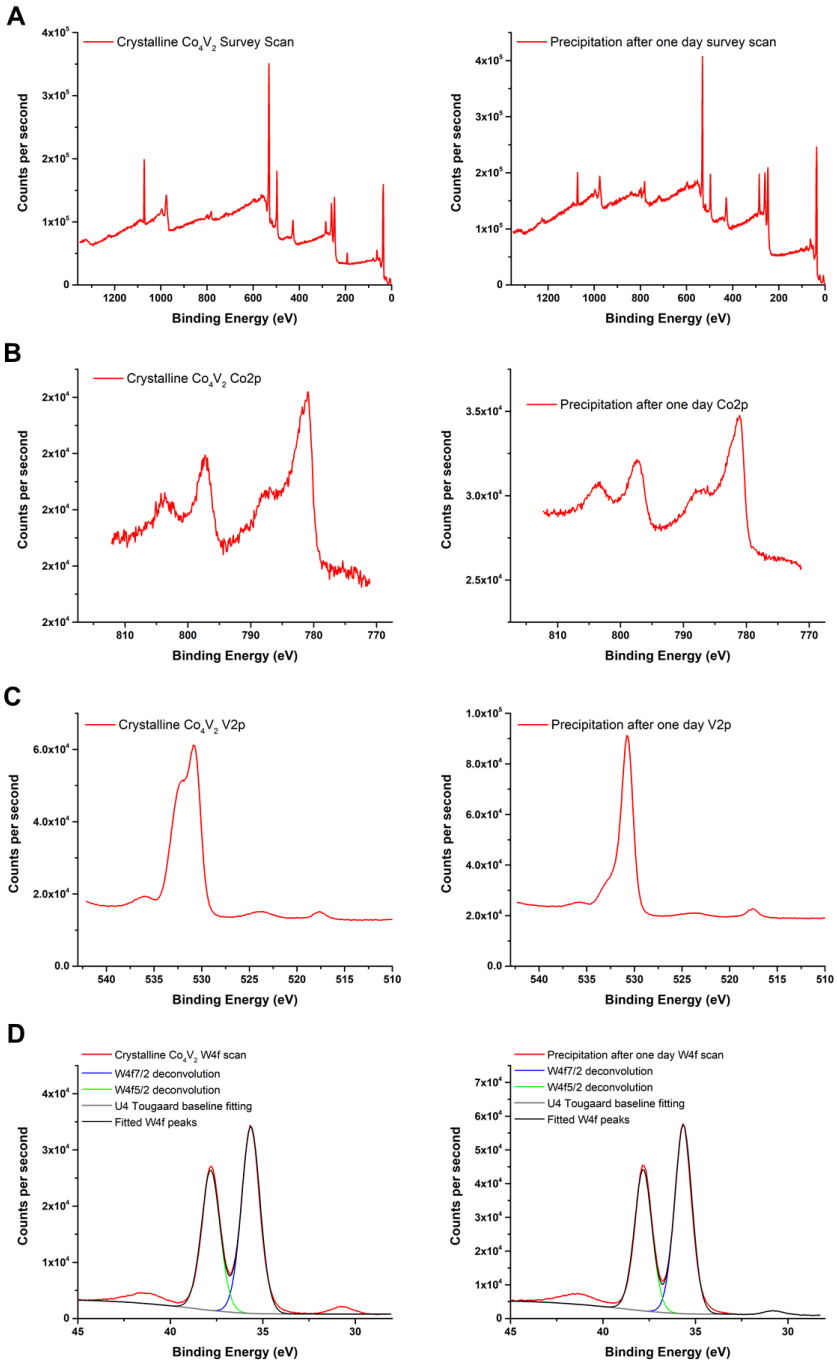

Figure 4.13. XPS analysis of **Co_4V_2** before and after dissolution in pH 8.3 NaB buffer. All precipitates are collected via centrifugation after either one day or one week of aging in pH 8.3 NaB buffer. (**A**) XPS survey scan from 0 eV to 1360 eV in binding energy. All peaks are accounted for in the formulation of the POM; (**B**) High resolution XPS measurement of the cobalt 2p region before and after precipitation. (**C**) High resolution XPS measurement of the vanadium 4f region before and after precipitation.; (**D**) High resolution XPS measurement of the tungsten 4f region before and after precipitation. Good fit is obtained for singular W(VI) species present.

b) Precipitation of **Co_4V_2** to form a solid.

To assess whether the missing signal is simply due to a decrease in solubility at elevated pH, the ^{51}V NMR trials in NaB at pH 8.3 and 9.0 were repeated, first passing the solution through a 0.2 µm syringe filter to remove undissolved materials before the NMR assessments (Figure 4.14).

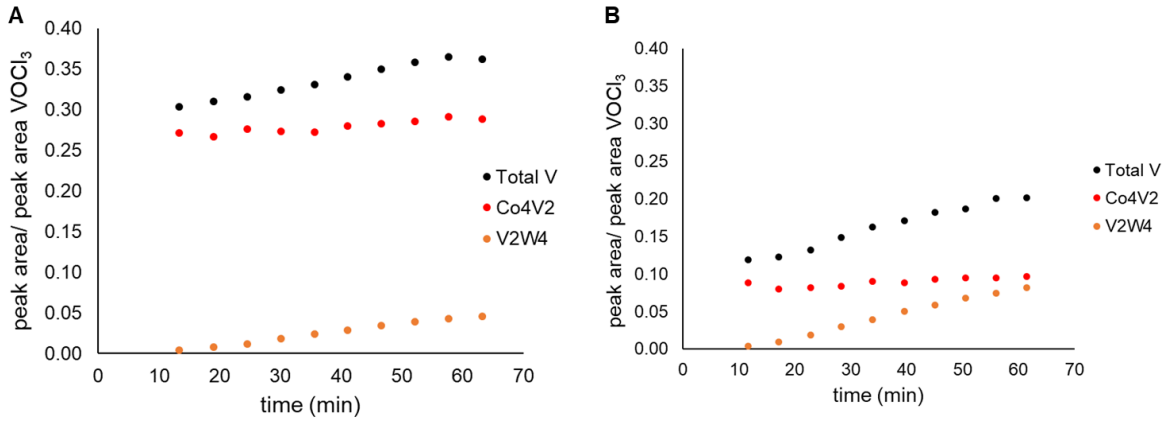

Figure 4.14. ^{51}V NMR study of kinetics of **Co_4V_2** after filtration. Relative ^{51}V NMR peak ratios of 5mM **Co_4V_2** taken in 80mM NaB buffer at (**A**) pH 8.3 and (**B**) pH 9.0 after filtration through a 0.2 µm syringe filter. Timer was started upon addition of the solution to the solid POM, and the solution was stirred for 5 min to ensure complete dissolution before filtration through the syringe filter, addition of the solution to the NMR tube and acquisition. A coaxial insert containing $VOCl_3$ and C_6D_6 was used for chemical shift referencing, locking, and for peak area comparison.

These studies reveal the same behavior as observed in the unfiltered cases (an increase in the signal for **Co_4V_2** over time), indicating that a solubility difference at elevated pH is not responsible for the missing signal. However, precipitation is observed at longer timescales and at further elevated pH and ionic strength. This suggests that a portion of the unobserved vanadium signal may result from solid formed during the reaction. Decreasing the ionic strength to 40 mM results in an increased **Co_4V_2** signal (Figure 4.15) and increasing the ionic strength to 160 mM results in the observed formation of solid material.

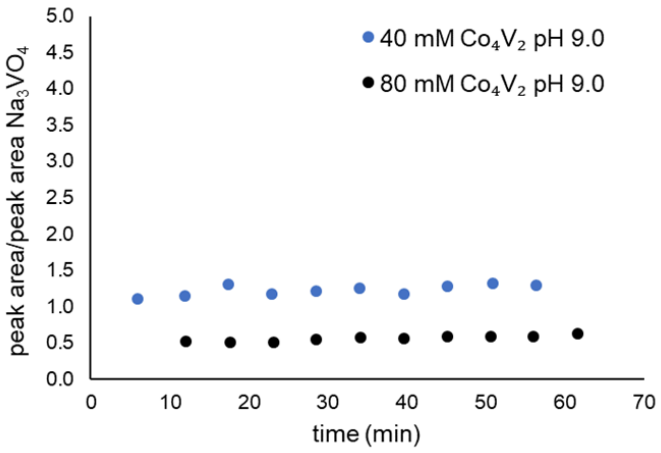

Figure 4.15. Effect of ionic strength on the **Co_4V_2** ^{51}V NMR signal. Conditions were 5mM **Co_4V_2** in 80mM NaB buffer pH 9.0. Timer was started upon addition of the solution to the solid POM. Solution was stirred for 5 min to ensure complete dissolution before addition of the solution to the NMR tube and acquisition. A coaxial insert containing 10mM Na_3VO_4 in D_2O was used for locking and for peak area comparison. Peaks are referenced to neat $VOCl_3$ at 0 ppm.

Attempts to study particle formation using light scattering techniques revealed that the solid particles were polydisperse and changed over time, and therefore were not suitable for DLS analysis. FT-IR spectra of the isolated solid did not reveal characteristic POM peaks, suggesting that the solid is a complex mixture of amorphous metal oxides, including vanadium oxides. Thus, some of the missing signal in the ^{51}V NMR spectrum is likely a result of solid formation due to the decomposition of **Co_4V_2** into mixed metal oxides.

c) Decomposition of the POM resulting in formation of Co-containing species not observed by NMR

A third potential cause of the missing ^{51}V NMR signal is decomposition resulting in $Co(II)_{aq}$ release, followed by formation of Co-containing complexes that are substantially more broadened

to the point where they are not observed above the baseline of the spectrum. To test the hypothesis that $Co(II)_{aq}$ released during decomposition may be broadening and shifting the lines, 50 mM $Co(NO_3)_2$ was added to a solution containing **Co_4V_2**. This increased the linewidth and shifted the peak by 5 ppm, but the signal remains the same before and after addition of cobalt, showing that interaction between $Co(II)_{aq}$ with the POM is not the cause of the missing ^{51}V NMR signal (Figure 4.16).

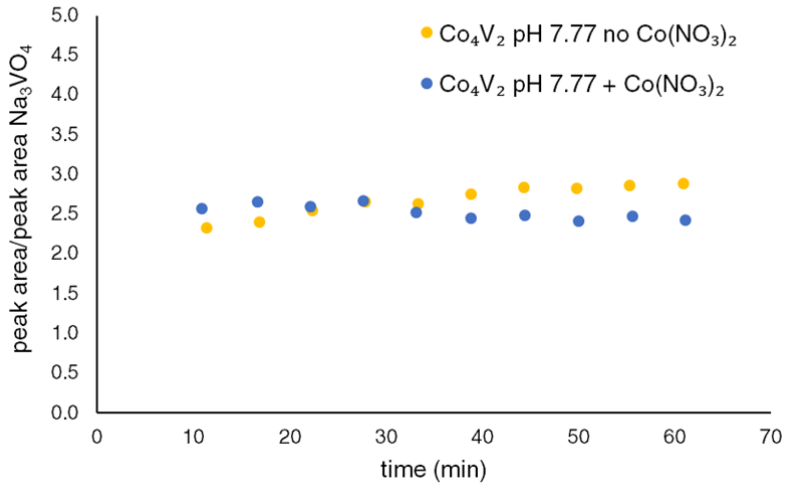

Figure 4.16. Effect of Co^{2+}_{aq} on **Co_4V_2** ^{51}V NMR signal. A 50 mM solution of $Co(NO_3)_2$ was added to a 5mM solution of **Co_4V_2** in 80mM pH 9.0 NaB buffer. Addition of $Co(NO_3)_2$ resulted in a decrease in pH, so a separate solution in 80mM pH 9.0 NaB buffer was pH-adjusted with HNO_3 to achieve the same pH (7.77). Timer was started upon addition of the solution to the solid POM. Solution was stirred for 5 min to ensure complete dissolution before addition of the solution to the NMR tube and acquisition. A coaxial insert containing 10mM Na_3VO_4 in D_2O was used for locking and for peak area comparison. Peaks are referenced to neat $VOCl_3$ at 0 ppm.

Several experiments have examined the solution stability of **Co_4V_2** under water oxidation conditions by determining the concentration of $Co(II)_{aq}$.[33-34] Line-broadening in the ^{31}P NMR spectrum of phosphate has been used as a probe for the concentration of $Co(II)_{aq}$ in solutions containing **Co_4V_2**.[34] First, the stability of **Co_4V_2** in sodium phosphate buffer was examined to

ensure that NaP itself would not alter the speciation and stability of **Co₄V₂**, as it has been demonstrated that Co-containing POMs are unstable towards certain buffer anions at basic pH values.[27] This phenomenon is particularly notable in phosphate buffer, where strong complexation of Co by phosphate buffer anions results in a shift in the speciation of Co(II) complexes and leads to decomposition of the isostructural **Co₄P₂** analogue.[25, 27, 58] Overall, the **Co₄V₂** signal over time observed in NaP is similar to that of NaB at the same pH, suggesting that NaP has a relatively small impact on the amount of **Co₄V₂** present (Figure 4.17).

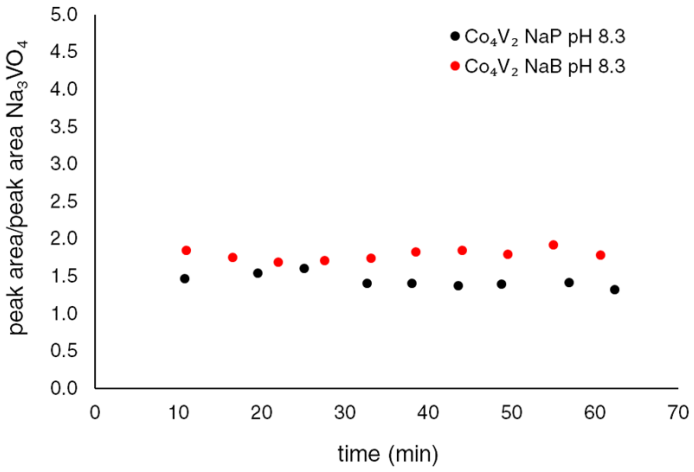

Figure 4.17. ^{51}V NMR study of effect of phosphate. Conditions were 5mM **Co₄V₂** in 80mM NaB buffer or 80mM NaP buffer at pH 8.3. Timer was started upon addition of the solution to the solid POM. Solution was stirred for 5 min to ensure complete dissolution before addition of the solution to the NMR tube and acquisition. A coaxial insert containing 10mM Na_3VO_4 in D_2O was used for locking and for peak area comparison. Peaks are referenced to neat $VOCl_3$ at 0ppm.

Using ^{31}P NMR line-broadening to measure the concentration of $Co(II)_{aq}$ revealed an increase in the amount of $Co(II)_{aq}$ in solution over time, reaching a maximum of 17.5 µM around 30 minutes in NaP at pH 8.3 (Figure 4.18). The maximum amount of $Co(II)_{aq}$ which can be released from a 5

μM solution of **Co₄V₂** is 20 μM, meaning that under these conditions, nearly 90% of the cobalt in the system is present as $Co(II)_{aq}$ after only 30 minutes.

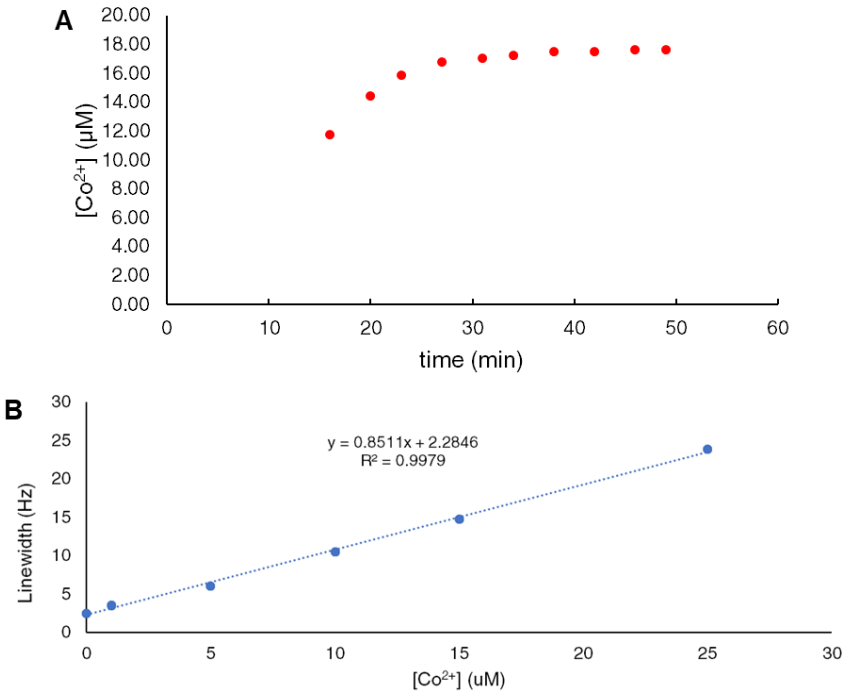

Figure 4.18. ^{31}P line-broadening analysis to determine Co^{2+}_{aq} concentration. (**A**) ^{31}P line-broadening measured over time using a 5 μM solution of **Co₄V₂**. Time was started upon addition of solvent to **Co₄V₂**. (**B**) Calibration curve correlating cobalt concentration and line-broadening of NaP in solution. All solutions contained 100 mM NaP pH 8.3 with 25% D_2O.Peaks are referenced to 85% H_3PO_4 in H_2O, and line-broadening analysis was done using MestreNova NMR software.

These results differ from the conclusions reached through ^{51}V NMR analysis, which show that a moderate amount of **Co₄V₂** still exists in solution at pH 8.3. The primary difference between these two studies is the concentration of **Co₄V₂**, as the ^{51}V experiments are done at several orders of magnitude higher concentration than the ^{31}P line-broadening analyses. To study the effect of concentration, we performed a similar study by dissolving 5 mM **Co₄V₂** in the buffer of choice, followed by extraction of the POM into toluene at varying time points, 1000-fold dilution, and

measurement of the $Co(II)_{aq}$ concentration of the aqueous layer using the ^{31}P line-broadening method. Extraction of **Co_4V_2** was achieved by exchanging the Na^+ counterion for THPA, as has been demonstrated previously in studies of POM stability.[27] The ability of POMs to exchange multiple counterions allows them to be selectively extracted into the organic layer, while all of the $Co(II)_{aq}$ remains in the aqueous layer. Analysis of the samples aged for one hour at pH 8.0, 8.3, and 9.0 detected 1.9, 3.3, and 7.9 μM of $Co(II)_{aq}$, significantly less than is observed at experiments run at low [**Co_4V_2**] (Figure 4.19).

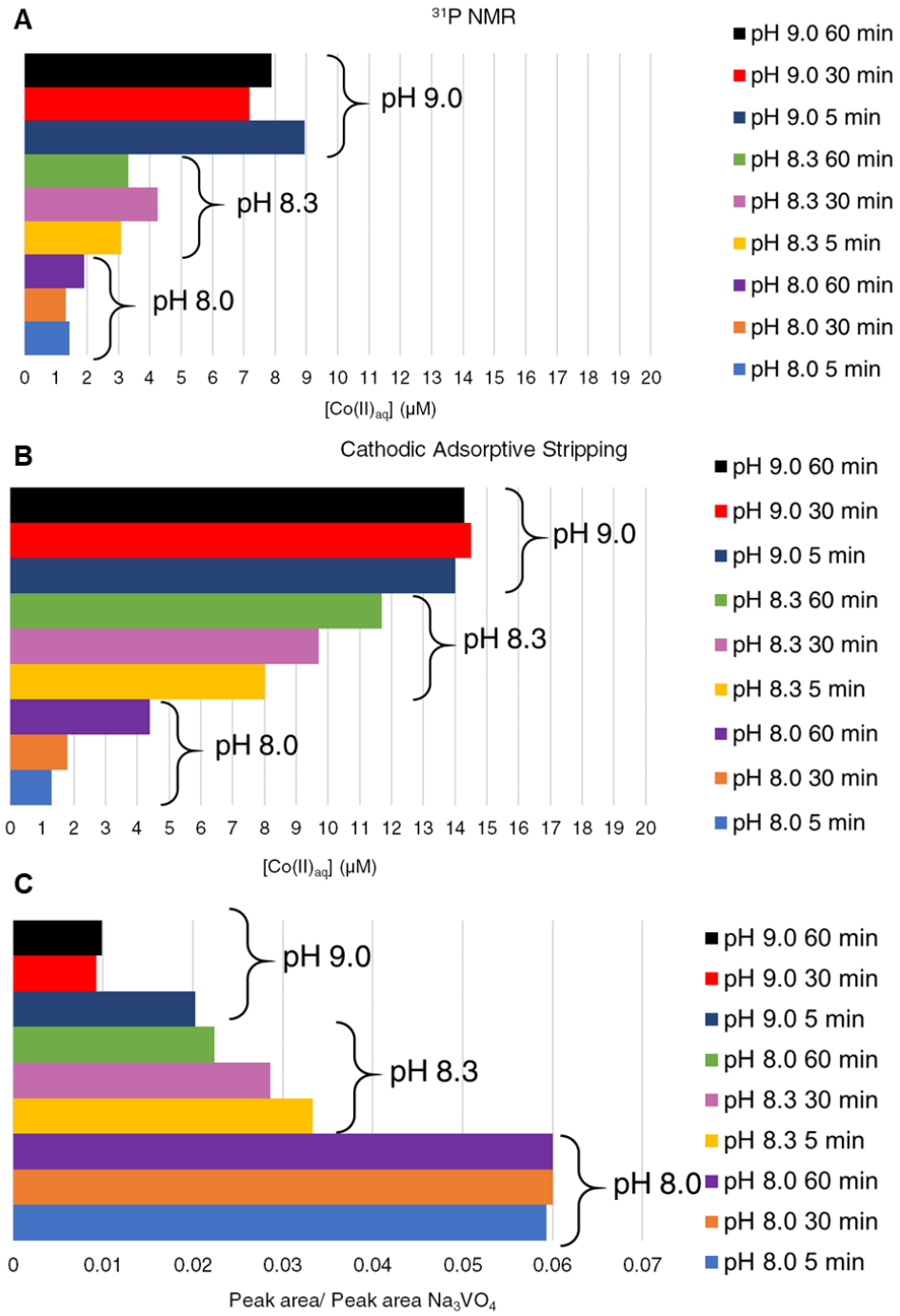

Figure 4.19. THPA extraction studies. For these studies, each point represents a separate sample, as each one was used as a separate extraction. (**A**) $Co(II)_{aq}$ concentration in the aqueous layer after extraction from solutions at varying pH, measured using the ^{31}P line-broadening method. After extraction, solutions were diluted 1000X before analysis. (**B**) $Co(II)_{aq}$ concentration in the aqueous layer after extraction from solutions at varying pH, measured using the dmg cathodic adsorptive stripping voltammetry method. (**C**) **THPA-Co_4V_2** relative concentrations measured in the toluene layer using ^{51}V NMR. All peaks are referenced to 10mM Na_3VO_4 in D_2O in a coaxial insert. In all cases, buffers were made using 80mM NaB at the indicated pH.

This demonstrates that there is a strong concentration dependence of the POM speciation in solution. Chelating reagents such as dimethylglyoxime (dmg) or 2,2'-bipyridine (bpy), have been used in conjunction with cathodic adsorptive stripping voltammetry in several WOC studies to quantify or sequester $Co(II)_{aq}$ in solution.[22, 27, 34] As an additional method to quantify $Co(II)_{aq}$, cathodic adsorptive stripping voltammetry experiments were performed using the same extracted samples as for the ^{31}P NMR study. The amount of detected cobalt was higher than the ^{31}P NMR line-broadening analyses, with 4.4, 11.7, and 14.3 μM $Co(II)_{aq}$ detected 60 minutes after dissolution. The discrepancy between these values suggests that there may be cobalt-containing species that are formed which are not extracted into the toluene layer, from which cobalt can be removed by dmg during the adsorptive stripping experiment. The ^{31}P NMR experiment is capable of measuring only $Co(II)_{aq}$ in solution, whereas the strong affinity of dmg for cobalt makes it more likely to remove cobalt from compounds prior to the adsorptive stripping experiment. Analysis of the ^{51}V NMR spectra of the toluene layer reveals a single peak located at 357 ppm which corresponds to $\mathbf{Co_4V_2}$, with no other vanadium signal observed. The ^{51}V NMR spectra of the extracted POM in the toluene layer reveals that the greatest amount of intact $\mathbf{Co_4V_2}$ observed the toluene layer occurs at pH 8.0, with much less POM present when extracting from a pH 9.0 solution (Figure 4.19), in accordance with the ^{31}P NMR and adsorptive cathodic stripping voltammetry experiments. The ^{51}V NMR spectra of the aqueous layer do not reveal any vanadium signals, confirming that any vanadium-containing compounds left in the aqueous layer are in a form that is not observed by ^{51}V NMR (Figure 4.20).

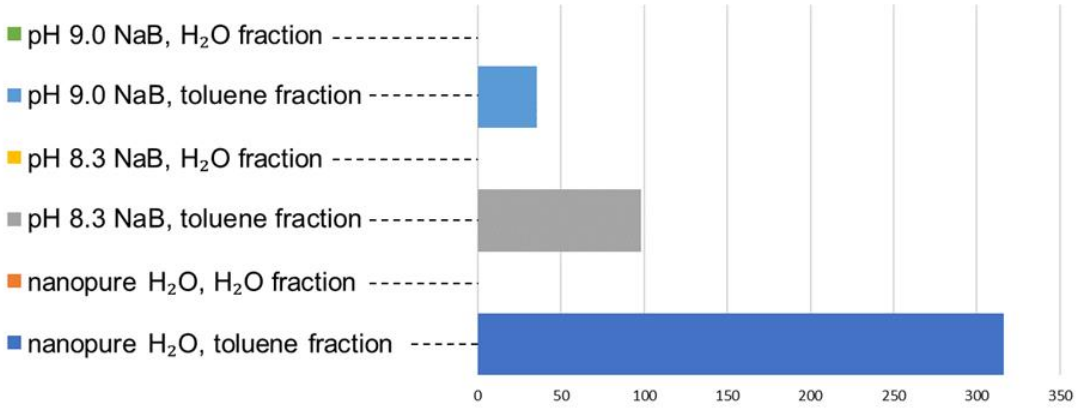

Figure 4.20. THPA extraction of **Co_4V_2**. ^{51}V NMR spectrum taken of 5 mM **Co_4V_2** 5 minutes after dissolution in water, followed by extraction with THPA-NO_3 in toluene for 5 minutes. A coaxial insert containing 10mM Na_3VO_4 in D_2O was used for locking and for peak area comparison. No signal is observed for the aqueous layer in any of the conditions. Buffers were made using 80mM NaB at the indicated pH.

At elevated pH, the primary observed side product **V_2W_4** is also unstable and undergoes speciation, resulting in the formation of various polyvanadates.[47, 59] This change is consistent with a decrease in the intensity of the color of the solution as the yellow octahedral POM vanadates became colorless tetrahedral vanadates (Figure 4.21).

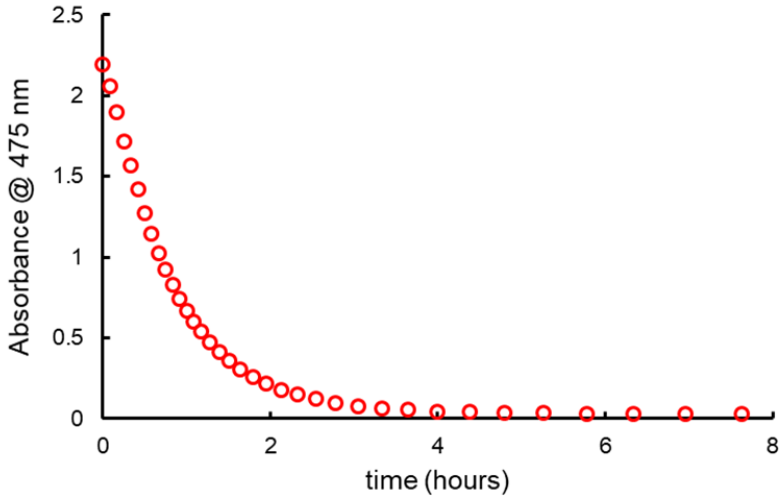

Figure 4.21. UV-Vis kinetics of **V_2W_4** decomposition. Absorbance measurements were taken at 475 nm after **V_2W_4** was dissolved in 80 mM NaB pH 8.3.

Adding one equivalent of $Co(II)_{aq}$ to this system results in solid formation, likely the result of a reaction between the vanadates in solution and cobalt to form various cobalt vanadates. This is confirmed by ^{51}V NMR, where it is observed that cobalt addition does not substantially affect the **V_2W_4** peak (slightly shifted and broadened), but immediately results in the disappearance of the polyvanadate peaks that are present after aging (Figure 4.22). This same process likely occurs in the **Co_4V_2** system, with POM undergoing speciation and equilibration to form **V_2W_4**, which goes on to form cobalt vanadate species.

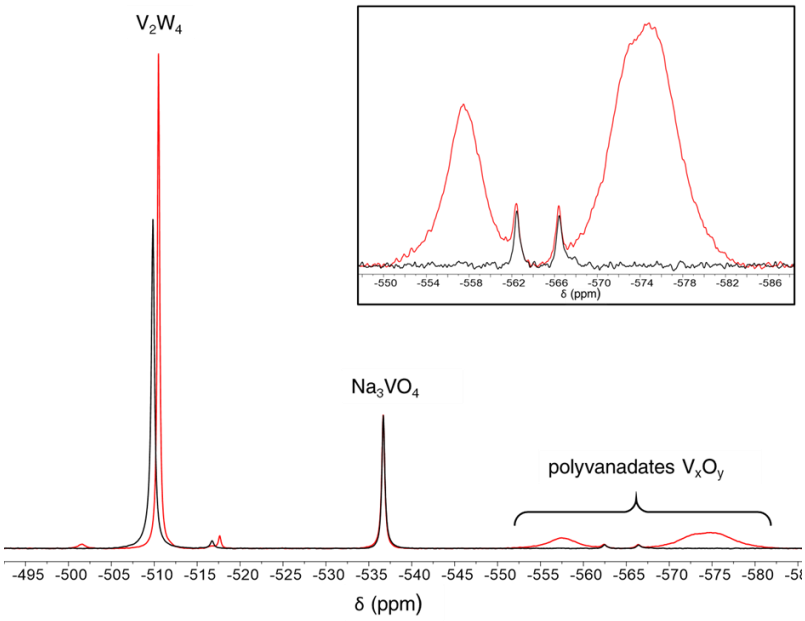

Figure 4.22. ^{51}V NMR spectra of **V_2W_4** before and after addition of $Co(NO_3)_2$. **V_2W_4** (5 mM) was incubated for 12 hours resulting in the formation of polyvanadate peaks. Addition of $Co(NO_3)_2$ immediately results in the disappearance of these peaks. A coaxial insert containing 10mM Na_3VO_4 in D_2O was used for locking and for peak area comparison. Inset: enlarged view of polyvanadate peaks before and after $Co(NO_3)_2$ addition. Spectra shown are before (red trace) and after (black trace) addition of $Co(NO_3)_2$

Taken together, these studies show that as the solution pH is increased, more **Co_4V_2** is converted to other vanadium-containing compounds. This process depends on pH, concentration, and ionic

strength. This work has established the use of ^{51}V NMR as an effective means to assess **Co$_4$V$_2$** stability in both solution and in the solid state. However, the very low POM concentrations used in water oxidation catalysis, as well as the presence of poorly soluble components in the reaction mixture during water oxidation catalysis (such as commonly-used chemical oxidant $[Ru(bpy)_3]^{3+}$) preclude the use of ^{51}V NMR to follow speciation under the exact conditions used for water oxidation experiments.

4.3.4 Kinetic Studies

The ^{51}V NMR studies described above show that the amount of **Co$_4$V$_2$** present in solution primarily depends on the pH. An issue of significant importance, therefore, is determining whether observed WOC activity is due to **Co$_4$V$_2$** or to a decomposition product such as $Co(II)_{aq}$. The catalytic efficiency for water oxidation can be observed by following the consumption of $[Ru(bpy)_3]^{3+}$ by the catalyst.[17] Kinetics of catalytic $[Ru(bpy)_3]^{3+}$ reduction were compared between $Co(II)_{aq}$ and **Co$_4$V$_2$** by tracking early-time curves using stopped-flow UV/vis techniques (Figure 4.23). For **Co$_4$V$_2$**, the maximum rates are achieved at the beginning of the reaction with no observed induction period. For $Co(II)_{aq}$, however, the reaction begins only after a very distinct induction period, which is typically 0.04 - 0.1 s long, likely due to aggregation resulting in the formation of polynuclear Co complexes that are active WOCs. This difference in induction period suggests that the water oxidation activity cannot be attributed exclusively to $Co(II)_{aq}$.

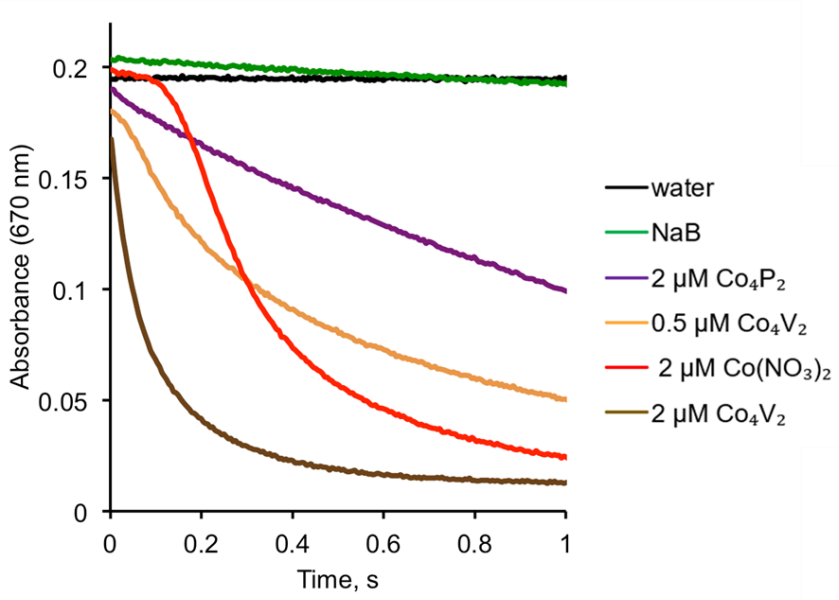

Figure 4.23. Kinetics of $[Ru(bpy)_3]^{3+}$ reduction (measured at 670 nm) catalyzed by solutions of: 2 μM $Co(NO_3)_2$, 2 μM **Co_4P_2**, 0.5 or 2 μM **Co_4V_2** at pH 9.0. All stock solutions of the catalyst were freshly prepared in 160 mM of NaB at pH 8.5 and then the solution was mixed by adding 0.5 mM $[Ru(bpy)_3]^{3+}$ in nitric acid solution to bring the final pH to 9.0.

In order to explore a possible involvement of decomposition products on the observed catalytic activity, the effect of **V_2W_4** on the kinetics of $[Ru(bpy)_3]^{3+}$ reduction catalyzed by $Co(NO_3)_2$ was examined. The induction period characteristic for $Co(NO_3)_2$ decreases as the aging time of the $Co(NO_3)_2$/**V_2W_4** mixture increases (Figure 4.24). After 30 minutes, additional aging time had no effect on the kinetic curves. The ^{51}V NMR studies shown in Figure 4.22 show that combining $Co(NO_3)_2$ and **V_2W_4** leads to the formation of cobalt vanadates, several of which are known to be active towards water oxidation,[60-61] and are likely contributing to the observed catalytic activity.

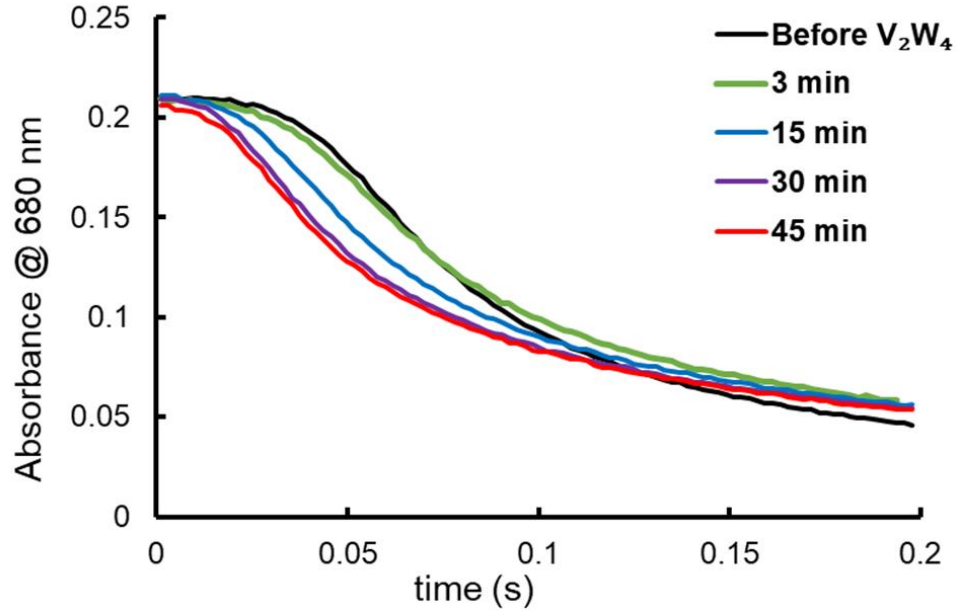

Figure 4.24. Kinetics of $[Ru(bpy)_3]^{3+}$ reduction (measured at 670 nm) catalyzed by solutions of 5 μM $Co(NO_3)_2$ and 25 μM **V_2W_4** in 80 mM NaB at pH 8.3. All stock solutions of the catalyst were freshly prepared in 160 mM of NaB at pH 8.5 and then the solution was mixed by adding 0.5 mM $[Ru(bpy)_3]^{3+}$ in nitric acid solution to bring the final pH to 8.3. Black curve – before adding **V_2W_4**, green after 3 min, blue after 15 min, purple and red after 30 and 45 min, respectively.

Similarly, allowing **Co_4V_2** to age in NaB buffer at pH 9.0 led to an increase in the rate of catalytic $[Ru(bpy)_3]^{3+}$ reduction, consistent with the formation of additional highly active catalysts over time (Figure 4.25). However, as the aging time is increased an induction period appears, demonstrating that the active catalyst is changing during the reaction to a faster catalyst that has an induction period. Even at longer aging times, the induction period observed in solutions of **Co_4V_2** are shorter than those for $Co(II)_{aq}$. Under water oxidation conditions, some amount of **Co_4V_2** may remain active, but the presence of other compounds including cobalt vanadates and $Co(II)_{aq}$ makes identification of the primary species responsible for water oxidation extremely challenging.

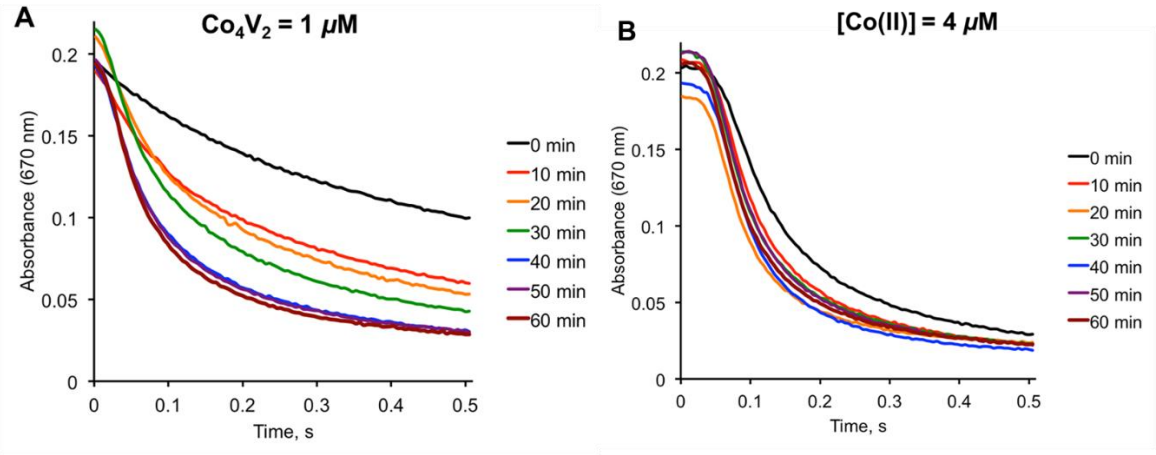

Figure 4.25. Stopped-flow UV-Vis studies of catalytic $[Ru(bpy)_3]^{3+}$ reduction in the presence of **Co_4V_2** solutions aged for varying amounts of time. (**A**) Kinetic curves taken at different aging times of **Co_4V_2**. (**B**) Kinetic curves taken at different aging times of $Co(NO_3)_2$. All solutions were freshly prepared immediately before analysis.

4.4 Conclusions

This work describes an improved synthesis for **Co_4V_2**, identifies its unusual ^{51}V NMR signal in solid and solution state, and assesses its purity and stability in solution through a variety of techniques. In aqueous solution, **Co_4V_2** slowly decomposes to **V_2W_4** and **VW_5**, but this decomposition takes place over an extended timescale, whereas the hydrophobic analogue **TBA-Co_4V_2** does not undergo solvolytic decomposition and is indefinitely stable in acetonitrile. At elevated pH levels, the situation becomes more complex, where ^{51}V NMR data suggest that speciation results in the rapid formation of compounds that cannot be observed in the NMR spectrum. These are likely cobalt vanadates and other metal oxides, as well as **V_2W_4**. After this initial equilibration, the remaining **Co_4V_2** remains stable over a one-hour time period, much longer than the timescale of typical water oxidation experiments. At low concentration, however, it is likely that small amounts of the POM remain intact after equilibration, making the identification of the various active catalysts in the system a challenging task.

Rigorous investigation of POM WOC systems, like other multi-component photocatalytic or photoelectrosynthetic systems, can be difficult because the measurements themselves can result in changes to the composition of the catalyst. In the case of **Co_4V_2**, these experimental limitations may impede or even prevent elucidation of the complete picture of the complex speciation behavior in solution. However, studies aimed at a deeper understanding of the many facets affecting stability and reactivity of this system, as well as related systems, are invaluable for scientific progress to develop catalysts that are not only more active and selective, but more stable. This work thus provides additional insights and methods for use during further investigations on related systems.

4.5 References

1. Chow, J.; Kopp, R. J.; Portney, P. R., *Science* **2003,** 302 (5650), 1528-1531.

2. Lewis, N. S.; Nocera, D. G., *Proceedings of the National Academy of Sciences* **2006,** 103 (43), 15729-15735.

3. Gray, H. B., *Nature Chemistry* **2009,** 1, 7.

4. Rüttinger, W.; Dismukes, G. C., *Chemical Reviews* **1997,** 97 (1), 1-24.

5. Yagi, M.; Kaneko, M., *Chemical Reviews* **2001,** 101 (1), 21-36.

6. Tachibana, Y.; Vayssieres, L.; Durrant, J. R., *Nature Photonics* **2012,** 6, 511.

7. Faunce, T.; Styring, S.; Wasielewski, M. R.; Brudvig, G. W.; Rutherford, A. W.; Messinger, J.; Lee, A. F.; Hill, C. L.; deGroot, H.; Fontecave, M.; MacFarlane, D. R.; Hankamer, B.; Nocera, D. G.; Tiede, D. M.; Dau, H.; Hillier, W.; Wang, L.; Amal, R., *Energy & Environmental Science* **2013,** 6 (4), 1074-1076.

8. Lv, H.; Geletii, Y. V.; Zhao, C.; Vickers, J. W.; Zhu, G.; Luo, Z.; Song, J.; Lian, T.; Musaev, D. G.; Hill, C. L., *Chemical Society Reviews* **2012,** 41 (22), 7572-7589.

9. Blakemore, J. D.; Crabtree, R. H.; Brudvig, G. W., *Chemical Reviews* **2015,** 115 (23), 12974-13005.

10. Hunter, B. M.; Gray, H. B.; Muller, A. M., *Chemical reviews* **2016,** 116 (22), 14120-14136.

11. McCrory, C. C. L.; Jung, S.; Peters, J. C.; Jaramillo, T. F., *Journal of the American Chemical Society* **2013,** 135 (45), 16977-16987.

12. Gerken, J. B.; Shaner, S. E.; Massé, R. C.; Porubsky, N. J.; Stahl, S. S., *Energy & Environmental Science* **2014,** 7 (7), 2376-2382.

13. Kanan, M. W.; Nocera, D. G., *Science* **2008,** 321 (5892), 1072-1075.

14. Lutterman, D. A.; Surendranath, Y.; Nocera, D. G., *Journal of the American Chemical Society* **2009,** 131 (11), 3838-3839.

15. McAlpin, J. G.; Surendranath, Y.; Dincă, M.; Stich, T. A.; Stoian, S. A.; Casey, W. H.; Nocera, D. G.; Britt, R. D., *Journal of the American Chemical Society* **2010,** 132 (20), 6882-6883.

16. Risch, M.; Klingan, K.; Ringleb, F.; Chernev, P.; Zaharieva, I.; Fischer, A.; Dau, H., *ChemSusChem* **2012,** 5 (3), 542-549.

17. Yin, Q.; Tan, J. M.; Besson, C.; Geletii, Y. V.; Musaev, D. G.; Kuznetsov, A. E.; Luo, Z.; Hardcastle, K. I.; Hill, C. L., *Science* **2010,** 328 (5976), 342-345.

18. Soriano-López, J.; Goberna-Ferrón, S.; Vigara, L.; Carbó, J. J.; Poblet, J. M.; Galán-Mascarós, J. R., *Inorganic Chemistry* **2013,** 52 (9), 4753-4755.

19. Lv, H.; Song, J.; Geletii, Y. V.; Vickers, J. W.; Sumliner, J. M.; Musaev, D. G.; Kögerler, P.; Zhuk, P. F.; Bacsa, J.; Zhu, G.; Hill, C. L., *Journal of the American Chemical Society* **2014,** 136 (26), 9268-9271.

20. Soriano-López, J.; Musaev, D. G.; Hill, C. L.; Galán-Mascarós, J. R.; Carbó, J. J.; Poblet, J. M., *Journal of Catalysis* **2017,** 350, 56-63.

21. Weinstock, I. A.; Barbuzzi, E. M. G.; Wemple, M. W.; Cowan, J. J.; Reiner, R. S.; Sonnen, D. M.; Heintz, R. A.; Bond, J. S.; Hill, C. L., *Nature* **2001,** 414 (6860), 191-195.

22. Stracke, J. J.; Finke, R. G., *J. Am. Chem. Soc.* **2011,** 133, 14872-14875.

23. Stracke, J. J.; Finke, R. G., *ACS Catal.* **2013,** 3 (6), 1209-1219.

24. Stracke, J. J.; Finke, R. G., *ACS Catal.* **2014,** 4, 79-89.

25. Goberna-Ferrón, S.; Soriano-López, J.; Galán-Mascarós, J. R.; Nyman, M., *Eur. J. Inorg. Chem.* **2015**, 2833-2840.

26. Schiwon, R.; Klingan, K.; Dau, H.; Limberg, C., *Chem. Commun.* **2014,** 50, 100-102.

27. Vickers, J. W.; Lv, H.; Sumliner, J. M.; Zhu, G.; Luo, Z.; Musaev, D. G.; Geletii, Y. V.; Hill, C. L., *J. Am. Chem. Soc.* **2013,** 135 (38), 14110-14118.

28. Li, J.; Güttinger, R.; Moré, R.; Song, F.; Wan, W.; Patzke, G. R., *Chemical Society Reviews* **2017,** 46 (20), 6124-6147.

29. Stracke, J. J.; Finke, R. G., *Journal of the American Chemical Society* **2011,** 133 (38), 14872-14875.

30. Stracke, J. J.; Finke, R. G., *ACS Catalysis* **2013,** 3 (6), 1209-1219.

31. Natali, M.; Berardi, S.; Sartorel, A.; Bonchio, M.; Campagna, S.; Scandola, F., *Chemical Communications* **2012,** 48 (70), 8808-8810.

32. Vickers, J. W.; Lv, H.; Sumliner, J. M.; Zhu, G.; Luo, Z.; Musaev, D. G.; Geletii, Y. V.; Hill, C. L., *Journal of the American Chemical Society* **2013,** 135 (38), 14110-14118.

33. Folkman, S. J.; Kirner, J. T.; Finke, R. G., *Inorg. Chem.* **2016,** 55 (11), 5343-5355.

34. Folkman, S. J.; Finke, R. G., *ACS Catalysis* **2017,** 7 (1), 7-16.

35. Sullivan, K. P.; Wieliczko, M.; Kim, M.; Yin, Q.; Collins-Wildman, D. L.; Mehta, A. K.; Bacsa, J.; Lu, X.; Geletii, Y. V.; Hill, C. L., *ACS Catalysis* **2018,** 8 (12), 11952-11959.

36. Flynn, C. M.; Pope, M. T., *Inorg. Chem.* **1971,** 10 (11), 2524-2529.

37. Li, B.; Yan, Y.; Li, F.; Xu, L.; Bi, L.; Wu, L., *Inorg. Chim. Acta* **2009,** (362), 2796-2801.

38. Wieliczko, M.; Geletii, Y. V.; Bacsa, J.; Musaev, D. G.; Hill, C. L., *Journal of Cluster Science* **2017,** 28 (2), 839-852.

39. Balula, Maria S.; Gamelas, José A.; Carapuça, Helena M.; Cavaleiro, Ana M. V.; Schlindwein, W., *Eur. J. Inorg. Chem.* **2004,** 2004 (3), 619-628.

40. Katsoulis, D. E.; Pope, M. T., *J. Am. Chem. Soc.* **1984,** 106 (9), 2737-2738.

41. Krolicka, A.; Bobrowski, A.; Kalcher, K.; Mocak, J.; Svancara, I.; Vytras, K., *Electroanalysis* **2003,** 15 (23-24), 1859-1863.

42. Sheldrick, G. M., *Acta Crystallographica. Section C, Structural Chemistry* **2015,** 71 (Pt 1), 3-8.

43. Dolomanov, O. V.; Bourhis, L. J.; Gildea, R. J.; Howard, J. A. K.; Puschmann, H., *J. Appl. Crystallogr.* **2009,** 42, 339-341.

44. Folkman, S. J.; Kirner, J. T.; Finke, R. G., *Inorganic Chemistry* **2016,** 55 (11), 5343-5355.

45. Andersson, I.; Hastings, J. J.; Howarth, O. W.; Pettersson, L., *Journal of the Chemical Society, Dalton Transactions* **1996,** (13), 2705-2711.

46. Lv, H.; Song, J.; Geletii, Y. V.; Vickers, J. W.; Sumliner, J. M.; Musaev, D. G.; Kögerler, P.; Zhuk, P. F.; Bacsa, J.; Zhu, G.; Hill, C. L., *J. Am. Chem. Soc.* **2014,** 136 (26), 9268-9271.

47. Rehder, D.; Polenova, T.; Bühl, M. In *Annual Reports on NMR Spectroscopy*, Webb, G. A., Ed. Academic Press: 2007; Vol. 62, pp 49-114.

48. Rehder, D., *Coordination Chemistry Reviews* **2008,** 252 (21–22), 2209-2223.

49. Bertini, I.; Luchinat, C.; Parigi, G., *Progress in Nuclear Magnetic Resonance Spectroscopy* **2002,** 40 (3), 249-273.

50. Varzatskii, O. A.; Penkova, L. V.; Kats, S. V.; Dolganov, A. V.; Vologzhanina, A. V.; Pavlov, A. A.; Novikov, V. V.; Bogomyakov, A. S.; Nemykin, V. N.; Voloshin, Y. Z., *Inorganic Chemistry* **2014,** 53 (6), 3062-3071.

51. Jorris, T. L.; Kozik, M.; Casan-Pastor, N.; Domaille, P. J.; Finke, R. G.; Miller, W. K.; Baker, L. C. W., *Journal of the American Chemical Society* **1987,** 109 (24), 7402-7408.

52. Huang, W.; Todaro, L.; Yap, G. P. A.; Beer, R.; Francesconi, L. C.; Polenova, T., *Journal of the American Chemical Society* **2004,** 126 (37), 11564-11573.

53. Ooms, K. J.; Bolte, S. E.; Smee, J. J.; Baruah, B.; Crans, D. C.; Polenova, T., *Inorganic Chemistry* **2007,** 46 (22), 9285-9293.

54. Bühl, M.; Parrinello, M., *Chemistry – A European Journal* **2001,** 7 (20), 4487-4494.

55. Müller, A.; Rehder, D.; Haupt, E. T. K.; Merca, A.; Bögge, H.; Schmidtmann, M.; Heinze-Brückner, G., *Angew. Chem. Int. Ed.* **2004,** 43, 4466-4470.

56. Howarth, O. W.; Pettersson, L.; Andersson, I., *Journal of the Chemical Society, Dalton Transactions* **1991,** (7), 1799-1812.

57. Pettersson, L. In *Polyoxometalate Chemistry for Nano-Composite Design*, Yamase, T., Pope, M. T., Eds. Springer US: Boston, MA, 2002; pp 139-147.

58. Lieb, D.; Zahl, A.; Wilson, E. F.; Streb, C.; Nye, L. C.; Meyer, K.; Ivanović-Burmazović, I., *Inorg. Chem.* **2011,** 50 (18), 9053-9058.

59. Rehder, D.; Weidemann, C.; Duch, A.; Priebsch, W., *Inorganic Chemistry* **1988,** 27 (3), 584-587.

60. Xing, M.; Kong, L.-B.; Liu, M.-C.; Liu, L.-Y.; Kang, L.; Luo, Y.-C., *Journal of Materials Chemistry A* **2014,** 2 (43), 18435-18443.

61. Liardet, L.; Hu, X., *ACS Catalysis* **2018,** 8 (1), 644-650.